UNDERSTANDING THE NANOCONFINED FLUID VIA ABSOLUTE FREE ENERGY DETERMINATION

By

Li Wan

Dissertation
Submitted to the Faculty of the
Graduate School of Vanderbilt University
in partial fulfillment of the requirements
for the degree of

DOCTOR OF PHILOSOPHY
in

CHEMICAL ENGINEERING

May, 2015

Nashville, Tennessee

Approved:

Professor Peter T. Cummings

Professor Clare M. McCabe

Professor M. Douglas LeVan

Professor Terry P. Lybrand

To Lily and Emily.

ACKNOWLEDGMENTS

I first want to thank my advisor, Professor Peter T. Cummings, for his invaluable guidance and support during the course of my Ph.D. research. Over the years, Peter has given me a tremendous amount of help by fostering my research skills and furthering my understanding of science and engineering. I have benefited greatly from these improvements in both my technical skills and in how I think about my career development. His wealth of knowledge, enterprising spirit, and keen insight are great examples for me and my work.

I also want to acknowledge the members of my dissertation committee: Prof. Clare McCabe, Prof. M. Douglas LeVan, and Prof. Terry P. Lybrand, whose guidance throughout my research has proven to be extremely beneficial. Their suggestions and critiques have driven me to a higher level and, for that, I am very thankful.

Since the beginning of my research, I have received much help and support from the members of Prof. Cummings' research group, especially from Dr. Hugh Docherty and Prof. Christopher R. Iacovella. Hugh's guidance in the early stages was critical to bringing me to this theoretical field and Christopher's advice helped to keep me pointed in the right direction. Without their help, the completion of some of this work would have been impossible.

I am very grateful to other members in the same group, including Prof. Guang Feng, Dr. William French, Dr. Song Li, Dr. Lili Gai, Dr. Adam Skelton, and Shan Guo. They all helped to make my work and life much easier and enjoyable. I am very lucky I had the opportunity to work in such a wonderful and energetic research group. These are memories I will cherish my whole life.

My appreciation also goes to the staff of Vanderbilt University, including Julie Canada, who worked with our research group, Mary Gilleran and Rae Uson, who worked in our department, and the staff of ISSS. They are the best and are always ready to help when you need it. Their dedicated work made my life easier and more efficient.

I gratefully acknowledge the financial support provided for this work from the National Science Foundation, the computing resources provided by the National Energy Research Scientific Computing Center (Hopper and the now-retired Franklin), the National Institute for Computational Sciences (Keeneland), and Cadbury at Vanderbilt University. The open source software package LAMMPS and HOOMD were also used in this work and are greatly appreciated.

TABLE OF CONTENTS

LIST OF TABLES

LIST OF FIGURES

CHAPTER I

INTRODUCTION

In recent years, the development of microelectromechanical systems (MEMS) and nanoelectromechanical systems (NEMS), such as mechanical actuators, pumps, accelerometers, and micro- and nano-scale motors, has received intense attention and effort from scientists and engineers. With their much smaller size, fewer raw material requirements, and lower energy demand, MEMS and NEMS have the potential to bring ideas that exist only in science fiction, such as lab-on-a-chip and robotic blood vessel clog-cleaners, to reality. However, the manufacturing and application of these devices requires a series of technological breakthroughs as well as an increased understanding of the physical and chemical behavior of every component at such a minute scale, especially for NEMS. Since most of these devices will be working in a fluidic environment, a vitally important question emerges: whether or not the fluid trapped by micro- and nano-scale devices still behaves the same as its corresponding bulk. And, in particular, whether or not a fluid undergoes a phase transition in nano-scale dimensions, such as by forming an ordered solid, or solid-like, phase.

Research on this question has given rise to a vigorous debate that began in the early 1990s. Following the earliest observation of nanoconfinement-induced solidification by Israelachvili and coworkers using static surface force apparatus (SFA)[1] , experiments by Klein and coworkers[2–4], using the dynamical surface force balance (SFB), on octamethylcyclotetrasiloxane (OMCTS) nanoconfined between two atomically smooth mica surfaces, yielded observation of orders of magnitude increase in viscosity and the onset of a non-zero yield stress, suggested a first order phase transition as the solid-surface separation is reduced from seven to six molecular layers. However, SFA experiments by Granick and coworkers[5] instead suggest a second-order transition rather than first-order, since no yield stress was observed and the viscosity increase is significantly smaller[6,7]. This controversy has spanned over two decades, despite a large number of experimental studies that aimed to definitively answer this important question. This is in large part due to the intrinsic difficulties faced in conducting these experiments[8]. Specifically, the fact that the nanoconfined phase is buried between two solid mica walls makes it impossible to directly observe its structure. From an experimental point of view, the inability to directly observe what occurs in the nanoconfined region is the major obstacle preventing a definitive conclusion. Moreover, the discovery of platinum nanoparticles on the mica surfaces in some experiments[9,10] led to a re-examination of published results, which potentially compromised some previous experimental observations[11].

Conversely, simulation studies, which have intrinsic molecular resolution, have no such observational problems. However, concerns over the realism of molecular models used in simulations as well as the lack of a clear demonstration that the solid-like structure observed is an equilibrated structure, rather than a metastable or transitional structure, has hindered wide acceptance of the results of these studies. The question of model accuracy has recently been well addressed by the Cummings group via the use of atomistically detailed models and physically realistic simulations of non-polar organic molecules nanoconfined by mica sheets. These simulation studies have provided strong evidence to support the experimental studies that observe a first-order phase transition, but haven't yet answered the question of whether or not the observed structure is metastable in nature.

To determine if a structure is metastable, the key measurement required is the free energy (FE) of the system since this quantity is minimized at equilibrium. However, to date, simulation studies of phase transitions under nanoconfinement have not effectively measured this quantity, probably due to the difficulty of computing the FE, both in bulk and, particularly, under confinement. Thus, this dissertation research is concentrated on the development and applications of absolute FE calculation methodology, specifically for nanoconfined systems, in order to apply the absolute FE as a tool to assist in an increased understanding of nanoconfined fluid phase behavior.

Chapter II of this thesis reviews previous experimental and simulation studies with emphasis on the debate in the SFA/SFB community. Evidence by researchers using other techniques, such as atomic force microscopy (AFM) , neutron scattering, differential scanning calorimetry (DSC) and other methods, are also briefly introduced. Subsequently, simulation studies on nanoconfined non-polar fluids are also reviewed and discussed. Like experimental studies, simulation studies have not reached a complete consensus on the nature of the phase transition with divergent simulation results and opposite conclusions reported in the last two decades. Lastly, Chapter II also reviews the development of major FE calculation techniques in the last several decades and briefly illustrates the pros and cons of recently proposed FE determination methods.

Chapter III details the model and methodology, and their step-by-step derivation, used in this research. The basic algorithm shows consistency with literature and the modified algorithm, which is specifically for nanoconfined systems, has also been validated. To correct the systematic error in FE calculation for nanoconfined system, we also introduce a modified tail correction. Use of this new tail correction greatly minimizes the error in potential evaluation, especially in nanoconfined systems with strong wall-fluid interactions. In a departure from conventional FE calculations, this work takes advantage of the parallel efficiency of molecular dynamics (MD) to speedup FE calculation. The difference in results due to the use of MD instead of monte carlo (MC) is also quantified and discussed. The advent of general-purpose computing on graphics processing units (GPGPU) in the last decade has enabled intensive parallel computing power for scientific research for applications able to take advantage of their unique architecture. Given the parallel nature of MD, implementation of GPGPU increases the speed of these simulations and, as such, was used to accelerate the calculations presented in this work.

Chapter IV can be viewed as the foundational work with the emphasis on the reexamination of FE calculations for bulk crystals. As the first step in solid FE calculation, this work reveals the roles of basic accuracy-influencing factors in FE calculation, such as simulation box shape, finite system size, finite-cutoff radius effect and so on. Their effects have been quantitatively measured in a series of judiciously selected scenarios. Potential compensation strategies, such as asymptotic finite size correction (FSC) and using a larger cutoff radius, have been reviewed and examined as ways to minimize the systematic error in absolute FE calculations. Meanwhile, the relative thermodynamic stability of fundamental crystal types has also been compared by employing absolute FE calculations. Among the investigated crystal types, including face centered cubic (FCC) crystal, body centered cubic (BCC) crystal, hexagonal closed packed (HCP) crystal, FCC demonstrates the lowest free energy and hence the highest thermodynamic stability.

Primary applications of the absolute FE calculation for nanoconfined systems are included in Chapter V to directly address fundamental questions in understanding nanoconfined phenomena. The roles of wall-fluid interaction strength and the wall-wall separation have been quantified by evaluating absolute FE values. Agreement has been reached with previous studies that employ indirect methods, such as calculating relative FE[12,13] and deriving a Clapeyron equation for confined fluid systems[14]. The FE data obtained in this work supports the existence of a phase transition. Additionally, an answer to the basic question of whether the nanoconfined phase is structurally identical to its bulk state has also been provided. We determined that the bulk-like configuration becomes less stable with increasing confinement and temperature. This means that a configuration with defects is preferred. Furthermore, FE calculations in incommensurate systems, where the size of wall particles is different from the size of fluid particles, in addition to commensurate systems, are also investigated. To reveal the effect of wall-fluid size on the confined phase thermodynamic stability, FE measurements of systems with various fluid/wall size ratios have been performed and compared with experimental results.

The nanoconfined systems investigated in Chapter VI are much closer to scenarios seen in physical experiments. In most experimental scenarios, the nanoconfined phase is immersed in the bulk fluid. Therefore, to stay true to experiments, grand canonical molecular dynamics (GCMD) simulations were conducted and the absolute FE of the nanoconfined phase measured, to better understand the nature of nanoconfined fluid behavior. Given the intensive computing power provided by graphics processing unit (GPU) and the parallel nature of molecular dynamics simulation, the open source software package HOOMD (highly optimized object-oriented many-particle dynamics) was used to accelerate the simulation. With the advantage of having the absolute FE calculated, the thermodynamic stability comparison under different wall-wall separations then became straightforward. The nanoconfined phase exhibited a large absolute FE oscillation as the separation increased, rather than exhibiting a smooth monotonically increasing line. This provides hints that even if the existence of a phase transition is proven and a consensus on the nature of that transition is reached, the behavior of the nanoconfined phase when the wall-wall separation is below the critical value, might not be exactly the same as was originally assumed. In other words, the nanoconfined phase might not stay in a solid state as the separation is reduced below the transition point. With the assistance of absolute FE measurements on each individual layer, the role of boundary and central layers in determining nanoconfined phase thermodynamic stability was differentiated in this work. The finding that the nanoconfined fluid phase behavior is dominated by central layers, in conjunction with FE calculations specifically for central layers, provides clues as to why there exists differing conclusions among experimental researchers. However, these still leave the debate unresolved.

Chapter VII examines some of the crucial differences between the SFB experiment by Klein's group and the SFA experiment by Granick's group. Of particular interest is how these differences contribute to each group's dramatically different understanding of nanoconfined fluid behavior as well as what intrinsic properties are actually shared by these experimental studies. Large scale molecular dynamics simulations and real-time order parameter measurements suggest that the larger contact area used in Granick's experiment[15,16] requires more time for the system to equilibrate. Additionally, several factors indicate a dramatically slower dynamic such as the manner in which the two solid walls approach each other, the viscosity measurement, the much faster confining speed, and the slower shearing speed. These systems turn out to be more difficult to reach equilibrium which increases the probability of the existence of “jammed” atoms in the nanoconfined region. In these simulations, extra atoms are artificially inserted into the nanoconfined region to mimic the aforementioned scenarios. The absolute FE measurements on systems with artificially injected atoms reveals that the extra atoms destabilize the system and limit the ability to transition a fluid into an equilibrated solid. Subsequently, Chapter VIII further investigates systems with various nanoconfined-phase densities, and examines the roles of “jammed” atoms in nanoconfined fluid behavior.

Based on the FE calculations performed in previous chapters, and the most recent simulation studies on nanoconfined fluid, this dissertation research proposes a thought process that might reconcile the two-decades-long debate in this field and give a relatively clear view on the nature of nanoconfined fluid behavior.

The last chapter summarizes this dissertation research and provides suggestions for future research as well as possible applications based on the knowledge obtained in this work.

CHAPTER II

BACKGROUND

2.1 Understanding the Nanoconfined Fluid

2.1.1 MEMS/NEMS Development

In the last fifty years, the electronics industry has seen many great developments, not the least of which are advancements in device miniaturization. Early in 1962, Tufte, Chapman, and Long[17], working at Honeywell, successfully created the first electromechanical device at the micron scale: a silicon integrated piezo-actuator at a thickness of approximately 200 microns. Only three years later, Nathanson and Wickstrom[18], working at Westinghouse, reported the successful creation of an accelerometer at a much smaller size, only 6.3 microns in radius. Following these pioneering creations, the practical application of such small devices started at a rapid pace. The first commercialized micron-sized sensor appeared on the market in 1973. After that, the doorway to developing and utilizing micron scale or even smaller, nanoscale, electromechanical devices was opened. In a workshop in 1989, Professor Howe[19,20] from U.C. Berkeley first used the acronym for microelectromechanical systems (MEMS, shown in Figure 2.1) to name this new field. In the early days of the field these devices shared a plethora of similarities with microelectronics, but even then they were already a distinct arena. MEMS and its future substitute and supplementary, NEMS, have seen a rapid expansion of manufacturing capacity in the microscopic world within the last several decades. To date, in addition to intense research attention and efforts, MEMS/NEMS have already found wide applications in industry in such devices as inkjet print heads, high-resolution digital displays, pressure and inertial sensors and many others[20].

Recently discovered and synthesized carbon-based structures such as buckyballs[23–25], graphene[26], and carbon nanotubes[27,28] (shown in Figure 2.2), make excellent candidate

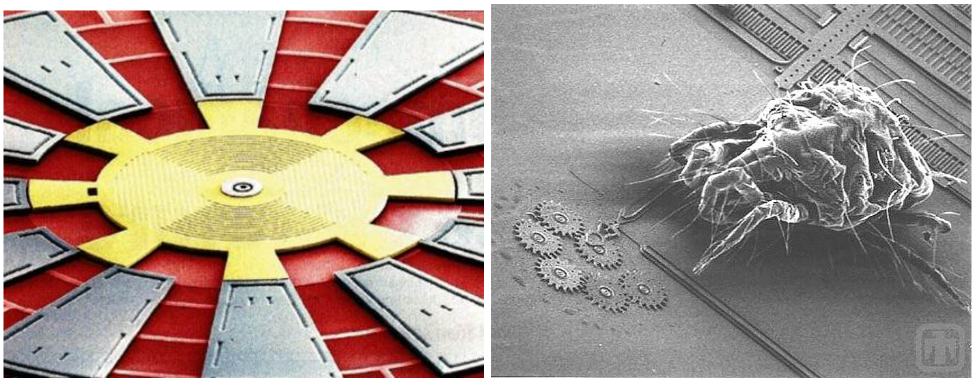

Figure 2.1. Semi-schematic diagram (left) of a MEMS electrostatic micromotor from the work of Roukes[21]. Scanning electron microscope (SEM) image (right) of a mite approaching a gear chain from Sandia National Lab.[22] The mite is approximately 1 millimeter long.

components for building nanoscale electromechanical devices due to their marvelous properties and well defined configuration. However, further development and application of MEMS/NEMS not only have to deal with traditional problems, such as the miniaturization of devices, component assembly in nanoscale, and their compatibility with the working environment, but they also have to meet new challenges brought on by shrinking their dimension by many orders of magnitude. Specifically, fluid management and fluid processing devices for biological microanalysis and drug delivery are important branches of the many emerging applications of MEMS/NEMS. A thorough understanding of whether or not the fluid confined in the nanoscale still behaves as its bulk state is crucial to the successful application of these devices.

2.1.2 Nanoscale Lubrication

Due the massive increase in information capture and storage seen in the past several years, it has been necessary to create devices with a great storage capacity such as the high storage hard drive. This is a challenge to scientists and engineers in a similar manner to other MEMS/NEMS devices because as the on-disk data density increases exponentially, the distance between the read head and disk decreases exponentially[30]. The lubricant fluid is thereby confined to a smaller and smaller slit, which is the same challenge seen in cre-

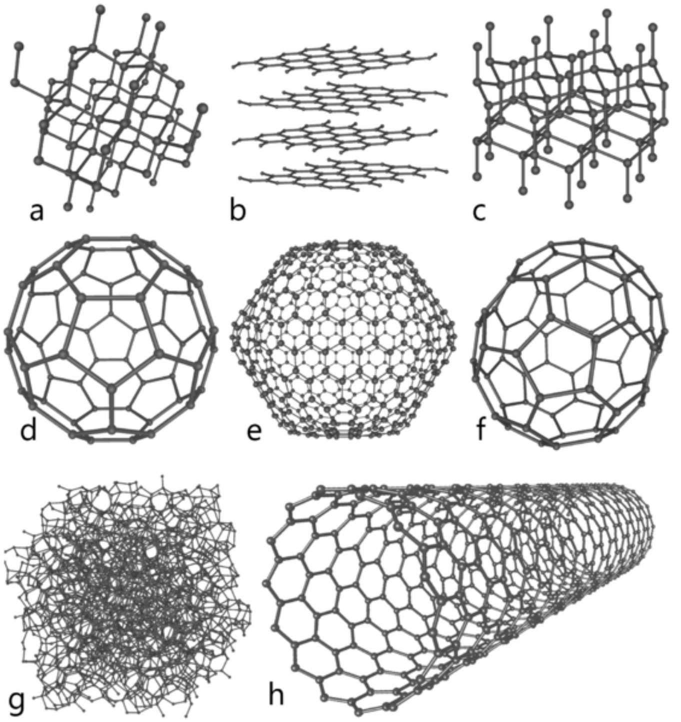

Figure 2.2. Illustration of all eight carbon allotropes by Mstroeck[29]. Buckyballs, graphene, and carbon nanotubes are perfect components for constructing electromechanical devices.

ating nanoscale electromechanical devices. More explicitly stated the challenge is, under extreme confinement, does the lubricant fluid still keep the same lubricating property as its bulk state? In other words, given that the distance between the read head and disk is lower than a certain critical value, does the lubricant fluid transition into other phases? If a solidification does in fact take place, then it likely means the upper bound storage capacity of this kind of hard drive .

2.1.3 Biological Application

A thorough understanding of nanoconfined fluid behavior also has great importance in medicine and biology. For example, synovial joints have very low friction over a large normal pressure range[31]. However, the mechanism of super lubrication of natural synovial fluids is not fully understood[32]. More research into understanding how a fluid nanoconfined between two surfaces behaves in nature will certainly facilitate the development of a new generation of artificial joints that could effectively mimic the ultra-low slide friction of natural synovial joints.

Another application is in attempting to answer one of the basic problems in biological science: the origin of life. It is widely accepted that there existed a RNA world that was the precursor of our current life which is based on a combination of DNA , RNA, and protein[33,34]. As for the origin of the RNA world itself, the pioneering experiment by Miller and subsequent similar experiments[35,36] already addressed the question of how the nucleotide is formed. However, the chemical mechanism that occurs between a nucleotide and the formation of RNA (or oligonucleotide) remains unclear. Given the existence of mica sheets soon after the Earth's formation, and the similarity of a confined fluid region to a Golgi apparatus[37], it would be interesting to investigate the physical change of nanoconfined behavior on the chemical properties as well as the possible role of confined fluids in this mechanism.[38]

2.1.4 Importance in AFM Operation

One product of the advances in MEMS technology, the invention of AFM in 1981, earned its inventors, Gerd Binnig and Heinrich Rohrer (at IBM Zrich)[39], the Nobel Prize in Physics in 1986. Since then, AFM has become one of the foremost tools in nanoscience. It provides true atomic resolution not only in a ultra-high vacuum condition, but also in an ambient environment. Due to the presence of a fluid layer on the surface[40,41] in ambient conditions, the study of nanoconfined fluid behavior is considerably important to AFM applications. Specifically, if a nanoconfinement-induced solidification takes place in the confined region between the probing tip and sample surface, it could potentially cast doubts on some AFM measurement results. As such, a modified and updated form of AFM is already an important tool in the investigations on nanoconfined fluid phenomena.

2.2 Controversy among Experimentalist

2.2.1 Introduction to SFA/SFB

While the first experimental studies of nanoscale confined fluids were performed by Israelachvili and Adams[42,43] in the 1970s, the first step in the study of such systems is attributed to the work of Tabor and Winterton[44,45], who, in the late 1960s, developed a method of determining the force between surfaces separated by nanometers. While the focus of their research was not nanoconfined fluids (rather it was to measure the attractive van der Waals forces between surfaces in air), the technique they developed overcame a number of important obstacles in the study of nanoscale systems. Building upon the work of Tabor and Winterton, Israelachvili and Adams[42,43,46] developed an improved apparatus capable of not only measuring both attractive and repulsive forces, but of doing so over a six orders of magnitude range of forces. This improved experimental approach became known as the surface force apparatus (SFA) and it, together with further improvements, has formed the basis of nanoconfined fluid research from the 1970s to date.

Among the most important improvements to the SFA technique of Israelachvili and Adams has been the ability to measure the effect of surface shear on the confined fluid. Such an adaptation has been performed by a number of groups with the most famous being that proposed by Klein and co-workers[6,16,47] (referred to as a surface force balance) and Granick and co-workers[48] (retaining the name of surface force apparatus). For comparison, Figure 2.3 provides schematics for the experimental setups of the groups of Granick (Figure 2.3a) and Klein (Figure 2.3b). In both cases the apparatus essentially consists of two surfaces, immersed in the fluid to be studied, coupled to a means of inducing oscillatory shear. In the case of the SFA (Granick) this is a piezoelectric bimorph strip, while the SFB (Klein) uses a piezoelectric tube (PZT), however, the end effect is similar (i.e. oscillatory shear). By measuring the resistance to this shear induced motion it is possible to infer a frequency-dependent viscosity that, in turn, may be extrapolated to zero-shear to obtain a measure of the viscosity of the confined fluid. It is by observing changes in this viscosity measurement, together with the previously mentioned measures of the attractive and repulsive forces between the confining surfaces, that the structure of the confined fluid is inferred.

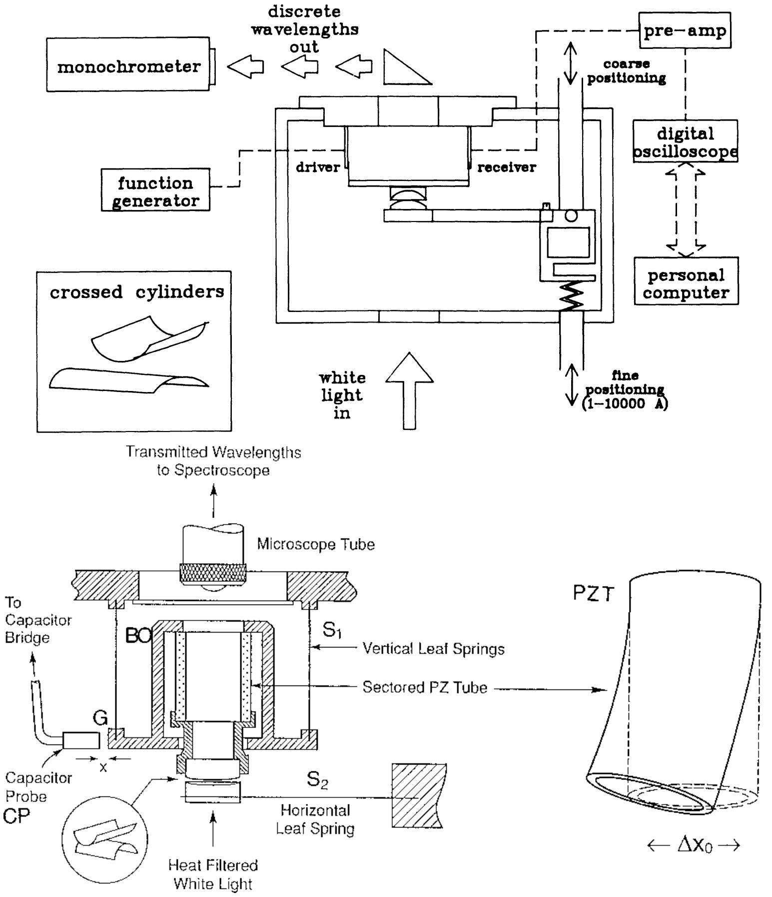

Figure 2.3. Schematic representations of surface force apparatus (SFA) and surface force balance (SFB) employed by Granick et al. and Klein et al., respectively. In SFA (top, taken from Granicks paper[48]), the shear is driven by the left piezoelectric bimorph strip (driver) and a voltage is measured as the right piezoelectric bimorph strip (receiver) detects the response of the desired system. In SFB (bottom, diagram taken form Kleins work[16]),the piezoelectric tube(PZT) provides a lateral motion (along x direction) to the top mica surface and the force is monitored by the capacitance of G.

2.2.2 Conflicting Results from SFA Community

Application of SFA to study the behavior of nanoconfined fluids was initially concerned with understanding fundamental issues, such as friction, lubrication, and adhesion. These studies focused on what are often referred to as ultra-thin films (typically corresponding to a surface separation of 3 molecular diameters or less). During this course of research it was discovered that when nonpolar fluids, such as linear and cyclic alkanes, are confined between surfaces separated by distances approaching several molecular diameters, their properties are dramatically different to those of their corresponding bulk state[6,49–52]. Specifically, it was noted that for a variety of non-polar fluids, confinement to this level (3 molecular diameters or less), at conditions in which they are normally in a liquid state, resulted in behavior consistent with that of a solid.

The ordering of a liquid immediately adjacent to a solid surface was originally introduced by Hardy in 1912[53]. Subsequently, Reychler, Harkins, and Langmuir supported and popularized this idea[54]. It is now universally accepted that the layer of a liquid closest to a surface consists of a monolayer of oriented molecules due to the constraint provided by the solid wall.

The observation of this unexpected solid-like behavior in the nanoconfined region spurred an increase in research efforts aimed at understanding the nature of the transition from fluid-like to solid-like behavior and the 1990s saw a number of such SFA and SFB studies[6,7,16,47,51,55–58]. Unfortunately, the results from the various experimental laboratories performing these studies were not in agreement and led to two conflicting theories. The first of these two theories is proposed by Klein and co-workers[6,16,47,55,56] and states that the transition is first-order as a function of surface separation (shown in Figure 2.4). The second theory is proposed by Granick and co-workers[7,51,57] who believe that the transition is second-order and thus equivalent to vitrification. Of course, both theories are supported by the experiments performed in each group. Specifically, those who espouse a first order transition observe a many orders of magnitude increase in viscosity, together with the abrupt onset of a non-zero yield stress. By contrast, proponents of a second-order transition observe only a dramatic increase in viscosity (i.e., a finite yield stress is not observed).

Since these two competing theories were proposed in the 1990s, there have been several efforts that attempt to reconcile the observed differences between what should essentially be identical experimental measurements. Unfortunately, to date, none has been successful and, for nearly two decades, a robust debate over this issue has taken place in the literature. By necessity, given the inability to observe directly what occurs between the confining surfaces, much of this debate has revolved around reducing perceived sources of error in the experimental apparatus. For example, Granick considers his early experiments that represented many-order of magnitude increase in viscosity to be compromised due to contamination of the mica sheets by platinum nanoparticles (the mica sheets were cleaved using hot platinum wire)[7,59–62]. Repeating these experiments using a different surface preparation method that eliminated platinum nanoparticle contamination, Granick and coworkers found different orders-of-magnitude increase in the viscosity depending on the confinement rate[7]. By contrast, Klein found no evidence of such problems in his experiments[56] and, ironically, the agreement with the new experiments of Granick was worse, not better.

While the new, platinum free, experiments from the Granick laboratory were unable to measure a non-zero yield stress, they did provide some new insight into confinement induced phase transitions. Specifically they observed that, for octamethylcyclotetrasiloxane (OMCTS), the occurrence of a many order-of-magnitude increase in viscosity was dependent upon the rate of approach of the confining mica surfaces; a "rapid" confinement (0.5-2.0 $nm \cdot s^{-1}$)) resulted in an increased viscosity while a quasi-static (< 0.01 $nm \cdot s^{-1}$) confinement resulted in a very low viscosity (shown in Figure 2.4). While this result has been disputed[63], it has been noted that such an observation is consistent with the formation of a jammed, non-equilibrium state[64]. If this is the case, it seems logical that the definition of "rapid" is a function of both the nature of the confined fluid as well as the size of the confining surfaces and that variations in these may account for the occurrence of jamming effects in some, but not all, experiments.

Given that the experimental apparatus used in each laboratory is of a custom design and build, the differences between them is, of course, not limited to just platinum particles or surface size effects but, rather, consists of a plethora of variations whose importance is unknown or contested (e.g. the role of fluid purity[16]). However, at its heart, the biggest hurdle to determining conclusively the change in the structure of a fluid upon nanoconfinement is that current experimental techniques lack the molecular resolution required to observe directly what occurs.

2.2.3 Results of AFM Experiments

In addition to the intense research efforts from the SFA/SFB community, researchers of other communities, using different experimental techniques, studied similar problems. In particular, atomic force microscopy (AFM) has also been applied to study the confinement of organic fluids[65–67]. Atomic force microscopy (AFM), when compared to SFA/SFB, has a much smaller contact area than either. AFM, and modified versions of this technique[40], allows for a wider choice of substrates, geometry, and the possibility of simultaneously measuring other properties with other equipment.

These AFM studies[65–67] found that the viscosity of a confined organic fluid stays bulk-like down to three molecular layers, before exhibiting enhancements in the viscosity as the last 2 fluid layers are expelled[67]. These results are similar to the work of Granick and coworkers, although it is necessary to note that pyrolytic graphite confining surfaces were used instead of mica. However, Mugele and coworkers[68] have raised questions about the suitability of AFM in the study of confinement-induced solidification. Specifically, due to the non-monotonic nature of nanoconfined fluid properties, they found that the typically assumed relation between molecular diffusivity and the damping measured by the AFM tip does not hold for nanoconfined fluids. More importantly, the manner in which AFM conducts measurements, by using up and down clicking movements instead of a lateral motion as used by SFA/SFB, might mean that AFM overlooked a possible solid phase. When taking into account that the absolute FE calculations in Chapter VI suggests a fluid/solid oscillatory nature as the separation is reduced below the critical value, the probability is high that AFM experiments actually miss the nanoconfinement-induced solid.

2.2.4 Other Techniques

Over the last two decades, in addition to significant advances in SFA/SFB techniques[69], several alternate methods have been applied to the study of nanoconfined fluid behavior including neutron scattering, X-ray[70] (solid surface deformation x-ray or neutron scattering), and differential scanning calorimetry (DSC). However, due to the extremely small amount of material in the nanoconfined region, background noise can have a substantial impact leading to results that are less than conclusive and even meaningless. Moreover, DSC itself is a tool that lacks sufficient precision to quantify such properties. To date, there still remains no general agreement between major experimental groups with respect to the existence of a sharp order-disorder transition as a function of surface separation.

2.2.5 Consistency in Nanoconfined Water Behavior

Given its fundamental importance in life, as well as its significance in physical, chemical, and biological properties, water has always drawn intense interest in related research. A similar scenario as described previously is also seen in the investigations on nanoconfined water systems. However, while there is no general agreement on the nature of nanoconfined non-polar fluid behavior, conclusions from studies on nanoconfined water behavior are quite consistent, both in simulation and experimental groups. Raviv et al.[71] in 2001 reported experimental results for water nanoconfined between mica sheets. Different from nonpolar organic fluid, such as OMCTS, cyclo-hexane, etc., water does not exhibit a many orders-of-magnitude increase in effective viscosity nor does it have a noticeable yield stress. Following that, the same conclusions have been reached by Leng and Cummings[72,73] in molecular simulation studies of water nanoconfined by mica sheets.

This behavior of water primarily stems from its strong, directional hydrogen bonds. The lack of increase in the viscosity of water can be well explained using the nanoconfined phase transition theory by Radhakrishnan et al.[74]. Due to the existence of hydrogen bonds, the interaction between water molecules is much stronger than nonpolar fluids. The interaction between water molecules and solid water does not overwhelm the interaction between water molecules. Hence, there is no freezing/melting point increase based on Radhakrishnan's theory. Additionally, the hydrogen bonds are highly directional. Water in a fluid state actually consists of water clusters[75] rather than single molecules. Extra energy is needed to break clusters and form a solid structure that might not be favored by hydrogen bond direction.

2.3 Simulation Research

2.3.1 Pros and Cons of Simulation

While the problem of direct observation of what occurs when a fluid is nanoconfined between molecularly smooth step-free surfaces (typically mica sheets) is a major hurdle that experimentalists have yet to overcome, for molecular simulations, which have an inherent molecular resolution, no such issue exists. Additionally, molecular simulation is free from the interference of uncertainties, such as previously unknown platinum contamination. Also, results by molecular simulation are relatively easier to reproduce between different research groups. Thus, in the study of nanoconfined systems, molecular simulation is an extremely powerful tool capable of providing direct evidence in the debate over the physics of confinement-induced phase transitions.

In fact, a wide range of computational studies have already been undertaken with the aim of obtaining such evidence. However, although molecular simulation techniques may not suffer a lack of resolution, they are not, of course, without their limitations and weaknesses. Most models employed in simulations are not atomistically detailed and may not completely grasp the key features of systems under investigation. Thus, while studies to date have provided useful insight, they have yet to prove in a sufficiently convincing manner the nature of confinement induced phase changes (i.e., the debate still persists). Given that this dissertation research is based on molecular simulation, we will now describe briefly some of the more prominent simulation studies as well as noting their apparent weaknesses.

2.3.2 Results from Simple Models

Pioneering simulation studies on nanoconfined fluid have been carried out by Thompson et al.[76,77] in the early 1990s, even before conflicting observations were reported experimentally. However, their original focus is the dynamic features of lubricants. By mimicking scenarios in experiments, they tried to gain insight on the origin of distinct dynamic features. The by-product of this work was the nanoconfinement-induced crystalline structure in static state and support of the as-yet-undisputed phase transition.

More comprehensive investigations were performed by Gao et al.[78–81] in the late 1990s. Gao et al. developed and applied the grand-canonical molecular dynamics (GCMD) technique to the study of systems between two face centered cubic (FCC) gold surfaces. Their simulations clearly show that when the separation between the two confining surfaces is less than 5 or 6 layers (i.e. for the commensurate system (with $\sigma_{mm} = \sigma_{wm}$), the critical thickness is 6 layers, while for the incommensurate system (with $\sigma_{mm} \neq \sigma_{wm}$), the critical thickness is 4 to 5 layers) the confined fluid exhibits features characteristic of solid-like response. Their study of the commensurate system is consistent with the reported fluid-to-solid-like transition of 6-layer thick octamethylcyclotetrasiloxane (OMCTS)[6] fluid film in Klein's surface force balance (SFB) measurement. Moreover, their views of the structure for sufficiently confined n-hexadecane not only exhibit well-layered configuration perpendicular to the gold surface, but also in-layer order.

Seminal work by Radhakrishnan and Gubbins[74,82] examined the behavior of a model system composed of Lennard-Jones (LJ) spheres under confinement, providing strong evidence of the existence of a first-order phase transition. In particular, their studies employed umbrella sampling to calculate the relative free energy difference between a confined disordered phase and a confined solid phase, demonstrating that the solid phase was lower in free energy over a wide range of state points. They additionally demonstrated that the order-disorder transition temperature shifts to higher values as the wall-fluid interaction exceeds the fluid-fluid interaction.

Also relevant are the work of Cui et al.[83–86], who provide further evidence supporting a first-order phase transition, and that of Jabbarzadeh et al.[87,88] who argue that the high friction fluid film is metastable rather than a thermodynamically stable state, and thus the transition is second-order. Making use of a united-atom model[89] for dodecane and a simple FCC lattice for the mica surfaces, both of them made a number of important observations. In the work of Cui et al.[83–86], they first note that the formation of an ordered solid-like structure upon nanoconfinement depends upon the relative strength of the wall-fluid interaction, occurring only when the wall-fluid interaction is sufficiently strong. Second, they demonstrate that if the wall-wall interaction is fitted to the experimental surface energy of mica (i.e., the surface energy of the freshly cleaved mica surface is from 200 to 400 mJm^{-2}[47]) then the wall-fluid interaction is strong enough to support the formation of an ordered solid-like structure, when dodecane is confined to 6 molecular diameters or less. Furthermore, they show that this transition is first order as a function of surface separation (i.e., for 7 layers dodecane remains fluidic) as well as determining that the confined structure consists of layers of dodecane in a herringbone arrangement (shown in Figure 2.5). In contrast with observations of Cui et al., Jabbarzadeh et al. find that the ordered solid-like structure is in a metastable state in their nonequilibrium molecular dynamics (NEMD) simulation, and they demonstrate an even more stable super-low-friction state for their specific system similar to the phenomenon reported by Zhu and Granick[90]. However, the shear rates in the Jabbarzadeh et al. work are many orders of magnitude greater than the Zhu and Granick experiment, casting doubt on whether they are related phenomena. Hence, the debate which originally focused on experiments has somewhat expanded to simulations.

2.3.3 Evidence from Atomistically Detailed Model

However, as noted above, all of the simulation studies to date are open to criticism for a number of reasons. Firstly, the models employed in such simulations are not atomistically detailed or physically realistic. In all of these previous works[78–81,83–88], the fluid molecules are described as united-atoms[92], which treat methyl and methylene groups as single interaction sites and are thus not sufficiently detailed. Additionally, it is not physically realistic to assume that the mica sheets only consist of simple LJ atoms located in face centered cubic (FCC) lattice sites statically. In contrast to gold, the mica surface is not FCC in nature[93]. Given this, it can be argued that the observed phenomena may be different to what occurs in experiment. Secondly, the timescale of these simulations is also limited, all in the range of 300ps to 100ns, which means the observed well-ordered structure could be a metastable state.

Recently, Docherty and coworkers[89,94] addressed the first problem for nanoconfined non-polar fluids. In their simulations, they used a fully atomistically detailed model for both the fluid (dodecane and cyclohexane[95]) and solid (mica[93]), and demonstrated that the nanoconfined fluids undergo a rapid and dramatic transition to a layered and ordered structure (shown in Figure 2.6). And as a reassessment of previous assumptions, they found that a hexagonal ordering of the sufficiently confined cyclohexane could be induced by the hexagonal nature of the mica surface. These are the most convincing results among those investigations to date, but the problem still remains of whether the ordered phase observed in the molecular simulations is thermodynamically stable or metastable due to these studies being conducted in the previously mentioned timescale range. A rigorous solution to this problem will be the development and application of FE calculation techniques to the study of nanoconfined systems. Therefore, FE calculations need to be performed to show whether the ordered phase observed in molecular simulation is in a thermodynamically stable state.

2.4 Free Energy

2.4.1 Criteria for Defining a Solid

In order to determine if there is a fluid-to-solid phase transition, the primary concern then becomes how is a solid/crystal phase defined. Simionesco et al. have reviewed criteria that are generally implemented in solid determination[96]. Some examples include the Hansen-

Verlet criterion that the magnitude of the structure factor at its first peak is 2.8[97], the Lindemann criterion that the amplitude of vibration of the atoms is not sufficient to invade the space of their nearest neighbors[98], and the Born criterion that shear strength characteristic of solids is present[99]. However, all of these criteria are defined on a kinetic basis and might not be thermodynamically conclusive.

2.4.2 Pivotal Role of FE in Thermodynamics

FE plays a fundamental role in thermodynamics. The FE of a system is the quantity which is minimized at equilibrium. For example, at constant pressure (P), temperature (T) and number of molecules (N), the Gibbs FE (G) is minimized; since a systems Gibbs free energy can in some cases be lowered by splitting into two phases (e.g., vapor and liquid), minimization of Gibbs FE is an important principle in understanding phase equilibrium. Another example are systems at constant volume (V), temperature (T), and number of molecules (N), in which case the Helmholtz FE (A) is minimized. If the relative thermodynamic stability of two phases is required at a given condition, such as density (ρ) and temperature T and N, a simple comparison of Helmholtz FE (A) would fulfill that. Provided that the FE is known with sufficient accuracy, theoretically, a conclusive determination of the stable structure and full description of the phase behavior of the system of interest would be straightforward.

2.4.3 FE Determination Methodologies

Given the importance of FE, however, the calculation of FE, even for a relatively simple system, can be a cumbersome or even impractical task. The direct measurement of FE in experiment and simulation, like pressure or temperature, is not possible. FE is a measure of the volume in phase space that a system can access rather than a mechanical property expressible in terms of position and momentum of molecule[100]. Hence, the study of FE calculation is itself a large and expanding topic of great interest. Following the introduction of novel methodologies and exponentially increasing computational capability in the last several decades, significant advances in FE determination have been made for a variety of systems, from early stage idealized particles to water, from sparse fluid to dense solids[101], from pure systems to mixtures[102,103]. To date, a plethora of elegant free energy determination approaches have been proposed, validated, and widely implemented[104–106,106–109].

2.4.3.1 Fluid FE Calculation

FE calculation for a fluid is relatively straightforward. The most classic method is thermodynamic integration. By employing a path that reversibly connects the fluid of interest with a free energy known state (i.e., FE reference), typically an ideal gas, the thermodynamic integration measures the FE difference between the system of interest and this FE reference. Subsequently, a simple summation of the FE difference and the FE of reference state will give the FE of the fluid under study. The integration is not limited to trace a reversible path that real experiments could follow. More often than not, the integration is performed along a path that actually does not exist in reality, and is only accessible in simulations. One example is an integration path with varying bond strength while other parameters remains constant. This method was given a new terminology, Hamiltonian integration[101], and is very useful in FE measurements.

Another robust fluid FE calculation approach, known as the particle insertion method, was proposed in 1963. It is also widely known as the Widom insertion method[109]. By randomly inserting a never-accepted test particle into an N-particle system, the Widom insertion method evaluates the excess chemical potential (μ_{ex}) of the N-particle fluid system using the following equation:

$$\mu_{ex} = -k_B T \ln \int ds_{N+1} \left\langle \exp\left(-\beta \Delta U\right) \right\rangle_N \tag{2.1}$$

where, k_B is the Boltzmann constant, T is temperature, s_{N+1} is scaled coordinate, β is equal to $1/(k_B T)$, ΔU is the interaction energy between the inserted test particle and the remaining molecules, and $\langle ... \rangle$ denotes the canonical ensemble average over the configuration space of this N-particle system. The summation of the excessive chemical potential (μ_{ex}) and the chemical potential of ideal gas under the same condition (μ_{id}) gives absolute FE. Moreover, attention should be given to the fact that the tail correction used in the potential calculation here is twice that of the generally used one. The Widom insertion method is especially useful for FE calculations on dilute or moderately dense fluid. However, it should be noted that if the system under investigation is dense, the frequency of important insertion would be extremely low thereby rendering FE measurements by this method impractical.

2.4.3.2 Solids FE Calculation

Partly due to the relatively high density of solids and the hysteresis that occurs in the phase transition, especially in simulation, determining a robust strategy to connect an arbitrary solid under investigation to a known free energy reference in order to determine its absolute FE takes a much longer time and more research effort than for fluid. Hoover and Ree[110,111] carried out pioneering work in the late 1960s by introducing the single-occupancy cell method. This method models the dense solid as a lattice gas that the particle moves within its cell and lets the lattice gas uniformly expand to low densities without a first-order transition. Only two years later, Hoover, Gray, and Johnson[104,105] proposed an alternative method by cooling the solid into a harmonic crystal. However, both the single-occupancy cell method and the cooling method have limitations. Research a few years later[112] proved that the uniform expansion may not be free from hysteresis and the cooling method probably encounters phase transitions in the molecular solid cooling process. Hence, a robust new method that is free from these limitations is needed for solid FE measurement.

In 1984, Frenkel and Ladd[106] proposed a novel method which employed an analytically known FE - the Einstein crystal that is structurally identical with its target solid as the reference state (the method is named after this reference state). This method then measures the free energy difference between the reference and solid of interest by introducing two stages. Since the reference and solid of interest are structurally the same, the Einstein crystal method avoids the first-order phase transition along the integration path to the largest extent possible. Currently, it has already become the standard method for solid FE calculation[101]. Subsequently, another straightforward and robust method was introduced by Wilding and coworkers[113–115] known as the phase switch Monte Carlo method. It determines the FE difference of two phases by using an extended sampling in just a single MC run. However, the phase switch Monte Carlo method is not feasible for measuring two systems with a large FE discrepancy. Meanwhile, the Wang-Landau Method[107], which was named after its author, has also been proposed. Sharing some similarities with the switch Monte Carlo method, the Wang-Landau Method adjusts the weighting factor in MC simulations to get the density of states and then calculates the FE difference. Most recently, Kofke and coworkers have developed a very efficient harmonically targeted temperature perturbation (HTTP) method[108,116] which is aimed at FE calculation for arbitrary solids. It determines its reference system by cooling the solid to a sufficiently low temperature in order to create a solid that behaves like a harmonic crystal whose FE can then be analytically calculated. Therefore, the HTTP method partially inherits the limitations of the cooling method, including the possible phase transition in the cooling process and the probability of an unreachable harmonic crystal. Additionally, the usage of HTTP is limited to systems with a continuous potential because the existence of the first derivative of the potential function is a prerequisite for FE calculation.

To date, a large amount of research has been devoted to the investigation of FE calculation techniques, which has promoted the improvement of these methods. The majority of these methods are focused on FE calculations for a specific group of systems, while others attempt to be more generally applicable. Meanwhile, FE measurements for classic ideal systems have already been widely conducted. For instance, a large amount of FE data for ideal hard spheres systems[106,107,117–121], LJ fluids[122], and crystals[123,124] are available.

However, these methods are typically developed for the study of bulk systems and none of them are directly applicable to the specialized case of nanoconfined fluids. Thus, in order to determine the FE for nanoconfined systems, further development of the most applicable method is required.

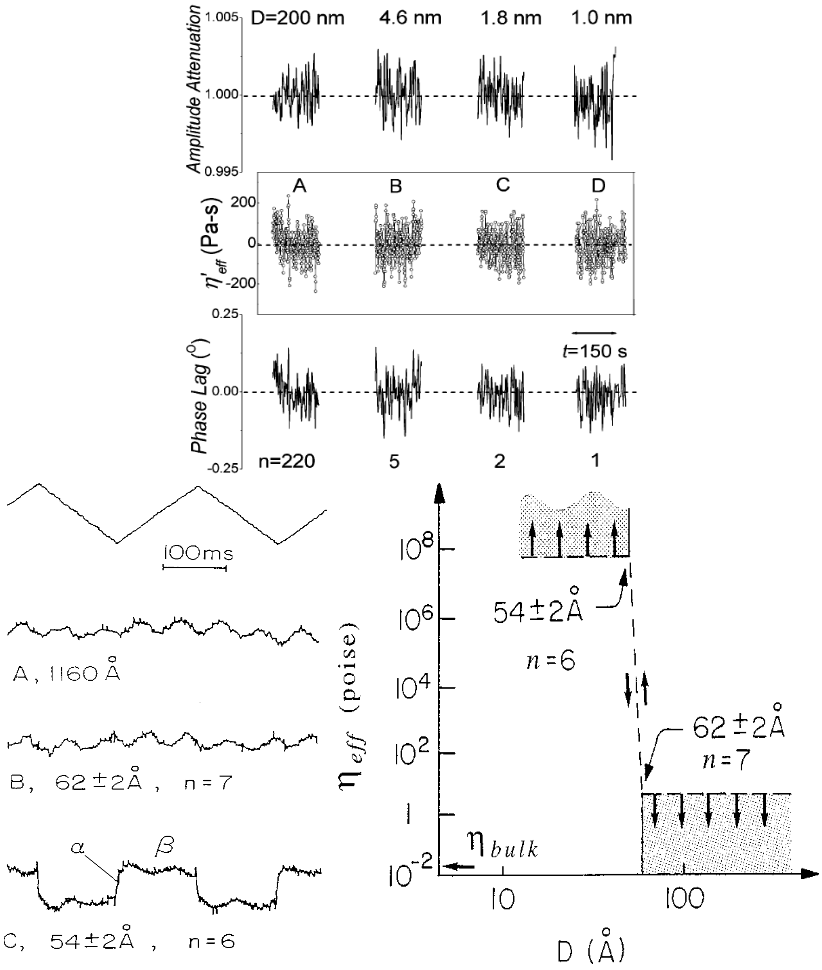

Figure 2.4. Conflicting results presented by Granick et al.[7] and Klein et al.[16]. Quasistatic compression (top) is from the work of Granick et al.[7]. There is no dramatic elastic-viscosity shift as the separation decreases from 220 nm to 1 nm. Applied motion and feedback signals at various separations (bottom left) and effective mean viscosity as a function of separation (bottom right) are observed by Klein et al.[16]. The abrupt increase and decrease of feedback signal (left, C) at six molecular layers indicate a non-zero yield stress. Moreover, effective mean viscosity demonstrates an orders of magnitude increase as the separation is equal to or less than six molecular layers.

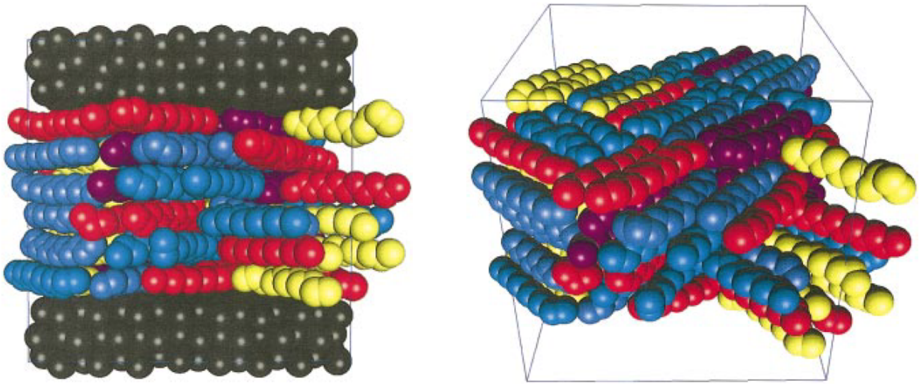

Figure 2.5. Snapshots of the nanoconfined dodecane at a separation equal to six molecular layers (from Cui et al.[85] work). A side view (left) of n-dodecane (SKS united atom model[91]) fluid nanoconfined by mica (FCC(100)) surfaces. A perspective view of the same configuration, showing a herringbone in-layer arrangement with 90° angle.

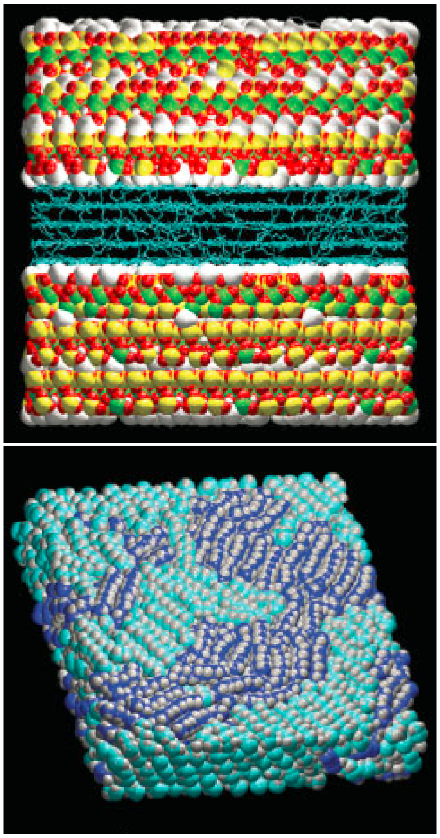

Figure 2.6. Snapshots of the nanoconfined dodecane at a separation equal to five molecular layers (taken from Cummings et al.[94] work). A side view (top) of n-dodecane (OPLS all-atom model) nanoconfined by mica (Heinz *al*.[93]) sheets. A perspective view (bottom) shows a herringbone in-layer arrangement with 120° angle.

CHAPTER III

SIMULATION AND FE CALCULATION METHODOLOGY

3.1 Choice of Models and Methodology

The focus of this dissertation research is in developing absolute FE calculation strategies for nanconfined systems and subsequently employing the FE measurement as a tool to determine the nature of nanoconfined phase behavior. Specifically, the motivation is to decisively resolve the two-decades-long debate in both experimental and simulation communities and determine whether the layered and ordered state of the nanoconfined fluid observed in molecular simulation is thermodynamically stable. This work is done via the absolute FE determination and FE comparison of corresponding states.

3.1.1 Models

Prior to choosing a reasonable interaction model in FE calculation for a nanoconfined fluid, a quick review of the materials used in previous experiments is necessary. As for the solid wall, molecularly smooth mica sheets typically have been used. Mica has a hexagonal sheet-like arrangement of its atoms. Its structure and chemical component have been known for quite some time[125]. Currently, modern standard measurements, such as nuclear magnetic resonance (NMR) spectroscopy, X-ray diffraction, X-ray spectra, and Infrared (IR) spectroscopy[126], can be used to easily determine the structural properties of mica. However, it is important to note that the chemical formula of mica is not fixed, and a detailed composition depends on its type and where it was mined. Based on the experimental data and previous work, Heinz and coworkers[93] have developed a widely compatible force field for mica and similar phyllosilicates. However, the computational cost associated with the Heinz model makes it intractable for FE calculations. Simplifications, such as assuming a uniform FCC crystal, with interaction strength mapped to realistic interactions, has been used in other work[83]. This puts the relative strength between a methyl group and mica at 4.47 times that of methyl-methyl groups. Meanwhile, the typical organic fluid used in experimental study is OMCTS, a molecule that has a flat sphere configuration (shown in Figure 3.1) and serves as a model liquid for Lennard-Jones (LJ) fluids.

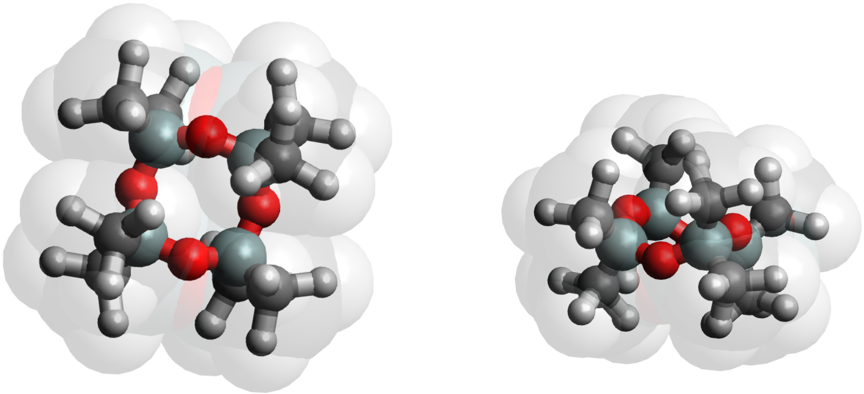

Figure 3.1. Top (left) and side (right) view of OMCTS by Avogadro package[127]. The color coding of atoms is: red - oxygen, light grey - hydrogen, dark grey - carbon, and dark blue - silicon.

Since the absolute FE determination is simulation based, a brief comparison of previously used models and their conclusions are presented in Table 3.1. Taking into consideration the setting differences in the simulations, such as the specific system under study, wall-fluid interaction, wall-fluid size ratio, and surface orientation, results by a simplified model demonstrate good consistency with those using an atomistically-detailed model. For instance, the layering and ordering transition of the sphere and sphere-like fluid cyclohexane molecule takes place around 4 to 5 molecular diameters. This indicates that the simplified model already captures key features of nanoconfined fluid behavior.

Table 3.1. A comparison of models implemented and results obtained in previous simulation studies.

	System	Fluid	Solid	σ_{wm} $/\sigma$	ε_{wm} $/\varepsilon$	Critical Thickness /layer	In-layer Order
Gao	commensurate	LJ	LJ-FCC(111)	1.00	2.40	~ 6	
	incommensurate	LJ	LJ-FCC(111)	0.89	2.40	$4 \sim 5$	
Cui	dodecane/mica	SKS	LJ-FCC(100)	1.06	4.47	6	90°
Docherty	dodecane/mica	OPLS-AA	Heinz			9	120°
	cyclohexane/mica	OPLS-AA	Heinz			5	120°@4layer

Consequently, taking into consideration the computational cost in FE calculation (especially since the method used in this work takes twenty simulations to carry out a single FE measurement), the classic 12-6 Lennard-Jones (LJ) potential is employed to model interactions in the nanoconfined system.

$$U = 4\varepsilon_{ij}\left[\left(\frac{\sigma_{ij}}{r}\right)^{12} - \left(\frac{\sigma_{ij}}{r}\right)^{6}\right] \tag{3.1}$$

Where U is the potential, ε_{ij} is the potential well depth, σ_{ij} is the interatomic distance at which the potential energy is equal to zero, and i and j denote the type of atom. Generally, w and m are used in this work to denote the solid wall particles and the fluid particles, respectively. Mostly in this research, Berthelot-Lorentz Combining rules are applied, except for FE calculations of the incommensurate systems in section 5.4. Additionally, it is important to note that all of the following work uses LJ reduced units, except for the explicitly specified scenarios. The interaction used in the subsequent work are designed to closely mimic the parameters used for systems such as mica and OCTMS, yet still be generally applicable.

3.1.2 FE Calculation Methodology

As reviewed in Chapter II, the phase switch Monte Carlo method[114,115] is straightforward and efficient but limited to low FE discrepancy measurements, with the Wang-Landau method sharing similar limitations. The newly developed HTTP method[108,116] takes continuous potential as the prerequisite and, as such, is not suitable for molecular solids. However, by employing a FE-known Einstein crystal (shown in Figure 3.2a) that is structurally identical with the solid of interest as the reference state, the Einstein crystal method[106] cleverly minimizes the probability of abrupt configuration shifts and thus far largely decreases the possibility of problems arising from phase transitions along the integration path. Although it is not as efficient as the phase switch Monte Carlo method, it is applicable for arbitrary solids. Thus, in this dissertation research, FE calculations are done using the Einstein crystal method as the starting point. The essential parts of this dissertation research are evaluating existing basic algorithms of the Einstein crystal method, developing modified algorithms, adapting these algorithms to the FE measurement, and employing FE as the tool to reveal the nature of nanoconfined fluid behavior.

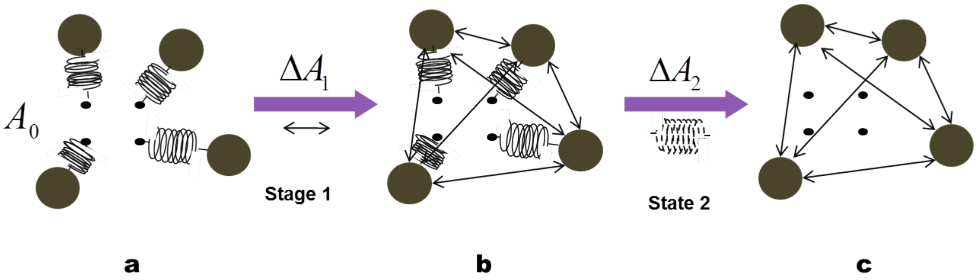

Figure 3.2. Schematic illustration of the Einstein crystal method. (a)Einstein crystal, (b)Einstein solid, (c)solid of interest. Stage 1: turning on the intermolecular intercations. Stage 2: gradually turning off the harmonic potential.

3.2 Basic Algorithm

3.2.1 Introduction

The original algorithm of the Einstein crystal method was proposed by Frenkel and Ladd[106]. Since its introduction in 1984, several improvements have been introduced[119,128] and modified applications have also been reported[129,130]. The Einstein crystal method to date has become a standard and robust method of absolute FE determination for arbitrary solids. More recently, it has been revisited in detail by Vega and co-workers[101,130]. The basic algorithm employed in this work was introduced by Almarza[128], who successfully removed the fixed-center-of-mass constraint in the original algorithm, making it more straightforward and much easier to use.

Basically, the Einstein method works by designing a reversible path to connect the system under investigation with a known FE reference and measure the FE change along the reversible path to obtain the FE of the investigated system. In particular, the Einstein crystal method employs a known FE Einstein crystal as the reference, which only consists of non-interacting harmonic oscillators, and constructs the reversible path via two stages. Hence, the calculated absolute Helmholtz FE (A) of a solid of interest is generally the summation of the following terms (shown in Figure 3.2 and the formula below): the absolute Helmholtz FE analytically-known reference (A_0), the FE change in stage one (ΔA_1), and the FE change in stage two (ΔA_2). The reference state (A_0) is an Einstein crystal (i.e., non-interacting particles attached to lattice points), which is structurally identical to the solid of interest. The first stage measures the FE difference between a system of interacting particles attached to lattice points and the Einstein crystal ΔA_1 (i.e., when intermolecular interactions are turned on). The second stage calculates the change in FE associated with removal of the harmonic potential (ΔA_2), leaving a system of interacting particles.

$$A(N,V,T) = A_0(N,V,T) + \triangle A_1(N,V,T) + \triangle A_2(N,V,T) \tag{3.2}$$

3.2.1.1 FE of the Reference (A_0)

The FE of the reference state, an Einstein crystal, can be calculated analytically via simplifying and evaluating the partition function. In canonical ensemble, volume (V), temperature (T), and number of molecules (N) are constants. The appropriate expression for the partition function ($Q(V,T)$) of a N-particle reference system would be:

$$Q(V,T) = \frac{1}{N!h^{3N}} \int \exp\left[-\beta H(q,p)\right] d\omega \tag{3.3}$$

where h is the Plank constant, β is equal to $1/(k_B T)$, $d\omega$ is considered as a volume element of the phase space, and $H(q,p)$ denotes Hamiltonian of the N-particle reference (i.e., energy of the reference system). q and p in $H(q,p)$ are, respectively, position coordinate and momentum coordinate. It is important to note that the reference system employed here is not center-of-mass fixed.

Since the reference Einstein crystal consists of non-interacting harmonic oscillators, there is no energy associated with the relative position of particles. The Hamiltonian of the reference thus only includes kinetic energy (Eq. 3.4) and harmonic bond energy (Eq. 3.5) components.

$$
\begin{aligned}
H(q,p) &= \sum_{i=1}^{N}\left(\frac{p_i^2}{2m}\right) && (3.4)\\
&\quad +\sum_{i=1}^{N}\left(\Lambda_E r_i^2\right) && (3.5)
\end{aligned}
$$

where r_i is the distance between the harmonic oscillator i and its lattice point, Λ_E denotes the harmonic bond constant, and m is the mass of particles. In the following, the partition function can be rewritten as

$$
Q(V,T) = \frac{1}{N!h^{3N}}\int \exp\left[-\frac{\Lambda_E r_i^2}{k_B T}\right]\prod_{i=1}^{N}\left(d^3 q_i\right)\int \exp\left[-\frac{p_i^2}{2mk_B T}\right]\prod_{i=1}^{N}\left(d^3 p_i\right) \quad (3.6)
$$

Performing the integration, brings the partition function to Equation 3.7 and then Stirling's approximation is applied. Subsequently, the equation below (Eq. 3.8) is obtained:

$$
\begin{aligned}
\frac{A_0}{Nk_B T} &= -\frac{\ln Q(V,T)}{N} && (3.7)\\
&= \left\{-\frac{3(N-1)}{2N}\ln\left(\pi/\Lambda_E\right)-\frac{3}{2N}\ln N-\frac{3}{N}\ln\frac{N}{V}\right\}+\left\{\frac{3}{2}\ln\left(\frac{h^2}{2\pi mk_B T}\right)\right\} && (3.8)
\end{aligned}
$$

where $\frac{h^2}{2\pi mk_B T}$ is the square of the de Broglie wavelength. In this work, its value is set to unity for solid systems. Thus, Equation 3.8 could be further simplified. Finally, an analytic expression for the FE of an N-particle reference system is presented in the following equation:

$$\frac{A_0}{Nk_BT} = -\frac{3(N-1)}{2N}\ln(\pi/\Lambda_E) - \frac{3}{2N}\ln N - \frac{3}{N}\ln\rho^{\star} \tag{3.9}$$

3.2.1.2 Evaluation of ΔA_1

The FE change ΔA_1 in stage one is defined as the FE difference between the reference system Einstein crystal and the intermediate system Einstein solid. The terminology Einstein solid here is used to specify a system consisting of harmonic oscillators, but with the intermolecular interaction between particles turned on. The ΔA_1 in the Einstein crystal method is determined by the division of partition functions of the Einstein crystal and the Einstein solid (Eq. 3.10). It is calculated by conducting umbrella sampling[131] of the Einstein crystal. The expression of ΔA_1 is given in the following equations:

$$\begin{aligned}
\Delta A_1(N,V,T) &= -k_BT\ln\frac{Q_1(V,T)}{Q_0(V,T)} && (3.10)\\
&= -k_BT\ln\frac{\int\exp(-\beta U_1)\,d1....dN}{\int\exp(-\beta U_0)\,d1....dN} && (3.11)\\
&= -k_BT\ln\langle\exp[-\beta(U_1-U_0)]\rangle_0 && (3.12)
\end{aligned}$$

where U_0 is the harmonic potential energy of Einstein crystal, U_1 is the overall potential energy of the intermediate system Einstein solid (including harmonic potential and intermolecular potential energy), and $\langle....\rangle_0$ denotes a canonical ensemble average over the reference system Einstein crystal. For simplicity, U_i (shown in Eq. 3.13) is defined as the energy difference between U_1 and U_0. In other words, it is the calculated intermolecular interaction potential energy based on configurations of the reference system. In FE determination, a MC simulation is employed in this stage to conduct the sampling and calculate ΔA_1.

$$\Delta A_1 = -k_B T \ln \langle \exp\left[-\beta \left(U_i\right)\right] \rangle_0 \tag{3.13}$$

However, in practical calculations, the value of $\exp\left[-\beta \left(U_i\right)\right]$ is too large to be accurately processed by the computer. Its range is beyond current computer capability. Therefore, a subtraction is introduced to evaluate a much smaller value, $\exp\left[-\beta \left(U_i - U_{i\_lattice}\right)\right]$, to avoid this problem.

$$\Delta A_1 = U_{i\_lattice} - k_B T \ln \langle \exp\left(-\beta \left(U_i - U_{i\_lattice}\right)\right) \rangle_0 \tag{3.14}$$

where $U_{i\_lattice}$ is the intermolecular interaction energy of the reference system in the lattice configuration. Hence, Eq. 3.14 is used in the following FE calculations for ΔA_1.

3.2.1.3 Evaluation of ΔA_2

Subsequently, in stage two, the harmonic interaction in the intermediate system, Einstein solid, is gradually decoupled to reach the solid of interest. A Hamiltonian thermodynamic integration (shown in Eq. 3.15) is carried out in that process to measure the FE change ΔA_2. It is worthwhile to note that such a route is rare or non-existent in real experiments. However, it still can be simulated by the computer.

$$\Delta A_2 \left(N, V, T\right) = \int\limits_{\lambda=0}^{\lambda=1} \left\langle \frac{dU\left(\lambda\right)}{d\lambda} \right\rangle d\lambda \tag{3.15}$$

Here, λ is the coupling parameter with the value ranging from zero to unity. Zero and unity denote Einstein solid and the solid of interest, respectively. $U(\lambda)$ is the potential energy of the system of interest in the harmonic interaction turning-off process and is defined by:

$$U(\lambda) = \lambda U_i + (1-\lambda)(U_h + U_i) \tag{3.16}$$

where U_h denotes the harmonic potential energy with full bond strength and U_i denotes intermolecular interaction potential energy component. Bringing in this formula, Equation 3.15 would be simplified as

$$\begin{aligned} \Delta A_2(N,V,T) &= -\int\limits_{\lambda=0}^{\lambda=1} \langle U_h \rangle_{N,V,T,\lambda}\, d\lambda && (3.17) \\ &= -\int\limits_{0}^{\Lambda_E} \frac{\langle U_h \rangle_{N,V,T,\lambda}}{\Lambda_E} d\lambda\Lambda_E && (3.18) \end{aligned}$$

Since U_h varies by several orders of magnitude, a change of variable technique is employed here to smooth the variation of U_h and improve the accuracy. Hence, the formula 3.18 can be rewritten as:

$$\Delta A_2 = -\int\limits_{\ln C}^{\ln(\Lambda_E + C)} \frac{\langle U_h \rangle_{N,V,T,\lambda}(\lambda\Lambda_E + C)}{\Lambda_E} d\ln(\lambda\Lambda_E + C) \tag{3.19}$$

where Λ_E is the harmonic bond constant and C is a general constant. Since previous work in the literature[106,132] shows that $C = \exp(3.5)$ gives a good estimate of the integral, this value is used in the following FE calculations.

3.2.1.4 Parameters Setting

Combining previous equations together (Eq. 3.2, 3.9, 3.14, and 3.19,), the FE of the solid of interest is given by

$$\begin{aligned}
\frac{A}{Nk_BT} &= \frac{A_0}{Nk_BT} + \frac{\triangle A_1}{Nk_BT} + \frac{\triangle A_2}{Nk_BT} && (3.20)\\
&= \left\{ -\frac{3*(N-1)}{2N} \ln\left(\frac{\pi}{\Lambda_E}\right) - \frac{3}{2N}\ln N - \frac{3}{N}\ln\rho^* \right\} && (3.21)\\
&\quad + \left\{ U_{i\_lattice} - k_BT \ln\left\langle \exp\left(-\beta\left(U_i - U_{i\_lattice}\right)\right)\right\rangle_0 \right\} && (3.22)\\
&\quad - \int_{\ln c}^{\ln(\Lambda_E + c)} \frac{\langle U_h\rangle_{N,V,T,\lambda}\left(\lambda\Lambda_E + c\right)}{\Lambda_E} d\left(\ln\left(\lambda\Lambda_E + c\right)\right) && (3.23)
\end{aligned}$$

In practical simulations, the choice of harmonic bond strength (Λ_E) is not arbitrary. Too strong a bond strength will tightly bond the atoms around their lattice sites and thus lower the efficiency of sampling. Similarly, a too weak bond strength will also raise issues. The weak bond might not be able to pull back the atoms to the lattice site in certain cases, and hence either crashes the simulation or drives the term ($\exp(-\beta(U_i - U_{i\_lattice}))$) to infinity. Tested in preliminary work, the value of $1200k_BT/\sigma^2$ is used for Λ_E in most cases in this dissertation work except in scenarios in which it is explicitly clarified.

As for the FE change in Stage two, the twenty-points Gauss-Legendre quadrature formula (Eq. 3.24) is used to evaluate the integral:

$$\int_{-1}^{1} f(x)\,dx = \sum_{i=1}^{N} w_{N,i} f(x_N, i) \tag{3.24}$$

where N is the number of points of Gauss-Legendre quadrature formula and $w_{N,i}$ denotes the weight factor. This dissertation research employs MD instead of MC to sample the transition states along the integration path in order to take advantage of the computational power of parallel computing.

3.2.2 Validation

To validate the basic algorithm employed later in this work, and since it is fundamental to the following research, the absolute Helmholtz FE determination for a face centered cubic (FCC) LJ crystal under the same conditions as literature ($T^\star = 2.0$, $\rho^\star = 1.28$)[123,123,124,130,133] has been conducted. Monte Carlo (MC) umbrella sampling[131] was used in stage one (ΔA_1) and Nosé-Hoover MD simulations within LAMMPS (Large-scale Atomic/Molecular Massively Parallel Simulator) [134] to sample the state points along the harmonic potential removing stage(ΔA_2), rather than a more general MC-based approach, was used to take advantage of the efficient multiple parallel CPUs[135].

As shown in Table 3.2, the calculated FE values demonstrate a good consistency with the FE values by Barroso and Ferreira[124], Vega and Noya[130], von der Hoef's[123] equation, and Mastny and Pablo's[133] equation. This agreement verifies the basic algorithm used in this work. Among these published approaches, Barroso et al. and Vega et al. used the Einstein crystal method that employs the classic MC-based approach in the second stage, while Von der Hoef proposed a fitting formula for the absolute FE of a Lennard-Jones solid and Mastny subsequently updated constants in this formula.

Table 3.2. Comparison of calculated absolute Helmholtz FE with literature values. The system under study is a LJ FCC crystal at $T^\star = 2.0$, $\rho^\star = 1.28$. Free energy A is in units of Nk_BT, N is number of particles, k_B is Boltzmann constant, and T is temperature.

	Calculated	Barroso[124]	Vega[130]	von der Hoef[123]	Mastny[133]
A	2.618	2.596	2.601	2.623	2.606
Fitting	$2.618 - \frac{12.156}{N}$		$2.601 - \frac{7.704}{N}$		

3.2.3 Monte Carlo versus Molecular Dynamics

However, as demonstrated in section 3.2, although the calculated FE value determined by using the basic algorithm is consistent with literature values, the MD-sampling based FE in this work still shows a minor difference from the MC-sampling based values in the literature. In particular, the slope of the fitting formula by MD sampling is obviously steeper.

Among the possible factors that lead to this difference, the divergence of the intended temperature and the achieved temperature in simulation could be the source. To this end, Butler and coworkers[136] developed an approach to calculate the configurational temperature (T_{config}, shown in Eq. 3.25) to represent the achieved system temperature in canonical MC simulation. By using this formula, the T_{config} could be directly evaluated based on the system configurations in MC simulation.

$$T_{config} = -\frac{\sum_{i=1}^{N} F_i^2}{k_B \sum_{i=1}^{N} \sum_{j \neq i} \nabla_{r_{ij}} F_{ij}} \tag{3.25}$$

$$F_i = \sum_{j \neq i} F_{ij} = -\sum_{j \neq i} \frac{\partial U_{ij}}{\partial r_{ij}} \tag{3.26}$$

where U_{ij} is the potential energy between particle i and particle j, and r_{ij} is the position vector between these two particles. As revealed by Butler and coworkers, T_{config} in canonical MC is always smaller than T_{input} (*i.e.*, the desired temperature) and the discrepancy between these two rapidly decays with the increasing system size (shown in Figure 3.3), turning out less than 0.2% for 2000 particles. Although the calculated FE difference is negligible in large system sizes, the dramatic discrepancy in small system sizes still exerts an obvious impact on the slope of the linear fitting line and the extrapolated value in the thermodynamic limit (i.e., $1/N \to 0$). Hence, special attention should be paid if the FE comparison between the MC-based and MD-based calculations is conducted for small systems.

3.3 Modified Algorithm for Nanoconfined System

3.3.1 FE Calculation for Nanoconfined System

Validation of the basic algorithm was conducted in the previous section. This section subsequently extends FE calculation efforts specifically to nanoconfined systems, which is the

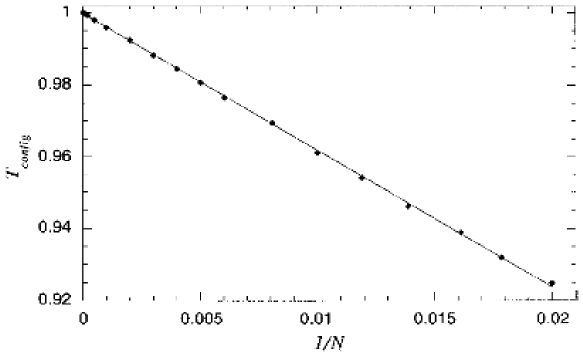

Figure 3.3. System size dependence of T_{config} in canonical MC simulation (taken from Butler et al.[136] work). T_{config} is measured by using Eq. 3.25 and it is always lower than the desired temperature ($T_{input} = 1.0$).

primary focus of this dissertation research. However, the Einstein crystal method was originally proposed for bulk solid FE calculation and current applications are limited to bulk or bulk-like systems. Therefore, modifications and scrutiny over the effects of these modifications are required to properly adapt this free energy method to nanoconfined systems.

Here, we treat wall particles in the confined system as static for simplicity. Seminal work by Dominguez and coworkers[137] has successfully employed the same assumption in Einstein crystal method based FE calculations, however, they only concentrate their study on weak wall-fluid interaction systems. This work extends FE calculations of nanoconfined systems to the scenarios much closer to the experimental conditions we are interested in (i.e., the wall-fluid interaction is approximately four times of fluid-fluid interaction). While the nanoconfined phase in a weak wall-fluid interaction system mostly retains its bulk-like property, strong wall-fluid interactions in nanoconfined systems renders the behavior of the nanoconfined phase dramatically different. It is important to note that the typical nanoconfined system investigated in this work includes a LJ solid wall and a LJ nanoconfined phase.

3.3.2 Modified Tail Correction

3.3.2.1 Introduction

The model system in this dissertation research is mostly composed of identically sized LJ spheres. The strongly differing interaction strengths make this a heterogeneous system. As such, using a standard tail correction in the nanoconfined system would result in systematic errors, making it difficult to conduct a direct comparison with other systems such as bulk phases. Besides, as shown in Fig. 4.5 in section 4.4, the potential calculation that the tail correction is involved in actually dominates the finite cutoff dependence in FE calculations.

Therefore, we introduced a well defined modified tail correction[138] to account for this. It is based on the surface area formula for spherical segments and takes advantage of one important feature of the spherical segment's surface area formula. That is, if two parallel surfaces intersect a sphere, surface area of the spherical segment between these two parallel surfaces is determined only by two parameters, the radius of the sphere (r) and the distance between these two parallel surfaces (h). In the nanoconfined system under study, these two surfaces are the wall-fluid boundary planes and h is the wall-wall separation correspondingly.

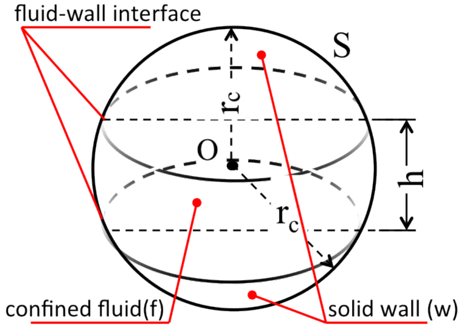

Figure 3.4. Schematic representation of the modified tail correction.

In Figure 3.4, S is the surface area of the spherical shell (including the surface area of the partial sphere in the nanoconfined phase and that in the solid wall), r_c is the cutoff distance used in potential calculation, and the subscripts m and w specify the mobile fluid particles and static wall particles, respectively.

To derive a tail correction specifically for the nanoconfined system under study, two following assumptions (shown in Figure 3.5) have been introduced. The first one assumes that the solid wall and the nanoconfined phase are homogeneous themselves although the whole system is heterogeneous. That means the densities of the solid wall (ρ_w) and the confined phase (ρ_m) remain constant for the whole system. The second assumption is that radial distribution functions $g_{wm}(r)$ and $g_{mm}(r)$ approach unity as $r \geq r_c$. Additionally, in order to guarantee that both wall-fluid boundary planes could intersect with the sphere, the cutoff radius used in the potential calculation should be equal to or larger than the wall-wall separation ($r_c \geq h$)

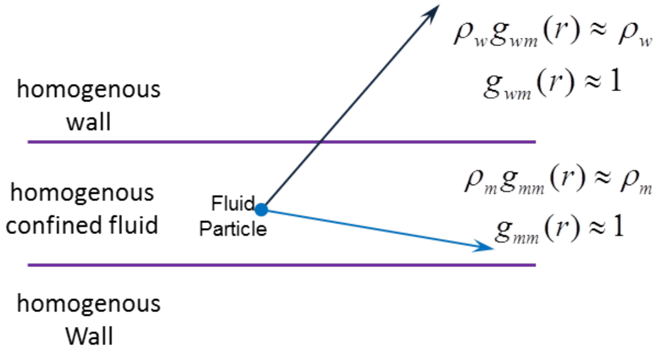

Figure 3.5. Assumptions for our modified tail correction

$$
\begin{aligned}
U^{tail} &= \frac{1}{2}\int_{r_c}^{\infty} dr\rho SU(r) \\
&= \frac{1}{2}\int_{r_c}^{\infty} dr\left[\rho_m S_m U_{mm}(r) + \rho_w S_w U_{wm}(r)\right] \\
&= 2\pi h\rho_m\varepsilon_{mm}\sigma_{mm}^2\left\{\frac{1}{5}\left(\frac{\sigma_{mm}}{r_c}\right)^{10} - \frac{1}{2}\left(\frac{\sigma_{mm}}{r_c}\right)^{4}\right\} \\
&\quad -2\pi h\rho_w\varepsilon_{wm}\sigma_{wm}^2\left\{\frac{1}{5}\left(\frac{\sigma_{wm}}{r_c}\right)^{10} - \frac{1}{2}\left(\frac{\sigma_{wm}}{r_c}\right)^{4}\right\} \\
&\quad +\frac{8}{3}\pi\rho_w\varepsilon_{wm}\sigma_{wm}^3\left\{\frac{1}{3}\left(\frac{\sigma_{wm}}{r_c}\right)^{9} - \left(\frac{\sigma_{wm}}{r_c}\right)^{3}\right\} \qquad (3.27)
\end{aligned}
$$

After performing the integral, Equation 3.27 is obtained. The detailed step-by-step derivation of the modified tail correction is included in Appendix A. It is important to note that, since this formula inherits from the spherical segment's surface area formula, the prerequisite to successfully using this formula is that the cutoff distance must be equal to or larger than the separation of the two solid walls.

3.3.2.2 Effectiveness Test

Now it is necessary to measure the effectiveness of the modified tail correction in potential calculations. This new modified tail correction is tested in potential calculations for an ideal nanoconfined system, which consists of two perfect FCC walls and a perfect FCC nanoconfined phase. The following test calculations were performed at $\sigma_m = \sigma_w = 1.0, \rho_w^* = \rho_m^* = 1.0, \varepsilon_{wm}^* = 4.0$ and $T^* = 0.75$.

$$\begin{aligned} Utail_{mm} &= \frac{8}{3}\pi\rho_w\varepsilon_{mm}\sigma_{mm}^3\left\{\frac{1}{3}\left(\frac{\sigma_{mm}}{r_c}\right)^9 - \left(\frac{\sigma_{mm}}{r_c}\right)^3\right\} \\ Utail_{wm} &= \frac{8}{3}\pi\rho_w\varepsilon_{wm}\sigma_{wm}^3\left\{\frac{1}{3}\left(\frac{\sigma_{wm}}{r_c}\right)^9 - \left(\frac{\sigma_{wm}}{r_c}\right)^3\right\} \end{aligned}$$

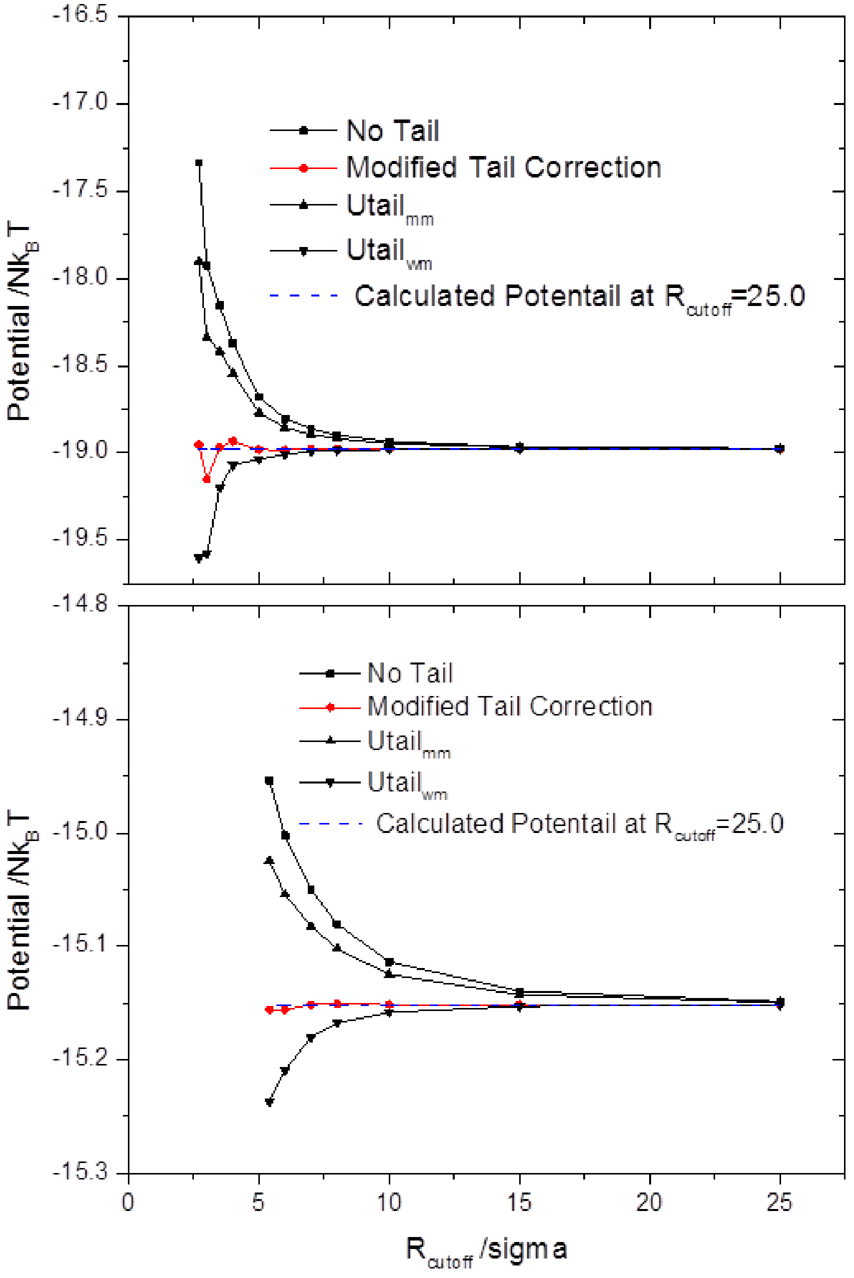

Figure 3.6. Comparison of scenarios with no tail correction, modified tail correction, and two general tail corrections in potential calculations. (top) The wall-wall separation is 3 ideal layers, with minimum cutoff radius $r_c = 2.7\sigma$. (bottom) The separation is 6 ideal layers, with minimum cutoff radius $r_c = 5.4\sigma$.

As shown in Figure 3.6, neither $Utail_{mm}$, $Utail_{wm}$, nor the no tail correction could model the heterogeneous nature of a nanoconfined system. The large difference between values provided by these strategies and the potential calculated at an extremely large cutoff radius suggests a better tail correction is necessary. Fortunately, the modified tail correction proposed in this dissertation research demonstrates dramatic advantages over these aforementioned strategies. The minor difference between the modified tail correction potential value and the potential calculated at extremely large cutoff radii indicates that the modified tail correction could better describe the heterogeneous nature of nanoconfined systems with sufficient accuracy. The difference between generally used standard tail corrections and the modified tail correction is on the order of 0.1 Nk_BT. This strongly suggests that simply using the traditional tail correction in a nanoconfined system will bring a dramatic systematic error. However, this can be avoided by the modified tail correction.

3.3.3 Adapted Algorithm Validation

To examine the adapted algorithm, an absolute FE comparison (shown in figure 3.7) has been designed and performed. In this model system, both the walls and the nanoconfined phase are structurally identical with its corresponding bulk. All their interaction parameters in the nanoconfined and bulk systems are the same, with the only difference being the mobile particles in the confined phase. They will feel the interaction of static rather than mobile particles in the nanoconfined system.

In the test FE determination, the adapted algorithm has been employed and given a FE value $A = -5.465Nk_BT$ for the confined phase in the model system. This is in close agreement with the FE of the bulk system as determined by using the basic algorithm ($A = -5.482Nk_BT$) and the value published in literature ($A = -5.494Nk_BT$)[123] for bulk crystals under the same condition (i.e., $T = 0.75$ and $\rho = 1.0$). Hence, this consistency has validated the modified algorithm that will be used in the following research.

Meanwhile, this consistency also strongly suggests that the treatment of wall particles as stationary has a negligible effect on the FE of the nanoconfined phase. In particular, considering that the wall particles themselves will be much more tightly bound to their lattice positions under strong wall-fluid interaction scenarios, the discrepancy owing to the static assumption is even less obvious.

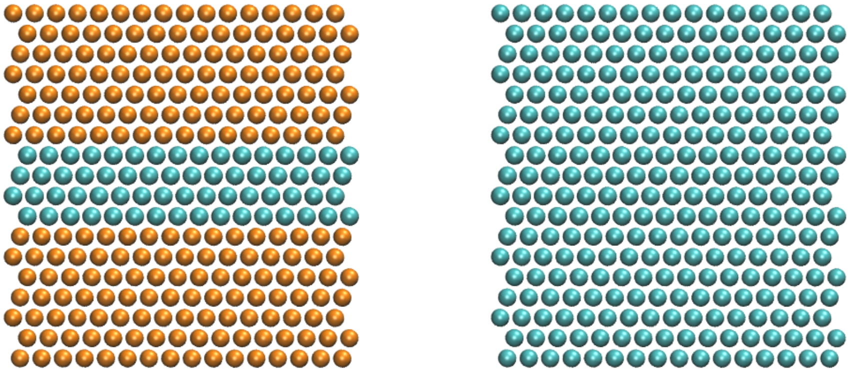

Figure 3.7. Snapshots of the nanoconfined system and the bulk FCC solid used in the modified algorithm validation. (left) The nanconfined system consists of an ideal FCC(111) structure confined between FCC(111) walls. (right) The bulk solid consists of FCC. The color coding of particles is: blue - mobile particles, orange - static solid wall particles.

.

3.3.4 Definition of Separation

As a crucial parameter in nanoconfined fluid behavior, the definition of separation (h) in a nanoconfined system is somewhat artificial in simulations. Since two kinds of surfaces with different orientations have been employed in this work, a brief introduction of separation definition is included here. Equation 3.28 is the separation definition in a FCC(111) solid surface nanoconfined system and Equation 3.29 is the separation definition in a FCC(110) solid surface nanoconfined system.

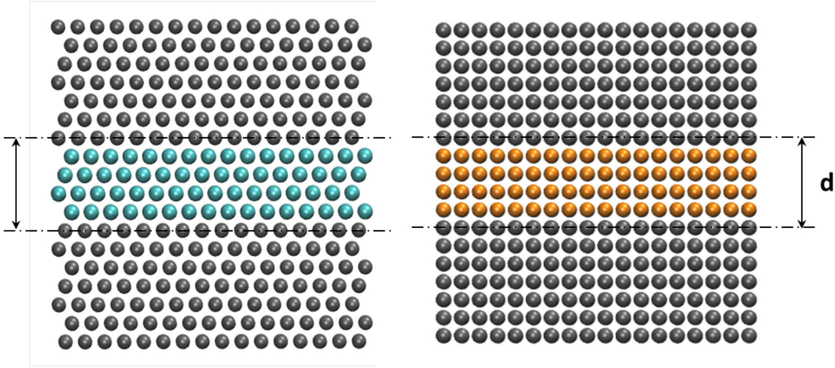

Figure 3.8. Definitions of separation in nanoconfined system employed in this dissertation research. (left) The solid wall consists of FCC(111) in nanoconfined system. (right) The solid wall has FCC(110) surface.

$$h = d1 - 2^{1/6}\left(6/9\right)^{1/2}\sigma_w\rho^{-1/3} \tag{3.28}$$

$$h = d2 - 0.5\left(2\right)^{1/3}\sigma_w\rho^{-1/3} \tag{3.29}$$

where h is the separation, σ_w is the inter-atomic distance at which the potential energy between two wall atoms is equal to zero, ρ is the reduced density of solid wall, and $d1$ and $d2$ denote the closest distance between the atom centers in two solid wall in a FCC(111) surface nanconfined system and a FCC(110) surface nanoconfined system respectively (shown in Figure 3.8). Generally, the sizes of wall particles and fluid particles are identical and ρ is set to unity in this dissertation research.

3.4 GPU accelerated calculation

3.4.1 Performance Gains via GPU Computing

As a specialized category among processors, the graphics processing unit (GPU) was originally created for 3D game rendering on a computer monitor. However, the large improvement in the capability and programmability of GPU over the last decade has swiftly extended its applications beyond its original arena[139]. To date, it has gained broad applications in computational acceleration in new areas, such as large-scale scientific computation, financial statistics, natural resource exploration, and weather forecasts. The usage of GPUs in general-purpose computation also exert a large impact on the development of supercomputers. Among the fastest supercomputers in the world[140], there are many machines installing GPUs to achieve augmented computing power while obtaining better energy efficiency per flop.

As compared to the central processing unit (CPU) in design, a GPU devotes a much higher ratio of transistors to computing rather than data cache. Thus, the GPU has greater computational resources compared with the general CPU. In addition to that, the intrinsic parallel architecture brings huge performance gains especially in algorithms designed to harness this parallelism. A template performance comparison of CPU and GPU in MD simulations has been conducted, using CPU-based LAMMPS and GPU-Based HOOMD. As shown in Figure 3.8, the simulation running on a GPU is at least one order of magnitude faster than on a CPU on the same motherboard. Considering the computationally intensive nature of FE calculation, GPU-accelerated simulation is used to facilitate the FE determination and promote the research based on FE values.

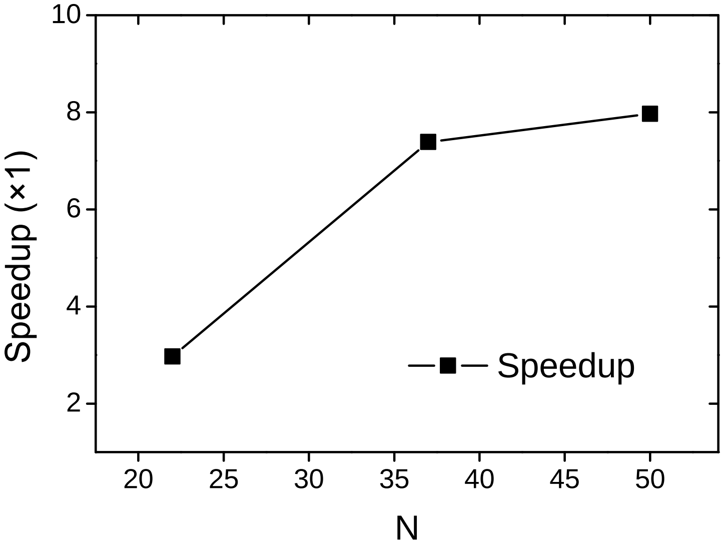

Figure 3.9. Performance comparison of CPU and GPU in MD simulation at various system size. CPU: Intel E5-2667 ×2[141] GPU: Tesla K40[142].

3.4.2 Thermostat in MD

As for open-source GPU-accelerated molecular dynamics packages, the most popular and efficient one is HOOMD (highly optimized object-oriented many-particle dynamics)[143]. HOOMD was developed from the ground up for GPUs, with a particular emphasis on coarse-grained models used herein, and thus is more efficient than LAMMPS. However, special attention should be paid to its implementations in canonical simulations of systems involving bonds, such as an Einstein solid with a harmonic bond described in this research.

In molecular dynamics simulations, the most commonly used temperature controller is the Nosé-Hoover thermostat named after its creators Nosé[144] and Hoover[145]. HOOMD employs their original algorithm in the simulation. While the Nosé-Hoover thermostat works extremely well for ergodic systems (i.e., the trajectory average can be taken into the phase space average), it probably fails in simulations for systems that are not so ergodic, for instance, small or stiff systems. An Einstein solid with harmonic bonds is less ergodic.

As shown in Figure 3.10, the temperature of a system simulated by HOOMD does not converge after a sufficiently long run time. Hence, that limits the usage of HOOMD in some circumstances in FE calculation. Modified dynamics using a chain of variables (Nosé-Hoover chain), that is, chains of thermostats that augment temperature control/stability, rather than the single thermostat variable in the original Nosé-Hoover dynamics, was introduced[146] and is an option for taking full advantages of the GPU in FE calculations in the future. In the following dissertation research, the usage of GPU's massive parallel computing power is limited to conducting non-bonded molecular simulations.

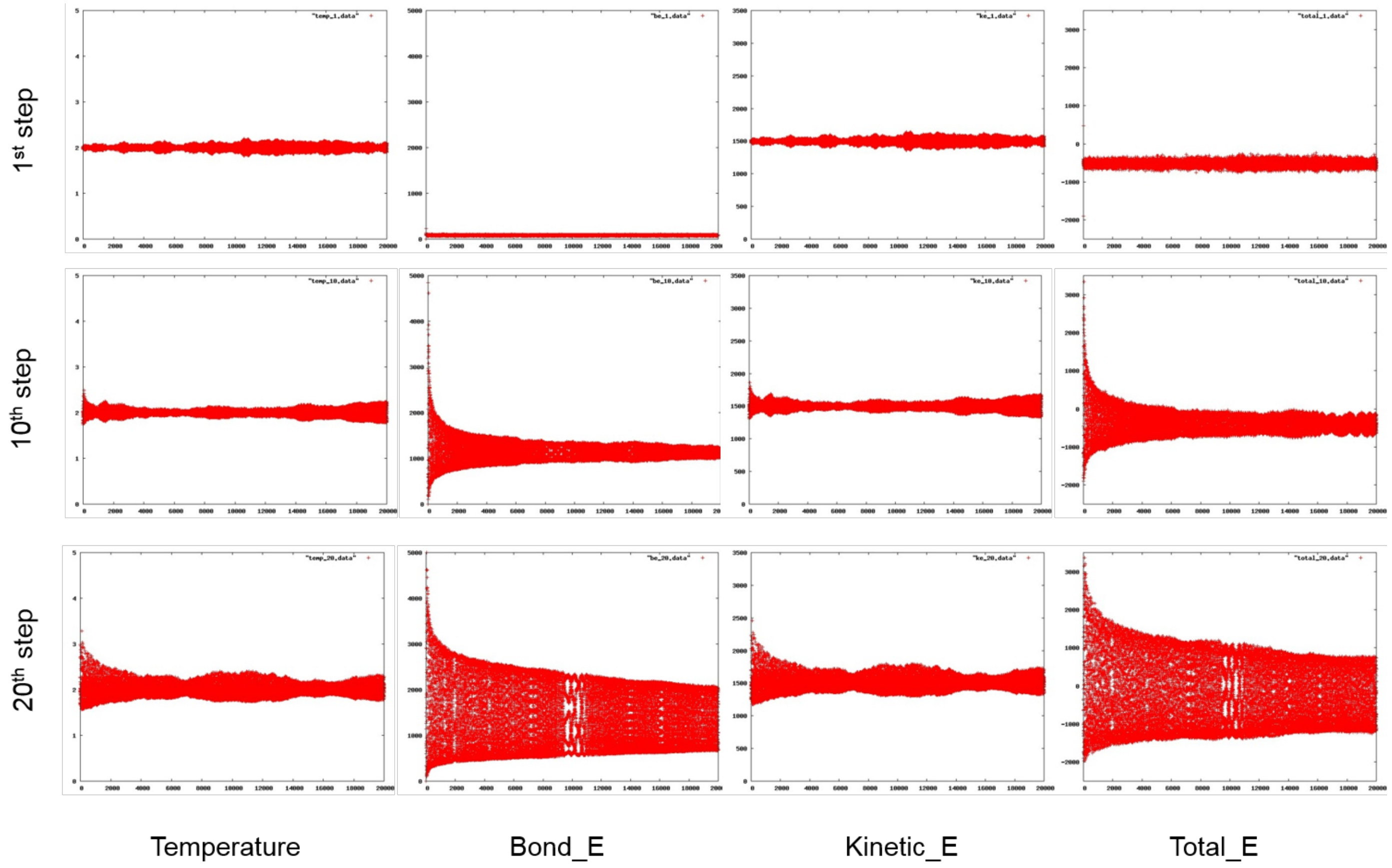

Figure 3.10. Convergence of temperature, bond energy, kinetic energy, and total energy with running time in the simulation of Einstein solid using HOOMD[143]. There are three systems with different bond strengths being tested. 1^{rd}, 10^{th}, and 20^{th} denote systems with weak bond, medium bond, and strong bond, respectively.

.

CHAPTER IV

BULK CRYSTAL SOLIDS

4.1 Role of Simulation Box Shape

According to previous studies on hard sphere systems[121], the simulation box shape plays a role in the accuracy of calculated absolute FE when using the Einstein crystal method. Briefly, the accuracy is determined by the largest cubic in the simulation box. Considering that the nanoconfined phase investigated in this dissertation research is inside a slit and is not cubic in shape, it is necessary to determine the role of box shape in absolute FE calculation of this system.

As shown in Figure 4.1, we measured the influence of box shape by comparing the calculated FEs of three different simulation box shapes. The calculated FEs for Lennard-Jones systems demonstrate dependence on the system's size (i.e., the number of particles), and not on the largest cubic in the simulation box. According to Figure 4.1, the box shape has an impact on the accuracy of calculated FEs, but it is minor compared to the system size. The influence of the simulation box shape can be minimized by using a larger system size or employing a good finite-size correction.

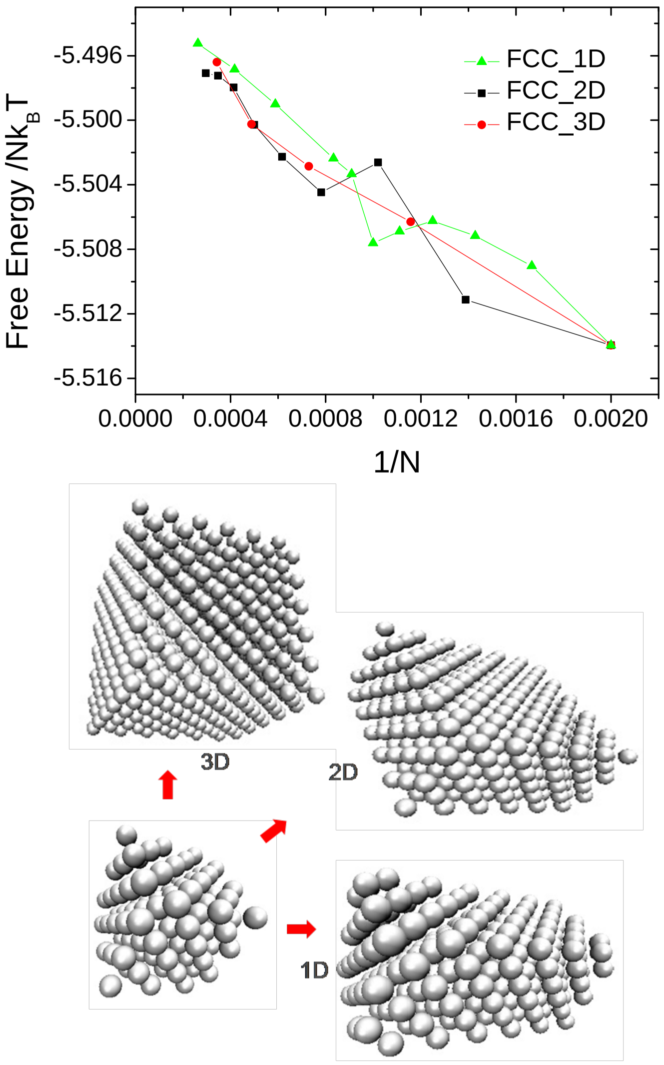

Figure 4.1. The effect of simulation box shape on calculated FEs for LJ crystals. A comparison (top) of the dependence of calculated FEs on box shape and a schematic diagram (bottom) showing what types of simulation box shapes are utilized.

.

4.2 Finite System Size Dependence and Correction

It is already known that a finite system size and a finite cutoff radius are the two major sources of systematic error in absolute FE calculations[106,119,130,133]. As such, to pave the way for more precise implementations of FE later on, their roles in FE determinations have been detailed and quantified. Moreover, reasonable compensation strategies have been explored to correct the systematic errors brought by them.

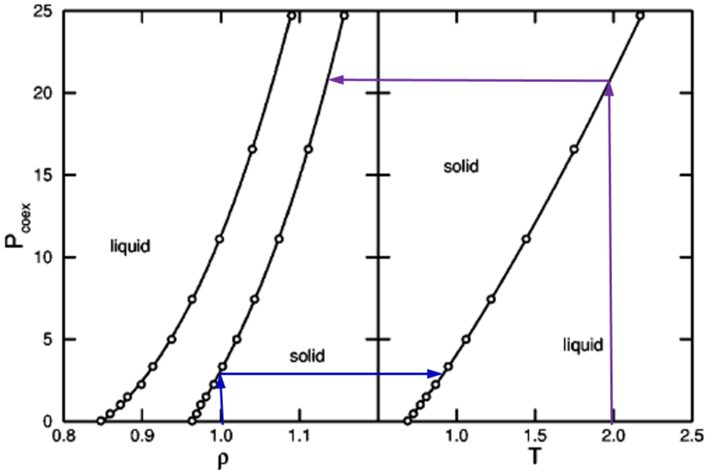

Figure 4.2. Phase diagram of Lennard-Jones system (taken from Martin A. van der Hoef's paper[147]). Blue line denotes Lennard-Jones system at $T^{\star} = 0.75$ and $\rho^{\star} = 1.00$. Purple line denotes Lennard-Jones system at $T^{\star} = 2.00$ and $\rho^{\star} = 1.28$.

To quantify the finite-size effect, we have conducted absolute FE calculations for three basic crystal types, face centered crystal (FCC), hexagonal closed packed crystal (HCP), and body centered crystal (BCC) at $T^{\star} = 0.75$ and $\rho^{\star} = 1.00$, using a series of simulation system sizes from 256 to 6912 (Figure 4.2). As shown in Figure 4.3, all free energy calculations demonstrate strong finite-size dependence, regardless of their crystal types. Hence, a universal finite size correction is necessary to correct the systematic error that stems from the usage of finite system size in calculation.

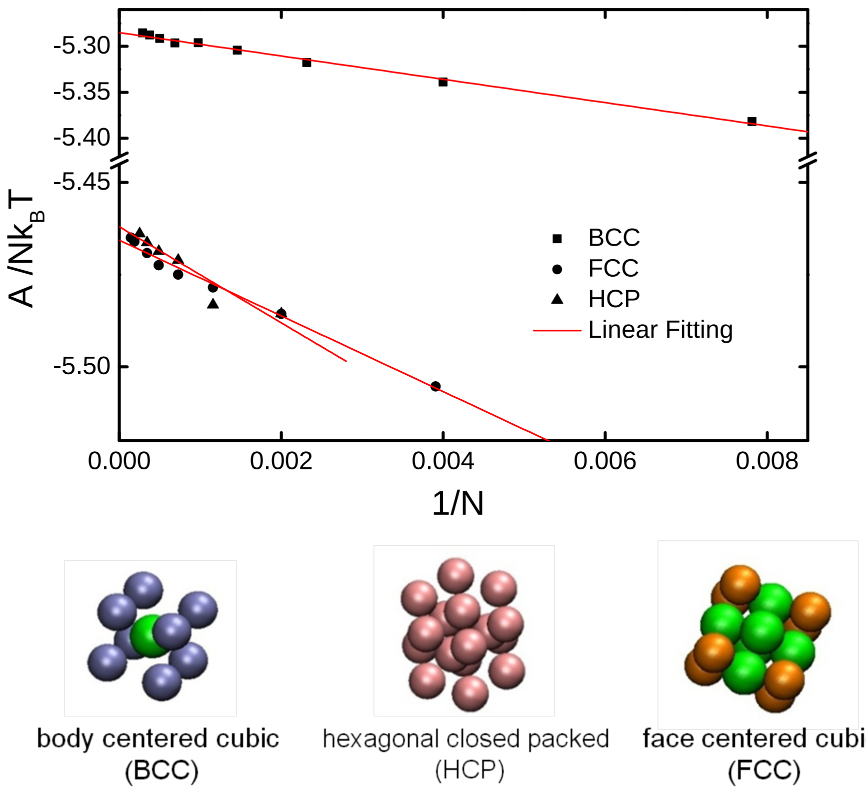

body centered cubic (BCC)
hexagonal closed packed (HCP)
face centered cubic (FCC)

Figure 4.3. System size dependence of calculated FEs for LJ crystals, at $T^\star = 0.75$, $\rho^\star = 1.00$. FEs of face centered cubic (FCC) crystal, hexagonal closed packed (HCP) crystal and body centered cubic (BCC) crystal have been calculated and compared.

The effort to introduce a finite-size correction (FSC) was pioneered by Hoover and Ree[111], which was followed with studies done by other researchers who used a modified FSC. Here we tested the effectiveness of the FSC-asymptotic, a semi-empirical finite size correction proposed by Vega and Noya[130], under the same conditions that subsequent FE calculations will use. The FSC-asymptotic compensated FE is given by

$$\frac{A_{N\to\infty}}{Nk_BT} = \frac{3}{2}\ln\left(\frac{\Lambda_E}{\pi}\right) \tag{4.1}$$

$$+\frac{1}{2}\left\{\frac{\triangle A(N,\Lambda_E)}{Nk_BT}+\frac{\triangle A(N,\Lambda_E)}{Nk_BT\,(1-1/N)}\right\} \tag{4.2}$$

where $\triangle A(N,\Lambda_E)$ is the summation of ΔA_1 and ΔA_2, representing the FE difference between the Einstein crystal and the solid of interest and $A_{N\to\infty}$ is the absolute Helmholtz FE in the thermodynamic limit (i.e., calculated FE with infinite system size and cutoff radius).

As shown in Table 4.1, we performed FE calculations for three crystal types under different density and temperature conditions, with extension to a larger simulation system size, along with the implementation of MD-based sampling instead of MC in stage two. FSC-asymptotic is always able to provide reasonable compensation for a finite-size effect, which gives precise prediction of FE in the thermodynamic limit, especially as the system size is close to 2000 particles. This suggests that use of the FSC-asymptotic correction as a universal finite-size effect compensation strategy is appropriate in FE calculations.

Table 4.1. Comparison between the calculated absolute Helmholtz FE for LJ crystals and the FSC-asymptotic corrected FE, with $T^\star = 0.75$ and $\rho^\star = 1.0$. All FE values are in units of Nk_BT. FSC-asymptotic corrected FE values as N approaches 2000 are shown in bold font.

N	FCC		HCP		N	BCC	
	Calculated FE	FSC-asymptotic	Calculated FE	FSC-asymptotic		Calculated FE	FSC-asymptotic
256	-5.505	-5.466			128	-5.382	-5.311
500	-5.486	-5.464	-5.486	-5.464	250	-5.339	-5.298
864	-5.478	-5.465	-5.486	-5.469	432	-5.318	-5.293
1372	-5.475	-5.466	-5.471	-5.462	686	-5.304	-5.287
2048	-5.472	**-5.466**	-5.469	**-5.462**	1024	-5.296	-5.284
2916	-5.469	-5.464	-5.466	-5.462	1458	-5.296	-5.288
4000	-5.467	-5.463	-5.464	-5.460	**2000**	-5.292	**-5.285**
5324	-5.466	-5.463			2662	-5.288	-5.283
6912	-5.465	-5.463			3456	-5.285	-5.281
∞	-5.466	-5.466	-5.462	-5.462	∞	-5.285	-5.285

4.3 Relative Stability of LJ Crystals

According to absolute free energy calculations for different basic crystal types, the Lennard-Jones FCC solid clearly demonstrates the lowest FE (Figure 4.3) when compared with hexagonal closed packed crystal (HCP) and body centered crystal (BCC). This is similar to the FE comparison of hard sphere crystal types in the previous study, in which the hard sphere FCC solid has the lowest free energy[106].

The lowest FE also indicates that FCC is thermodynamically the most stable Lennard-Jones crystal type among these three types under the selected condition ($T^\star$ = 0.75, $\rho^\star$ = 1.00). Although FCC and HCP both belong to closed packing crystal types, the ABA layering of FCC (HCP, AB layering) gives more permutation possibilities and, hence, more microstates and lower entropy. However, the FE difference between FCC and HCP is minor (highlighed with inset in Figure 4.3) when compared to their FE gap with BCC.

4.4 Finite Cutoff Radius Effect

In addition to the effect of finite system size, the finite cutoff radius is also a major systematic error source in FE calculations, especially for solids. Solid structures microscopically exhibit intrinsic high ordering and solid crystals therefore have anisotropic properties. Due to this intrinsic ordering in solids, the generally used cutoff radius in fluid simulations is not sufficient to guarantee the accuracy of solid simulations, particularly, potential and FE calculations for solids.

As shown in Figure 4.4, the radial distribution of FCC, HCP, and BCC crystals still oscillates dramatically at relatively large radii compared to fluid, as does the potential residue. The assumption, that radial distribution function $g(r)$ is equal to unity at large values of r, for the generally used standard tail correction does not hold well when using a typical cutoff radius for fluids. Hence, we investigated the finite-cutoff radius dependence of each term in the absolute free energy calculations to find specific compensation strategies for each.

In this work we performed FE calculations for LJ crystals at a series of cutoff radii at $T^\star = 0.75$, $\rho^\star = 1.0$, and a given large system size. As shown in Figure 4.5, calculated FEs demonstrate a strong finite cutoff dependence and each term in the FE calculation has a remarkably different cutoff-radius sensitivity.

The results in Figure 4.5 clearly demonstrate that the finite cutoff effect is in large part determined by the choice of cutoff radius in ΔA_1 evaluation, rather than that of ΔA_2. According to the profiles in Figure 4.5, a cutoff radius larger than 3.0 sigma is already sufficient to provide a FE change value with necessary precision in ΔA_2 evaluation. ΔA_1, at a cutoff radius of 3.0, still shows a strong dependence on cutoff radius.

This difference suggests that in order to achieve a sufficient accuracy, a longer cutoff radius is particularly necessary in the ΔA_1 calculation. This puts additional importance on the potential calculation in FE determination. In the following FE calculations, the employed cutoff radius should be as long as possible within the practical conditions, and the choice of tail correction also needs to capture the nature of the solid system.

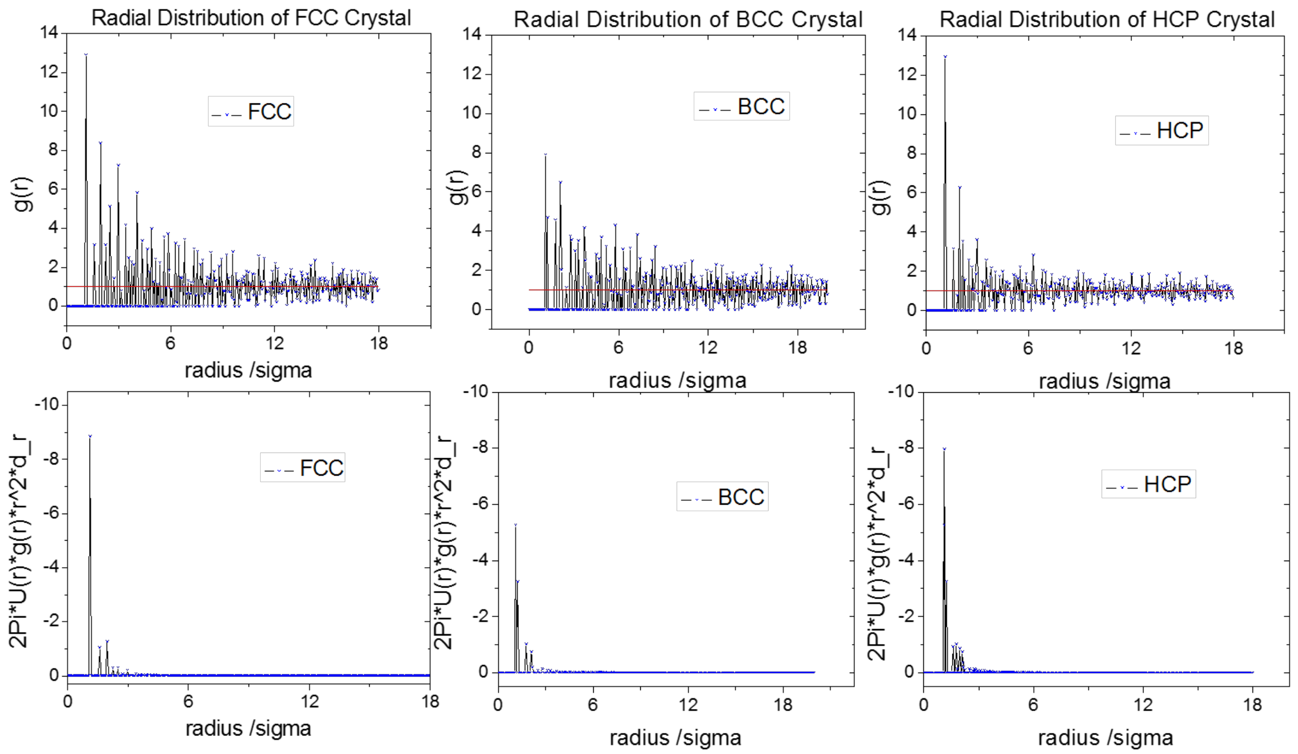

Figure 4.4. Radial distribution function and potential residue with radius of face centered cubic (FCC) crystal, hexagonal closed packed (HCP) crystal, and body centered cubic (BCC) crystal. All are at $\rho^{\star} = 1.00$.

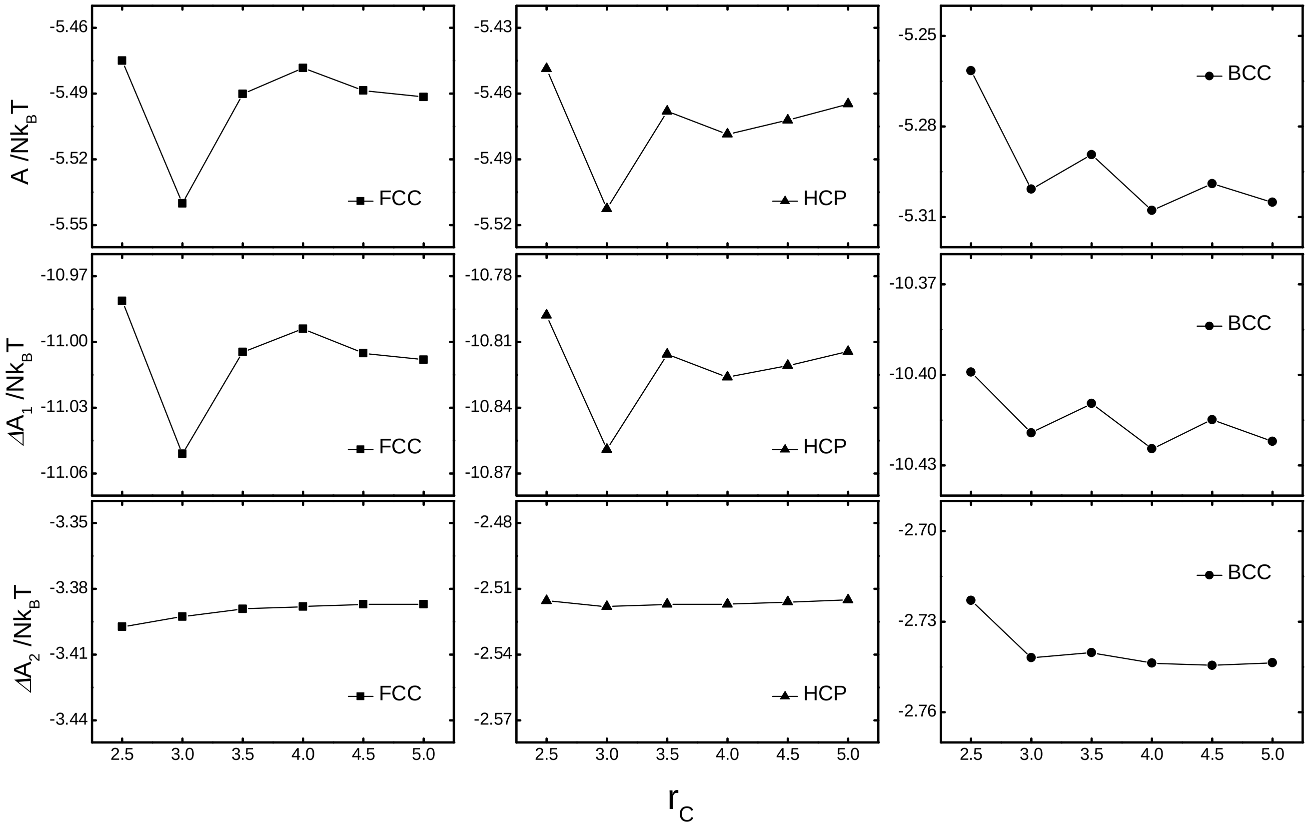

Figure 4.5. Finite cutoff radius dependence of absolute Helmholtz FE (A), state one(ΔA_1), and state two(ΔA_2). Three crystal types, FCC, HCP, and BCC are measured. r_c is cutoff radius.

CHAPTER V

IDEAL NANOCONFINED SYSTEMS

5.1 Wall-Fluid Interaction

It is known that the wall-fluid interaction and the wall-wall separation (i.e., split pore size) play crucial roles in determining nanoconfined fluid behavior. Previous simulation work predicts that as the interaction strength between walls and mobile fluid particles ($\varepsilon_{\mathrm{wm}}$) is increased to values exceeding the fluid-fluid interaction ($\varepsilon_{\mathrm{mm}}$) at sufficient confinement, the transition temperature will shift to higher temperatures than an equivalent bulk system[148,149]. Hence, this chapter begins by revisiting the impact of the wall-mobile fluid interaction strength on the thermodynamic stability and transition temperature of nanoconfined fluids. This allows for the establishment of boundaries for the specific model and parameters used in this work, as well as to further test the adapted free energy method.

We adapted absolute FE calculations for nanoconfiend ideal FCC structures at various wall-fluid interactions ($\varepsilon_{wm} = 2.0 * \varepsilon_{mm}$ and $\varepsilon_{wm} = 4.0 * \varepsilon_{mm}$) and separations. As shown in Figure 5.1, the increment of wall-fluid interaction ($\varepsilon_{wm} = 2.0 * \varepsilon_{mm}$ to $\varepsilon_{wm} = 4.0 * \varepsilon_{mm}$), draws the FE of the nanoconfined phase lower, and thus further stabilizes the nanoconfined solid. This trend holds with the two different surface orientations (FCC(100) and FCC(111)) investigated in the study.

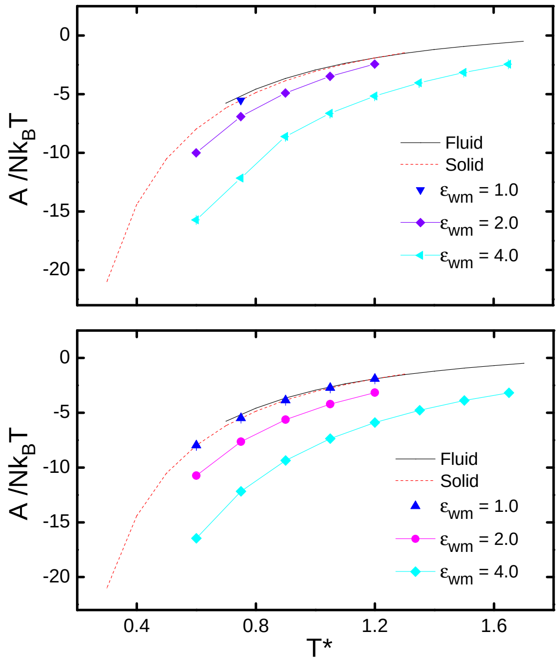

Figure 5.1. Absolute Helmholtz FE (A/Nk_BT) as a function of reduced temperature. A/Nk_BT is calculated in the scenario in which the densities of bulk fluid, bulk solid, solid wall, and nanoconfined phase are all equal to unity ($\rho^*_{bulkfluid} = \rho^*_{bulksolid} = \rho^*_{wall} = \rho^*_{confinedphase} = 1.0$). The separation for the nanoconfined phase is fixed at 4 ideal layers. The A/Nk_BT of the bulk solid and fluid are given by von der Hoef's equation[123] and Johnson's equation[122], respectively. The interaction strength between the solid wall and the nanoconfined phase is set to 1.0, 2.0, and 4.0 respectively ($\varepsilon_{wm} = \{1.0, 2.0, 4.0\}, \varepsilon_{mm} = 1.0$). **(top)** FCC(100) solid wall with nanoconfind FCC(100) crystal. **(bottom)** FCC(111) solid wall with nanoconfined FCC(111) crystal.

More importantly, along with the increment of the wall-fluid interaction, FE of the confined structure demonstrates a tendency to converge with the FE profile of the bulk fluid at higher temperatures compared to the FE profile of the corresponding bulk solid(ε_{wm}). This is in agreement with previous simulation studies[148,149], as well as Radhakrishnan and Gubbins' relative FE results[74]. By using umbrella sampling to calculate the relative FE of nanoconfined systems, Radhakrishnan and Gubbins successfully demonstrate a higher melting/freezing point with a larger wall-fluid interaction strength.

5.2 Role of Wall-Wall Separation

The next key parameter to study in nanoconfined fluid behavior is the wall-wall separation. As reported in experimental studies, first-order phase transitions of nonpolar organic fluids occurs only when the thickness of the slit pore (created by mica sheets) is smaller than seven molecular diameters[6,16,47]. Thus, this work takes a thermodynamic approach to investigate the role of wall-wall separations in nanoconfined phenomena by calculating the FE of nanoconfined idealized solid structures at various molecular diameters.

As shown in Figure 5.2, the absolute FE of the nanoconfined phase decreases with narrowing separation. Together with the results demonstrated in Figure 5.1, the absolute FE of the nanoconfined phase can be lowered either by enhancing the wall-fluid interaction and/or decreasing the nanoconfined slit pore size. In this manner, the solid structure turns out to be more thermodynamically stable and enables a much easier fluid-to-solid transition of nanoconfined fluids. This trend demonstrates good consistency with the previous simulation and relative FE calculation results[74,96,150]

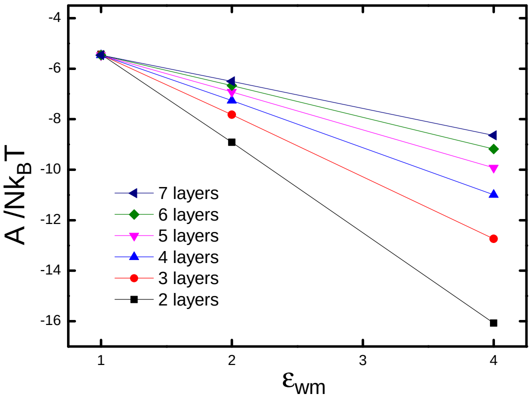

Figure 5.2. Free Energy (A/Nk_BT) of the nanoconfined ideal crystal as a function of wall-wall separation. FE calculations are conducted under separations ranging from two ideal layers to seven ideal layers. The nanoconfined solid system consists of two FCC(111) walls and a nanoconfined FCC(111) crystal.

.

5.3 Structure of Nanoconfined Phase

As indicated in the previous sections, sufficient nanoconfinement and strong wall-fluid interactions have the potential to induce a fluid-to-solid phase transition for a nonpolar fluid, given the fact that they can remarkably lower the FE of the nanoconfined phase in solid states. However, another question emerges if the solid structure forms. Specifically, whether or not the solid structure formed in the nanoconfined split pore is identical with its corresponding bulk.

To answer this question, we examined another group of FE comparisons (as shown in Figure 5.3), under the condition that the temperature is well below the bulk solid melting point ($T^* = 0.75$) and around the melting point ($T^* = 1.00$). The FE difference is measured between the perfectly packed crystal of the nanoconfined phase (its structure is identical with its bulk crystal) and the configuration with stacking faults that is taken from MD simulations.

As demonstrated in Figure 5.3, the configuration with the stacking faults at a separation of two ideal layers has a lower FE than that of the corresponding perfectly packed crystal. This suggests that the confined phase tends to form a solid structure that is different from its corresponding bulk. However, that does not mean the configuration with staking faults is always more stable. As the separation increases in the nanoconfined phase as a whole, the bulk-like perfect structure is preferred. The increase of temperature, from $T^* = 0.75$ to $T^* = 1.00$, also demonstrates a similar trend (Figure 5.3). The bulk-like perfect structure is thermodynamically more stable at a higher ambient temperature. This indicates that the confined phase as a whole, tends to form a bulk-like structure as the separation widens and the temperature increases, and vice versa.

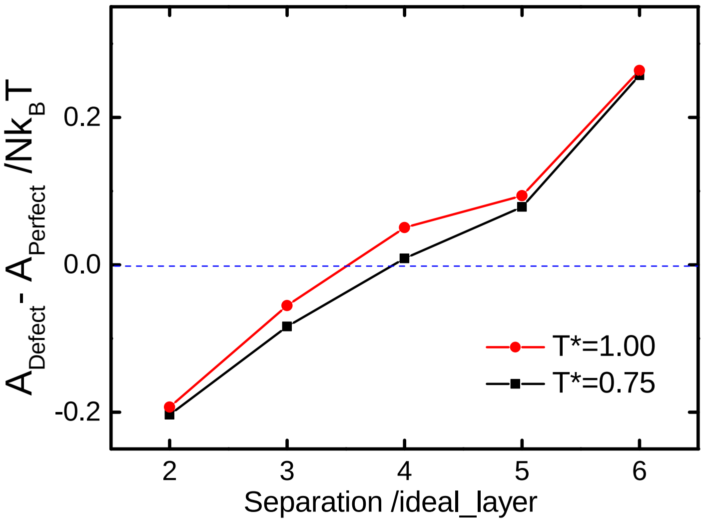

Figure 5.3. Absolute Helmholtz FE difference between perfectly stacked crystal and corresponding structure that has stacking faults. The wall-fluid interaction strength is 4.0 times of that of fluid-fluid interaction ($\varepsilon_{\mathrm{wm}} = 4.0\varepsilon_{\mathrm{mm}}$) and sigma for the solid wall and the nanoconfined fluid/phase are the same ($\sigma_{\mathrm{ww}} = \sigma_{\mathrm{mm}}$). The density is 1.0 both for the wall and nanoconfined phases ($\rho_w^* = \rho_m^* = 1.0$).

5.4 Fluid-Wall Particle Size Ratio

In previous sections, for FE calculation and comparison simplicity, the nanoconfined systems studied were all commensurate systems (i.e., the fluid particle size is identical with the wall spacing). Unfortunately, such scenarios are rare in real experiments. Additionally, simple organic fluids nanoconfined by solid walls show similar phase behavior regardless of their own molecular size[16,47]. Because of this, this research thus examines FE determinations at various fluid/wall particle size ratios to reveal its role in nanoconfined fluid behavior. Moreover, various fluid-wall size ratios can also be interpreted as having different surface roughness, meaning this can be viewed as the impact of wall surface roughness on the nanoconfined phase thermodynamic stability.

As Figure 5.4 shows, the FE of the confined phase decreases with the increment of the fluid-wall size ratio. Both potential energy and entropy contribute to the change of the absolute Helmholtz FE while the potential energy governs the change. The entropy

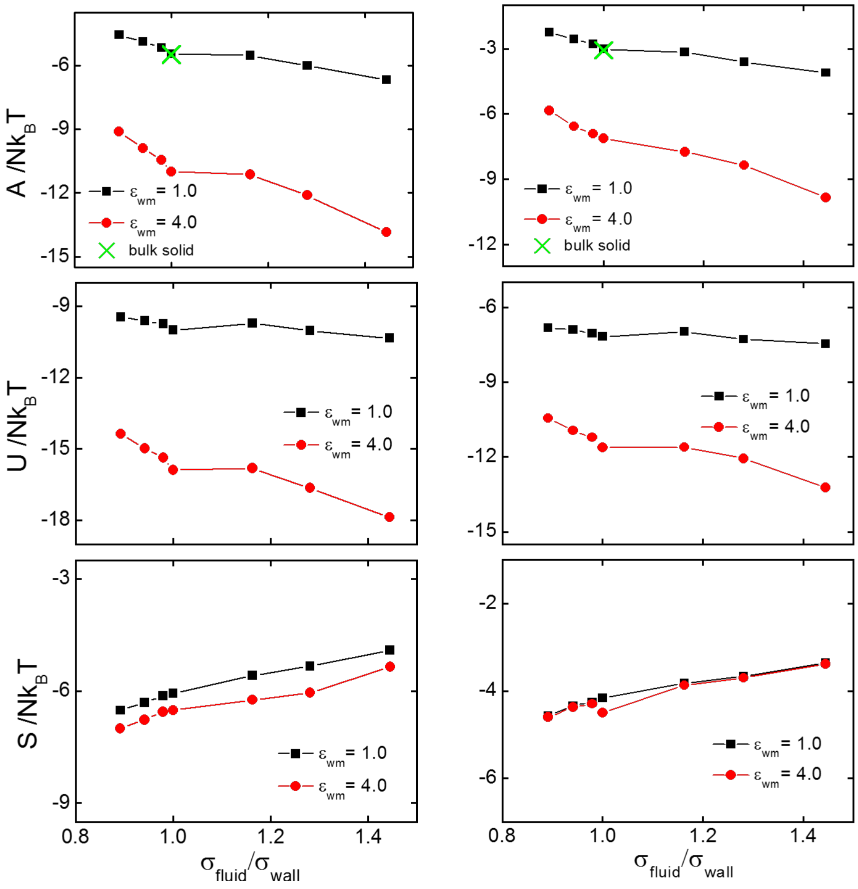

Figure 5.4. FE, potential energy, and entropy varies with fluid-wall particle size ratio, at $\rho^*_{mobile} = \rho^*_{wall} = 1.0$. **Left** column $T^* = 0.75$; **Right** column $T^* = 1.00$. The separation is scaled with fluid particle size and fixed at four ideal layers.

.

of the nanoconfined face increases steadily with fluid particle size, both at $T^* = 0.75$ and $T^* = 1.00$. This suggests that with a larger organic fluid particle, or smaller wall spacing and surface roughness, the nanoconfined phase has a lower FE and a higher thermodynamic stability. Moreover, Figure 5.4 also indicates that this trend is actually dominated by the wall-fluid potential.

$$\begin{aligned} \sigma_{wm} &= \left(\sigma_{ww} + \sigma_{mm}\right)/2 \\ \varepsilon_{wm} &= \left(\varepsilon_{ww} * \varepsilon_{mm}\right)^{1/2} \end{aligned} \tag{5.1}$$

When conducting studies on fluid-wall particle size ratios, it is important to note that the FE calculation for incommensurate systems is somewhat artificial. As noted above, the wall-fluid potential energy plays a dramatic role in the thermodynamic stability of the nanoconfined phase. Hence, the definitions of fluid-wall interaction range may have a dramatic impact on the calculated FE. To clarify this, aside from the standard Berthelot-Lorentz combining rule (Equation 5.1) used previously, two other definitions of wall-fluid interaction range (Equation 5.2 and Equation 5.3) are used to determine the free energy of the nanoconfined phase and investigate the role of fluid-wall size ratio. In order to make the comparison more straightforward, the separations in all of these FE calculations are scaled with fluid particle size and fixed at four ideal layers.

$$\sigma_{wm} = (\sigma_{ww} * \sigma_{mm})^{1/2} \tag{5.2}$$

$$\sigma_{wm} = 1 \tag{5.3}$$

As shown in Figure 5.5, using the geometric average of the full-full interaction and the wall-wall interaction to define the wall-fluid interaction range (Equation 5.2) gives a similar profile as the standard Berthelot-Lorentz combining rule (Equation 5.1). Nonetheless, the FE change of the system with a fixed wall-fluid interaction range is dramatically different. While the former two definitions remain similar and the absolute FE of the nanoconfined system gradually decreases with the increment of the fluid-wall particle size ratio, the FE profile demonstrates a local minimum at $\sigma_{fluid}/\sigma_{wall} = 1.0$ in the latter case.

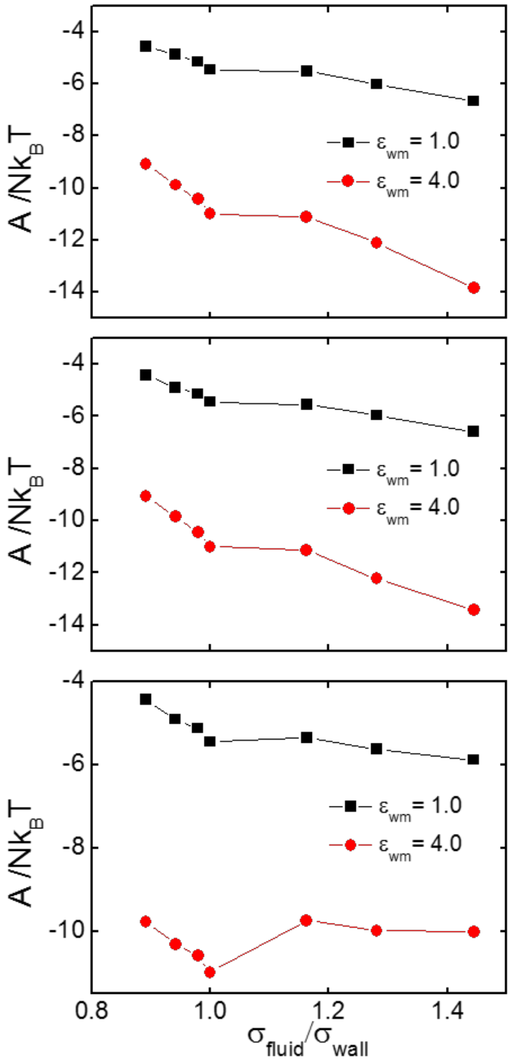

Figure 5.5. FE as a function of the fluid-wall particle size ratio at different definitions of wall-fluid interaction range. **(Upper)** Berthelot-Lorentz combining rule; **(Central)** geometric average; **(Bottom)** fixed wall-fluid interaction range at $\sigma_{wm} = 1$. Densities and temperature of the system are set to $\rho^*_{mobile} = \rho^*_{wall} = 1.0$, and $T^* = 0.75$. The separation is scaled with fluid particle size and fixed at four ideal layers.

CHAPTER VI

NONIDEAL NANOCONFINED SYSTEMS

6.1 GCMD

6.1.1 Molecular Dynamics Simulations

In experimental scenarios, the nanoconfined region is typically immersed in fluid[151]. Early simulations conducted by Gao et al.[78] have investigated properties of nanoconfined fluids in grand canonical molecular dynamics (GCMD) simulations. This dissertation research details both simulation analysis and FE measurements to further understand the nanoconfined phase that is immersed in bulk fluid.

To this end, we conducted grand canonical molecular dynamics (GCMD) simulations as pioneered by Gao and Landman[152]. Our GCMD simulations consist of an FCC slit nanopore embedded within a large, rectilinear bulk system, allowing for the free exchange of particles between the pore and the bulk environment (see Figure 6.1). Here, the system is designed such that when the density in the pore = 1.0, the bulk has a density of 0.85; because of the large size of the bulk, the bulk density is essentially unaffected by small changes in the pore density. As a result, particles in the bulk are essentially unaffected by changes within the pore. As shown in Figure 6.1, we performed simulations with a constant number of particles N, volume V, and temperature T (i.e., NVT); while GCMD simulations are often performed at constant pressure P (i.e., NPT), the large size of the bulk fluid makes the use of NPT unnecessary, as negligible changes in system pressure were seen as a function of time.

In this work, two different sets of simulations are performed. The first set of simulations consists of GCMD simulations of 86000 total particles and are used to investigate the order-disorder transition (ODT) and as input to the FE calculations (shown in Figure 6.1). These are performed with both the HOOMD-Blue[143,153] and LAMMPS[134] simulation packages using the Nosé-Hoover thermostat with timestep = 0.001 in LJ units; HOOMD-Blue[143,153] is used for calculations performed on clusters equipped with graphical processing units (GPU) whereas LAMMPS was used for parallel simulations on traditional distributed CPU-systems. Both packages produced essentially identical results. Simulations use the XPLOR style shifting which leaves the well depth unchanged as a result of potential truncation and shifting. The cutoff of the interaction between mobile particles is set to 3σ (as suggested in Section 4.4), where XPLOR shifting starts at 2.75σ. The wall-mobile particle interaction cutoff is set to 5.0σ, with XPLOR shifting starting at 4.75σ. Since the wall-mobile particle interaction energy will, in general, exceed the interaction between mobile particles, a larger cutoff is required to minimize artifacts associated with truncation. This longer cutoff and XPLOR shifting is also used to ensure better continuity with free energy calculations.

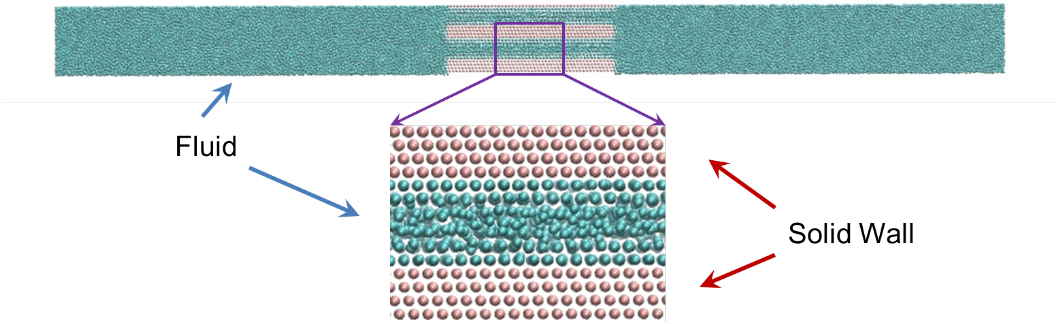

Figure 6.1. Snapshot of a nanoconfined system in a typical GCMD simulation. In this case, two pores constructed of stationary particles are embedded within a large bulk fluid, with periodic boundary conditions in all dimensions. The simulation is accelerated by using a GPU.

The second set of simulations consists of large-scale GCMD simulations with 960,000 and 6,220,000 total particles used to investigate the effects of surface contact area on ordering (results and analysis will be seen in Section 7.3). These simulations are carried out using a hybrid GPU-CPU version of LAMMPS[134], capable of efficiently scaling to millions of particles. These simulations also use the Nosé-Hoover thermostat with timestep = 0.005 and XPLOR shifting starting at 4.75σ.

6.1.2 Order-disorder Transition Temperature Analysis

To investigate the order-disorder transition (ODT), the GCMD simulations were performed by starting from a high temperature disordered state at $T^{\star} = 4.0$, then cooling by increments of $\Delta T^{\star} = 0.1$ until a low temperature solid is achieved. The ODT is estimated via visual inspection and examination of a layer-by-layer global 2D hexagonal order parameter (OP) of particles within the pore, constructed by taking the Fourier transform with frequency $\ell = 6$ of the super-position of the in-plane first neighbor shell surrounding atoms within a given layer[154,155]; a perfectly ordered layer will result in an OP value of unity. For reference, $T_{\mathrm{ODT}}^{\mathrm{bulk}} \sim 0.9$ for a bulk system at $\rho^{\star} = 1$ (note, $\rho^{\star} = 1$ is the density of an ideal minimal potential energy FCC crystal). Table 6.1 summarizes the ODT for ideal pore separations (i.e., integer multiples of the FCC layer spacing, $2^{(1/6)}\sqrt{(6/9)}\sigma$), for various $\varepsilon_{\mathrm{wm}}$ values. Here we see that as $\varepsilon_{\mathrm{wm}}$ is increased, so does $T_{\mathrm{ODT}}^{\mathrm{conf}}$, which is in agreement with previous work[148,156]. The ODT is also shifted to higher temperatures as the pore separation is reduced. This is likely a consequence of the fact that larger pores have a smaller fraction of the total number of confined particles in contact with the walls. Also, we observe that even when interactions are symmetric ($\varepsilon_{\mathrm{wm}} = \varepsilon_{\mathrm{mm}} = 1$), small pores demonstrate a slight increase in $T_{\mathrm{ODT}}^{\mathrm{conf}}$ as compared to the bulk phase. We also note note that as we exceed six ideal layers, $T_{\mathrm{ODT}}^{\mathrm{conf}} \sim T_{\mathrm{ODT}}^{\mathrm{bulk}}$, within the accuracy of our ODT calculations and density variations within the pore.

Table 6.1. T_{ODT} estimated using GCMD simulations with resolution $\Delta T^{\star} = 0.1$.

# layers	separation (σ)	$T_{\mathrm{ODT}}^{\mathrm{conf}}$ ($\varepsilon_{\mathrm{wm}}$=1)	$T_{\mathrm{ODT}}^{\mathrm{conf}}$ ($\varepsilon_{\mathrm{wm}}$=2)	$T_{\mathrm{ODT}}^{\mathrm{conf}}$ ($\varepsilon_{\mathrm{wm}}$=4)
3	2.75	1.7	2.3	3.0
4	3.67	1.4	1.8	2.3
5	4.58	1.1	1.4	1.7
6	5.50	0.9	1.1	1.2
7	6.42	0.8	0.9	1.0

To unambiguously assess the trends predicted by the GCMD simulations, we have employed the modified Einstein crystal method to calculate the absolute Helmholtz FE for idealized confined FCC systems. In Figure 5.2 of Section 5.2, A/Nk_BT of ideal nanoconfined FCC structures is plotted as a function of separation, for various $\varepsilon_{\mathrm{wm}}$ values. These calculations are performed at $T^\star = 0.75$ as it is below the bulk ODT and thus all separations should exhibit a stable solid structure. Not surprisingly, A/Nk_BT is reduced as $\varepsilon_{\mathrm{wm}}$ is increased; reducing A/Nk_BT means the phase is more stable relative to the bulk, which manifests itself in $T_{\mathrm{ODT}}^{\mathrm{conf}} > T_{\mathrm{ODT}}^{\mathrm{bulk}}$. These FE measurements also observe that A/Nk_BT is lower for smaller pores than larger pores, and thus smaller pores should likewise be expected to have a higher ODT value than the bulk. These results are fully consistent with previous studies by Gubbins et al.[148], and Kaneko et al.[156]. However, FE measurements in Section 5.2 are limited to ideal nanoconfined FCC structures and are oversimplified. A more general FE description of nanoconfined phase behavior in experiments still relies on a direct FE measurement of the nanoconfined phase in GCMD.

6.2 Free Energy of Nanoconfined Phase

We next simulated a system consisting of 86000 total particles and used their configurations for FE measurements of the nanoconfined phase (Figure 6.1). The same FE determination methodology that was validated in Section 3.3 and utilized in Chapter V is used here. First, attention is focused on the $\varepsilon_{\mathrm{wm}} = 4$ system, as this strength is roughly characteristic of mica-organic molecule interactions, and at the wall-wall separation with an integer number of ideal layers.

As shown in Figure 6.2, the FE of the confined phase is much lower than that of its corresponding fluid in the bulk region. This suggests that the confined phase and the fluid in the bulk region, although they are the same species and are in contact with each other, form different phases. Since particles in the confined region certainly are in the fluid state when the wall-wall separation is sufficiently large, the formation of a different phase in GCMD indicates that there should be a phase change as the wall-wall separation decreases, i.e., the fluid in the confined region might undergo a fluid-to-solid transition, due to the larger influence of nanoconfinement and wall-fluid interaction. The most recent pressure measurement by Gubbins et al.[157] demonstrates a similar trend. They found that the pressure of the nanoconfined phase is much higher than the corresponding bulk fluid.

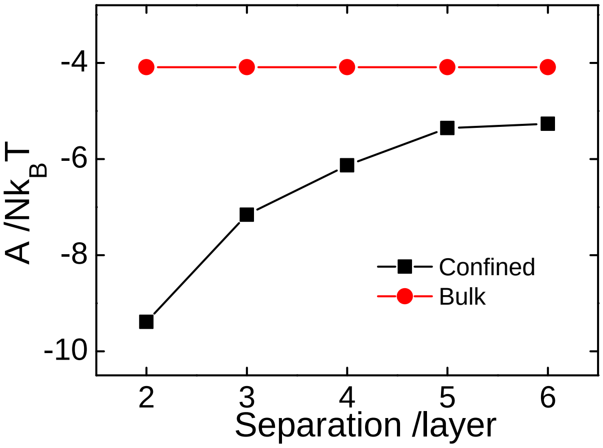

Figure 6.2. Absolute Helmholtz FE of LJ nanoconfined phase and bulk fluids as a function of wall-wall separation in GCMD simulations. The absolute FE of the nanoconfined phase is determined by employing the modified Einstein crystal method (Section 3.3), while the FE of bulk fluids is evaluated by measuring their densities in simulations first, then subsequently using the Johnson's equation[158].

Next, GCMD simulations were performed as a continuous function of separation, not just with ideal pore spacings. Each pore separation is an independent simulation employing stationary walls and thus there is no need to consider the effects of pore compression rate[159,160]. In Figure 6.3, the FE of the nanoconfined phase in the fluid state that is estimated based on the measured number density, the FE of nanoconfined phase in solid state, and the FE of bulk fluid, are plotted as a function of separation for systems at $T^\star = 1.0$. Their configurations are taken from equilibrated simulations that were generated by slowly cooling from a high temperature disordered state. At $T^\star = 1.0$, solid structures form within the nanopores over the entire range sampled in figure 6.3, while the bulk region of the GCMD simulation remains in a disordered fluid state.

Using the configurations generated via GCMD simulation as the input, and the modified

Einstein crystal method to calculate A/Nk_BT as a function of separation, we then plot the FE of corresponding states in Figure 6.3. As shown in Figure 6.3, there exist peaks and valleys in the FE curves of the nanoconfined phase in both the fluid and solid states. Like most chemical and physical transitions, the FE peaks of the nanoconfined phase in the solid state occur just prior to the transition between an integer number of layers. As the six configurational snapshots in the upper-right corner of Figure 6.3 shows, the central region of the nanoconfined phase is in a disordered state. This suggests the transition points are locally unstable states in the FE profile. Additionally, closer scrutiny reveals that a new layer is about to be generated if the separation kept growing, and that the height of this transition peak would decrease as pore separation is reduced.

On the contrary, ideal separations occur roughly midway between the peak on the left and the peak on the right, at the position where the FE of the nanoconfined phase reaches a local minimum (shown via the snapshots of nanoconfined phase configurations inserted in the FE profile 6.3). The nanoconfined phase forms a well-ordered structure at those points. Later in this research, the study on the density of the nanoconfined phase will demonstrate that these are also the points where the number densities of nanoconfined phase are most close to $\rho^\star = 1.00$ (i.e., the density of the energetic minimum FCC crystal).

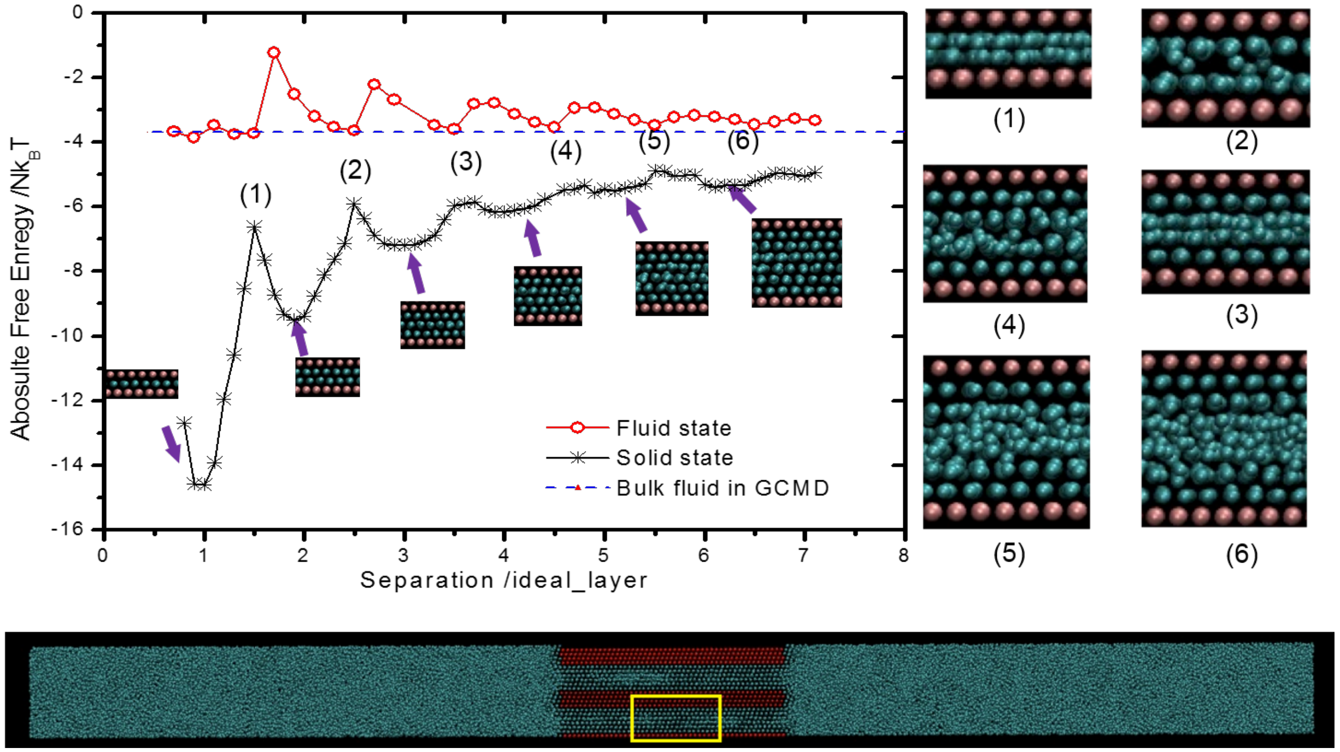

Figure 6.3. **(Upper Left)** Absolute Helmholtz FE of the nanoconfined phase in fluid and solid states, absolute Helmholtz FE of the bulk fluid, as a function of separation, and the snapshots of each configuration of the nanoconfined phase at separations that are at integer number of ideal layers. Absolute Helmholtz FE of the nanoconfined phase is determined using structures generated in GCMD simulations as the input. Absolute Helmholtz FE of the nanoconfined phase in fluid state and bulk fluid number are calculated using their measured number density in GCMD simulation and the Johnson's equation[158]. The number density of the bulk fluid is kept at $\rho^{\star} = 0.85$ **(Upper Right)** Snapshots of the nanoconfined phase at the local peak of their absolute Helmholtz FE. **(Bottom)** Snapshot of the entire system in GCMD simulation and the region that is used for sampling.

Moreover, for ideal separations, A/Nk_BT of the nanoconfined solid is significantly lowered as the separation is reduced, as was seen in Figure 5.2. The difference in the peak height *versus* valley depth of the free energy curve is most significant for small separations, whereas the differences are relatively minor for larger separations. That is, there is a smaller penalty for transitioning between integer layer numbers as the pore size is increased.

Also plotted in Figure 6.3 is the free energy of the bulk region of the GCMD simulation at $\rho^\star = 0.85$, as calculated using the Johnson's equation[158]. Over the entire range, A/Nk_BT of the nanoconfined region is lower than the bulk phase it is in contact with. As such, there is a strong thermodynamic driving force associated with forming a solid phase within the pore. For an additional comparison, the density within the pore is used as input to the Johnson's equation, i.e., we compare to the free energy of a disordered liquid at the same density as the solid within the pore. A/Nk_BT of a liquid state scales with density[158], whereas the solid phase demonstrates a more complex density behavior related to its ability to accommodate the crystal structure.

6.3 Role of Boundary Layers

As revealed in previous simulation studies on various nanoconfined systems, the boundary layer, which is the fluid layer most adjacent to the solid wall, has properties that are significantly different from other layers in the nanoconfined fluid. In the slit nanopore we are investigating, there are two boundary layers total. These two layers physically behave more like a solid rather than a fluid in most scenarios, even if the rest of the nanoconfined fluid is in a well-defined fluid state. As such, it is necessary to differentiate the boundary layers from the rest of the nanoconfined fluid, and to determine if they have different physical properties and what are their specific roles in nanoconfined-fluid phase behavior.

We begin this investigation of boundary layers by measuring their densities and the densities of the central layers as well as the entire nanoconfined phase in GCMD simulations. In Figure 6.4, the densities as a function of wall-wall separation are plotted. At the temperature $T^{\star} = 1.00$, the number of fluid particles in the boundary layers remains constant: 168 in the selected area (shown in snapshots in the upper-left of Figure 6.4), regardless of the change in wall-wall separation. However, the number of fluid particles in the central layers keeps increasing monotonically with a larger wall-wall separation. The number densities of the central layers and the entire nanoconfined phase see oscillations with the increasing wall-wall separation.

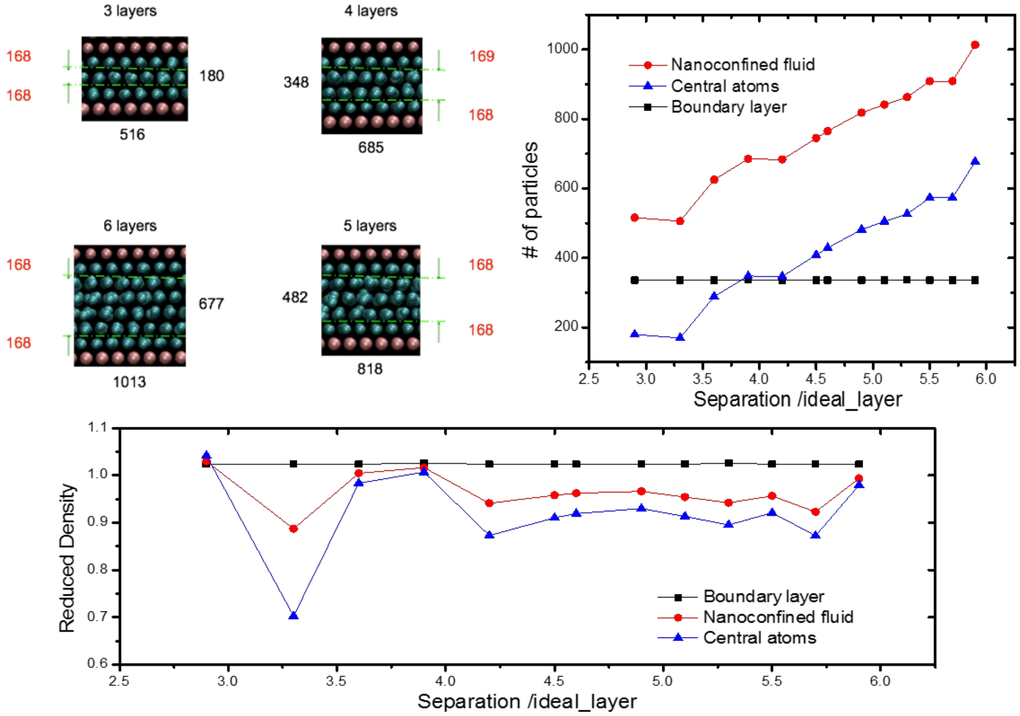

Figure 6.4. **(Upper Left)** number of particles in the selected region within the boundary layer at various separations. **(Upper Right)** Number of particles in the boundary layers, the central layers, and the entire nanoconfined region as a function of separation. **(Bottom)** Number density of the boundary layers, the central layers and the entire nanoconfined region, as a function of separation.

Nevertheless, due to the high mobility of fluid particles in central layers and the relatively weak intermolecular interaction strength between fluid particles, the prerequisite of successfully using the modified Einstein crystal method in Section 3.3 does not hold for the FE calculation of boundary layers. In other words, assuming the fluid particles in the central layers are static at all separations would render the FE determination, and all following studies based on FE, erroneous. Thus, it is not applicable to characterize the boundary layers via direct absolute FE measurements.

6.4 Free Energy of Central Region

Our results thus far have only considered comparisons between bulk phases and nanoconfined solids. The free energy of a nanoconfined disordered liquid may actually be lower than the equivalent bulk phase, based on the contribution of the wall-fluid potential energy (U) to the total free energy ($A = U - TS$). Thus, while we have clearly shown that nanoconfined solids have lower free energy than equivalent bulk phases, we have not shown via direct absolute free energy calculations that nanoconfined solids have lower free energy than nanoconfined disordered liquids. Calculating the absolute free energy of a nanoconfined fluid directly is challenging, as the simulated systems appear to be strongly driven towards forming ordered solid structures, unless an external bias is applied.

Recall that previous work[148] employed umbrella sampling to investigate the relative free energy difference between nanoconfined solids and nanoconfined disordered fluids (note, umbrella sampling includes a biasing criteria allowing sampling of regions of phase space that would otherwise be unlikely to be visited during a typical simulation).

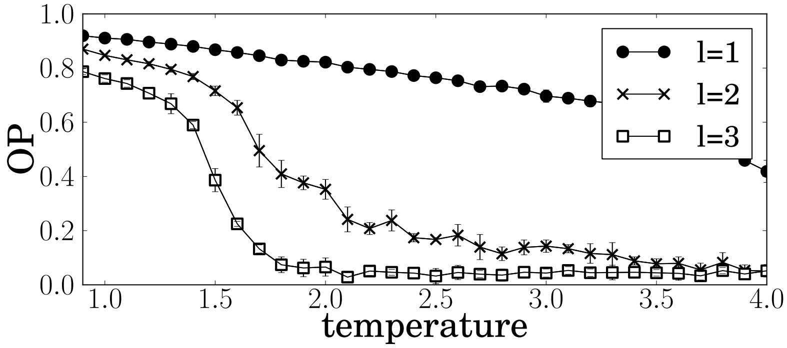

Figure 6.5. Global version of the 2d hexagonal order parameter as a function of location within a 6 layer pore for $\varepsilon_{\mathrm{wm}} = 4.00$. $l = 1$ corresponds to the layer in contact with the wall, $l = 3$ corresponds to the 3rd layer, farthest from either wall.

Rather than employing a biasing scheme, we can take advantage of the heterogeneous nature of nanoconfined systems to provide further insight into the phase transition. Specifically, it has been previously observed that particles that occupy the central most region of the nanopore strongly dictate the ODT[148]. A recent study of confined hard sphere fluids reveals that the position of particles perpendicular to the solid wall determines their diffusive dynamics, whereas particles near the wall move much more slowly even in the absence of a strong wall-fluid interaction[161]. Particles in the central region, those not in contact with the wall, experience the weakest levels of wall-mobile fluid interaction and the highest mobility, tending to lag behind regions closer to the walls in terms of structural ordering. The entire system cannot be considered a solid until this central region transitions from disordered to ordered. In Figure 6.5, we plot the 2d global hexagonal OP as a function of $T^\star$ for different spatial regions in the pore, for a system that can accommodate six ideal layers. Particles along the pore walls demonstrate a high value of the OP, even at high $T^\star$, slowly increasing as $T^\star$ is reduced. Structural ordering of the particles in the central most layer lag significantly behind the wall region and demonstrate a more rapid transition to an ordered state as $T^\star$ is reduced. The spatially intermediate second layer from the wall has characteristics more closely matching the central most layer as opposed to the layer in contact with the wall.

Following this, we make the assumption that, due to the significantly increased ordering at high $T^\star$, particles along the walls effectively act as the confining surface for the central region as it orders, allowing us to treat the layers in contact with the walls as stationary within the free energy calculation. Again, since these central layers dominate in determining when and if the system undergoes an ODT, comparing the free energy of this region to the bulk state is more appropriate as it mostly eliminates the contribution of the strong wall-mobile fluid potential energy to the total free energy.

In Figure 6.6a we plot A/Nk_BT of the central region of the nanoconfined system with $\varepsilon_{\mathrm{wm}} = 4.0$, simulated at $T^\star$=1.0; we also plot A/Nk_BT of the full nanoconfined system and A/Nk_BT of the bulk disordered fluid at the same density as the pore, calculated using the

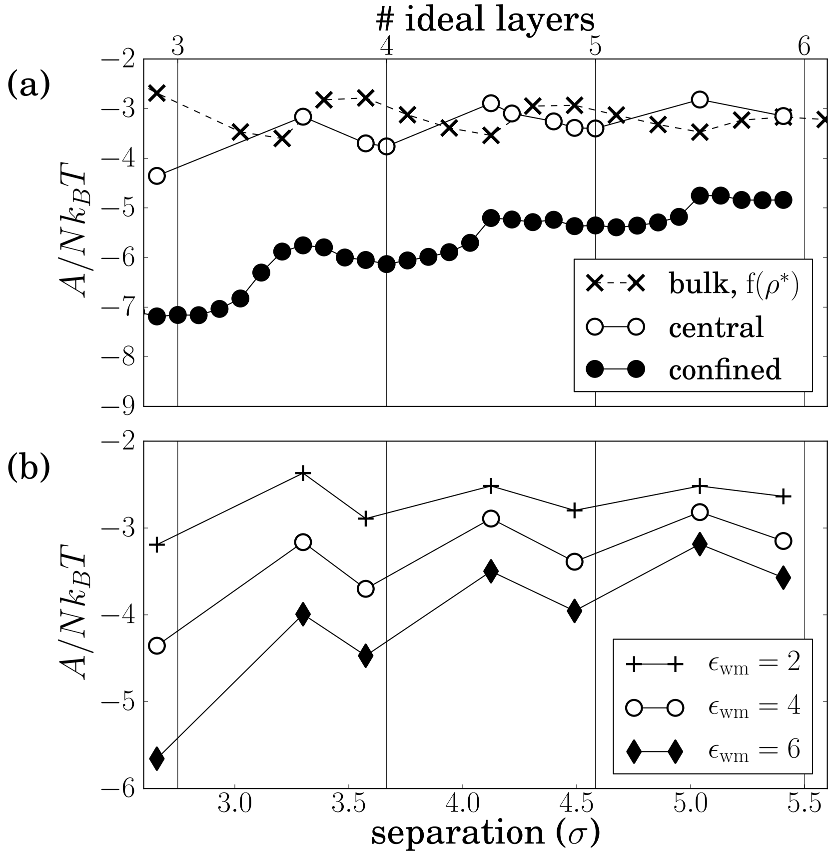

Figure 6.6. **(a)** A/Nk_BT of the central region of the pore (i.e., excluding particles along the walls) as compared to the entire confined region and the bulk value at matching density. **(b)** A/Nk_BT as a function of the central region for ε_{wm} = [2,4,6].

Johnson's equation. The free energy of the central region still demonstrates fluctuations in A/Nk_BT, where peaks occur for non-ideal separations and valleys for ideal separations. Interestingly, A/Nk_BT of the central most confined region and the equivalent density bulk fluid appear to oscillate with respect to each other; the fluid state is lower in free energy for non-ideal separations whereas the confined solid is lower for ideal separations. This agrees with calculations by Kaneko and coworkers that suggest the freezing/melting points oscillate with separation[156]. This trend persists up to approximately six ideal layers, at which point the values of A/Nk_BT converge. This strongly suggests that for larger separations there is no longer a sufficient driving force for crystallization in the central region of the pore, consistent with the previous ODT calculations in Table 6.1, where we saw that $T_{ODT}^{conf} \sim T_{ODT}^{bulk}$ for greater than six layers when $\varepsilon_{\text{wm}} = 4.0$. The fact that the solid state is not universally lower in free energy may help to explain why evidence of a fluid-solid transition is not observed in all experiments, e.g., if the system is compressed to a non-ideal spacing for the fluid.

It is important to note that while this comparison largely factors out the strong wall-fluid interaction, the free energy of the equivalent bulk state does not take into account the effects confinement on the entropy. Confinement will reduce entropy[162], resulting in an increase in total free energy, as compared to a bulk state, and the free energy should increase as pore size is reduced.

In Figure 6.6b we compare A/Nk_BT of the central region for various values of ε_{wm}. As ε_{wm} is reduced to 2, A/Nk_BT is shifted upwards, resulting in convergence with the free energy of an equivalent density bulk phase at a smaller separation ($\sim$5 layers). Similarly, increasing ε_{wm} to 6, A/Nk_BT of the central region is lowered, shifting convergence with the equivalent density bulk system to a separation exceeding six layers. This is consistent with the trends in ODT in Table 6.1, where systems with low values of ε_{wm} transitioned to bulk-like ODT values at smaller separations than systems with larger values of ε_{wm}. This trend may also help explain differences in experiments, as variations in the effective value of ε_{wm} (e.g., related to the surface ion concentration in the cleaved mica) may shift the confinement induced transition.

CHAPTER VII

EXAMINATION OF EXPERIMENTAL DIFFERENCES

7.1 Consistency

7.1.1 Experimental Studies

In the previous chapter, nanoconfined fluid systems examined using GCMD and FE measurements, supporting the assertion of the existence of a solid-fluid transition. The absolute FE investigation on a nanoconfined fluid is in agreement with Klein's observations in their SFA experiments[2–4] that the solid phase is the stable, low free energy state under sufficient confinement. However, this does not fully resolve why other experiments from Granick find evidence of glassy states[11], rather than crystals, or why AFM measurements[65,66,68] tend to agree more closely with the conclusions of Granick and coworkers. In the AFM community, researchers prefer to attribute the much lower viscosity increment observed in modfied AFM experiments (compared with the viscosity increment in Klein's SFB experiments), to the second order glass transition. While much effort has been spent to determine which group's experiments are correct, researchers in both the experimental and simulation communities want to explore whether there is a way to explain most of the experimental results by using the same description of nanoconfined nonpolar fluid behavior. In other words, they wish to develop a theory that is capable of illustrating most all of the observations in current experimental studies at the same time.

First, let us consider some of the consistent findings among experimental studies. As shown in Israelachvili's summary of experimental results[63] (in Figure 7.1, right), a common phenomenon that is shared by all experiments, even the experiments with platinum nanoparticle contamination, is the oscillation of the normal force. The normal force (or solvation force) oscillates between attraction and repulsion, and the amplitude of oscillation increases as the separation is reduced. This indicates that the separation-reducing process actually consists of a series of spontaneous and non-spontanous sub-processes. The attraction in the normal force corresponds to a spontaneous process while the repulsion corresponds to a non-spontaneous process.

We also see similar scenarios appearing in simulation studies . Briefly, most investigations into nanoconfined non-polar fluid behavior, thus far, share the same conclusion: the separation-reducing process is oscillatory in nature rather than gradually altering. That means that if a universal theory is to explain most of the investigation results to date, it must include the oscillation and give a clear description of that oscillation in the separation-reducing process.

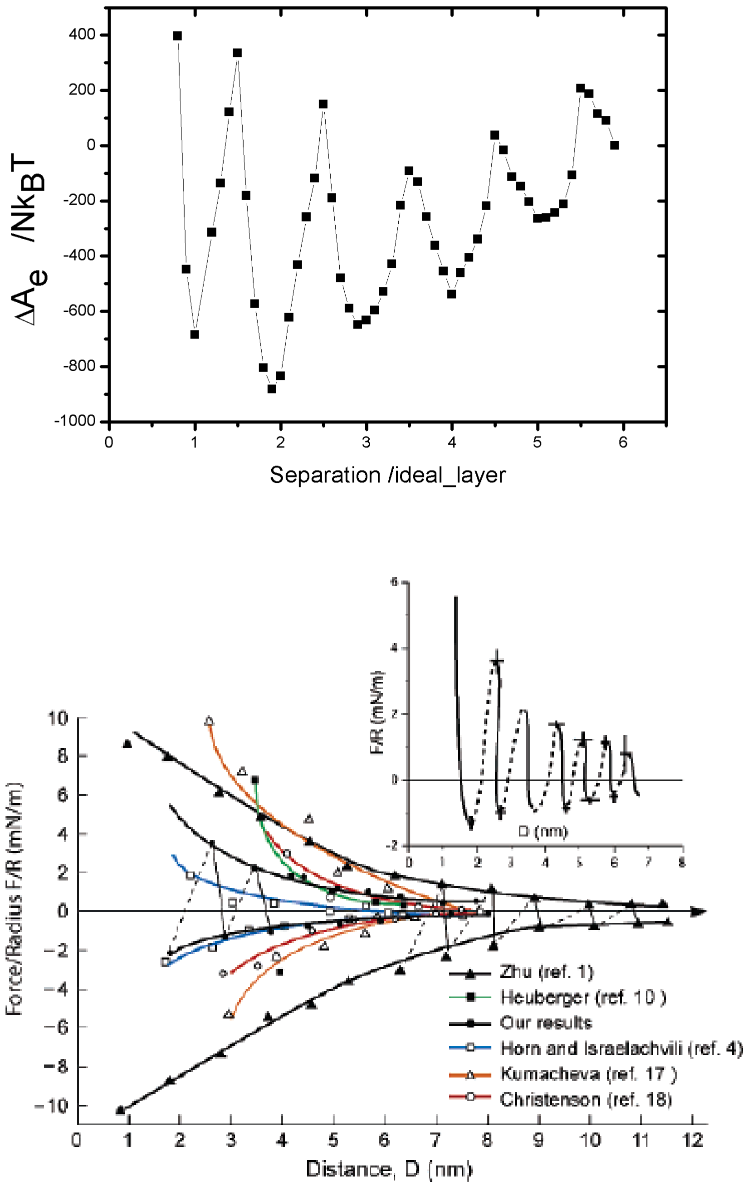

Figure 7.1. **(Left)** The free energy of the entire system as a function of separation. Green arrow: spontaneous process; Red arrow: non-spontaneous process. **(Right)** Normal force/R versus separation (taken from Israelachvili's paper[63]).

7.1.2 Cumulative FE Measurements

Due to the conclusive nature of FE measurements and the straightforwardness of absolute FE comparison, FE study on the entire system should have the ability to further prove the aforementioned consistency. However, given that different phases coexist in the system and external forces are applied, obtaining the FE of the entire system itself is not a straightforward process. Thus, we introduce several assumptions to estimate the absolute FE of the entire system (denoted in Figure 6.3 Bottom) and we employ a hybrid approach to measure the FE. That is, we divide the nanoconfined system into three parts, and evaluate their FE change individually and finally combine them together to get the FE change of the entire system from the initial separation (the separation of six ideal layers is selected here).

$$\Delta A_{EC} = \Delta A_{NC} + \Delta A_{BC} + \Delta A_{BL} \tag{7.1}$$

where ΔA_{EC} is the FE change of the entire system with reference to the system at a six-ideal-layer separation. ΔA_{NC}, ΔA_{BC}, and ΔA_{BL} denote the FE change of the nanoconfined phase, bulk fluid system, and the boundary region between the nanoconfined phase and the bulk fluid respectively.

$$\Delta A_{NC} = \Delta(A_N * N) \tag{7.2}$$

$$\Delta A_{BC} = A_B * \Delta N \tag{7.3}$$

$$\Delta A_{BL} \approx 0 \tag{7.4}$$

Among these, the FE change of the entire nanoconfined phase (ΔA_{NC}) is defined as the change in the product of absolute FE of the nanoconfined phase (A_N) and the number of particles in the nanoconfined phase (N); the definition of the FE change of the entire bulk fluid system (ΔA_{BC}) is based on the assumption that the bulk is not influenced by the nanoconfined and its FE does not alter. The FE of the boundary layer (ΔA_{BL}) is assumed to stay constant.

Even though this is a large NVT simulation that is used to simulate a NPT process and given that the FE of entire system is an estimation, Figure 7.1 still reveals the oscillation between spontaneous and non-spontaneous processes (corresponding to negative and positive normal force respectively). This supports the aforementioned consistency shared by both experimental and simulation studies, and proves that the absolute FE measurement is able to describe the characteristic property of nanoconfined fluid behavior. Hence, in the following section, we compare the difference in details between both sides of the debate and employ absolute FE determination as a tool to further explore the nature of nanoconfined fluid behavior.

7.2 Comparison of Specifications in Experiments

While the key parameters, such as shear frequency, shear amplitude, and contact area diameter are directly included in Klein and coworkers' introduction to their experiment[16], the aforementioned key parameters are not all directly available in Granick's publication[90]. Therefore, we summarize the same parameters employed by Granick's group in previous experiments reported[7,15] and list them in the following table (Table 7.1)

Table 7.1. Comparison of shear frequency, shear amplitude, and contact area diameter in experiments employed by both sides.

	Surface Force Apparatus SFA	Surface Force Balance SFB
Shear Frequency (Hz)	1.3[7]	550[16]
Shear Amplitude (nm)	0.5[90]	1500[16]
Contact Area Diameter (μm)	100[15]	10[16]

To make the comparison in Table 7.1 more straightforward, a schematic plot is provided in Figure 7.2. As it shows, the experiment conducted by Klein and coworkers[16] has a smaller nanoconfined area, much higher shearing frequency, and a larger amplitude of shearing. It indicates that it is much easier to get the fluid particles outside of the nanoconfined region in Klein and coworkers' experiments[16] than in Granick's experiments. It also suggests that it is easier/faster to reach a thermodynamically stable state in the Klein apparatus. The difference in these key parameters might be the root cause of the opposing results reached by both sides.

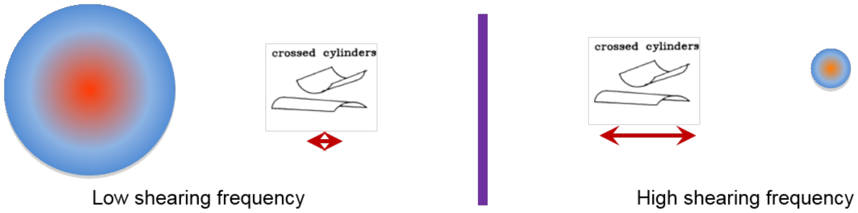

Figure 7.2. Schematic comparison of key parameters in both sides' experiments. **(Left)** Shear frequency, shear amplitude, and contact area diameter employed in Granick's experiment[7,15,90]. **(Right)** Shear frequency, shear amplitude, and contact area diameter employed in Klein's experiment[16].

7.3 Role of Larger Contact Area

Furthermore, it is important to note that typical simulations are performed with surface contact areas of $\sim 10^{-5}$ to $10^{-4} \mu m^2$, whereas experiments with the surface force balance (where solid phases are observed) have contact areas[3] of $\sim 10^2 \mu m^2$, and experiments with the surface force apparatus (where solid phases are not observed) have contact areas[15] of $\sim 10^4 \mu m^2$. The orders of magnitude difference in contact area may also play a significant role, influencing the dynamics and the ability to form the lowest free energy state. To investigate this, we performed GCMD simulations for increasing surface contact area, focusing on ordering with the central most layer; our interest is in whether the final structures are the same as those seen in the smaller simulations and how the time to order in these large simulations varies with pore contact area.

Specifically, we simulate two systems with 960,000 and 6,220,000 particles, each that can accommodate six ideal layers. If we assume that $\sigma_w = 3.5$ $\AA$, roughly the diameter of the potassium atoms in mica[149], we find that these systems have surface contact areas of $0.0021 \mu m^2$ (960,000 particles) and 0.014 μm^2 (6,220,000 particles). Simulations are performed by first disordering the system at $T^\star = 4.0$ and then instantaneously quenching to $T^\star = 1.1$; we monitor the in-plane 2-d hexagonal OP within the most central layer (i.e., $l = 3$ in Figure 6.5) as a function of time. $T^\star = 1.1$ places us just within the ordered regime predicted from the smaller system sizes (see Table 6.1).

In Figure 7.3 we plot the OP as a function of time for the two system sizes. The larger system requires a significantly longer time, by a factor of ~5, to reach the same level of ordering as the smaller system. The ratio of surface areas is ~6.6; extrapolating this trend, we would expect that a two order of magnitude increase in surface contact area would result in the system requiring a factor of ~75 more time to reach an equivalently ordered state. Previous work[160] has focused on the connection between rate of compression of the surfaces (i.e., the time at each separation the system has to relax) and the structure, conjecturing that higher-rates form non-equilibrium, jammed states. Clearly, this may be further exacerbated by surface size effects, where systems with larger contact areas simply take much longer to reach equilibrium, which may be further augmented by the significant effects that wall interaction strength and pore separation can have on the absolute free energy of the confined phase.

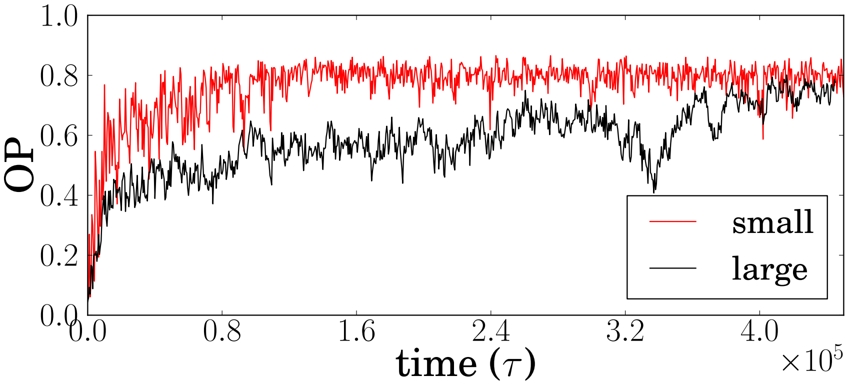

Figure 7.3. In-plane 2-d hexagonal order parameter within the central most layers (l=3) of a system that can accommodate 6 ideal layers as a function of time for *small* (960k particles) and *large* (6,220k particles).

7.4 Role of "Jammed" Atoms

As noted in the previous section, the dimensions of a nanoconfined region in experiments is $4 \sim 6$ orders of magnitude larger than the fluid molecule scale[3,15]. Considering that the thickness of a nanoconfined fluid is in the range of several molecular diameters, there is the possibility that extra fluid particles are jammed in the confined region as the two surfaces approach. It is necessary to take this into consideration, especially in the time scale used for the current experiment. Therefore, we measured the FE shift due to a change in the nanoconfined fluid density, in order to understand the role of jammed atoms its behavior.

Here, we artificially inserted particles into the nanoconfined region to mimic the jammed phenomena that possibly exists in experiments, then equilibrated the nanoconfined fluid systems and took their configurations for FE measurements. It is important to note here that we calculated the FE of the central layers instead of the nanoconfined fluid as a whole, since it is known that the central layers actually dominate the phase behavior of the nanoconfined fluid[138].

As shown in Figure 7.4, when comparing the FE of bulk solids under the same conditions, the nanoconfinement and the large fluid-wall interaction introduces an FE local minimum for the confined fluid, whereas the confined fluid is equal to unity and is in its stable state. However, as the local density increases due to the jammed atoms, the FE of the central layers increases sharply in comparison to the bulk solids. This indicates that jammed atoms, which may stem from insufficiently slow confinement speeds and large contact areas, have the potential to destabilize the nanoconfined solid if a nanoconfinement induced solid phase is formed. This interesting result provides a hint towards understanding the difference between Granick's and Klein's results: the reason why there is no fluid-solid phase transition observed in Granick's experiments might be due to the existence of "jammed" atoms.

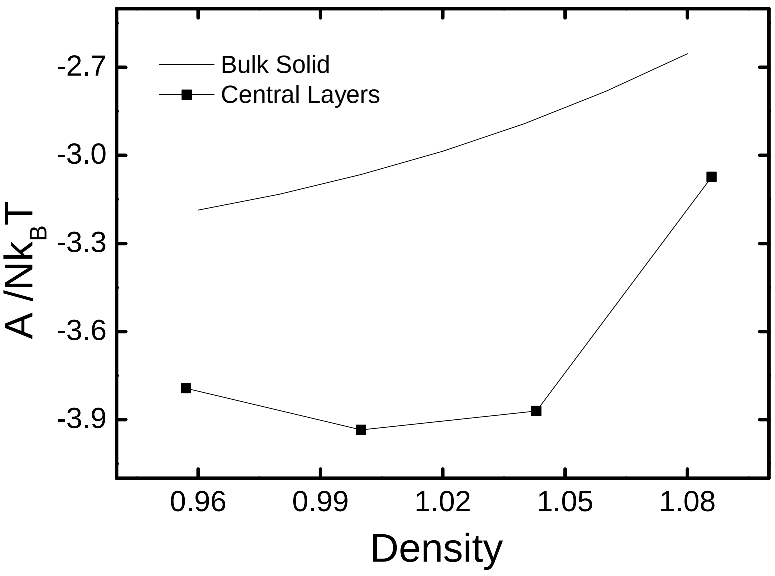

Figure 7.4. FE of central atoms as a function of the nanoconfined phase density, compared with FE of the bulk at the same density.

.

7.5 Fluid-Solid Oscillation

It is well known that the properties of a nanoconfined fluid are dramatically different compared to its corresponding bulk fluid. Current studies focus on exactly how the nanoconfined phase is different from its corresponding bulk. Is a solid formed when the wall-wall separation is below the critical value, or is a glassy state reached? Based on the FE measurements in the previous sections, our work seems to support the formation of a solid state. However, the theory that the nanoconfined phase transitions into a solid state below the critical separation is unable to give a reasonable explanation for the other researchers' results, including Granick's research and, more importantly, the experimental results from the larger AFM community. This indicates that simply viewing a nanoconfined phase that has a smaller separation than the critical value as solid, still misses some key points in the nanoconfined fluid phase behavior. Simply borrowing ideas from the macroscopic bulk behavior is not able to provide a complete description of the confined fluid behavior in nanoscale.

In view of this drawback to the current way of understanding, we introduce an alternative way to describe the nanoconfined fluid behavior, based on the difference in parameters in experiment and the role of "jammed" atoms in the nanoconfined phase. That is, the nanoconfined phase does not always stay in a solid state in any separation that is lower than the critical value. As the wall-wall separation is equal to an integer number of ideal layers, a solid state is formed that is different from its corresponding bulk. While the wall-wall separation is between an integer number of ideal layers, we assume that the nanoconfined fluid stays in a fluid-like state, which is different than the current way of understanding nanoconfined phase behavior.

Using this thought process, we can potentially resolve the differences between the work of Klein and Granick. Firstly, it supports the existence of a nanoconfinement-induced solid state, which is consistent with Klein and coworders' experimental results[2–4]. Secondly, the lack of a solid state observation in Granick and coworker's studies[11] can be explained by the much higher possibility of jamming fluid particles inside the nanoconfined region (even in a quasi-static compression manner), and the capability of jammed particles in destabilizing the nanoconfined phase. In other words, it is the jammed atoms that renders different observations in Klein's and Granick's experiments.

As shown schematically in Figure 7.5, due to the smaller nanoconfined area, a much higher shearing frequency, and a larger shear amplitude, fluid particles in Klein's experiment are able to leave the nanoconfined region much easier. Additionally, the much smaller nanoconfined area enables it to reach equilibrium faster. Contrary to Klein's experiment, the jamming of fluid particles inside the nanoconfined region, even in a quasi-static mode, is highly possible in Granick's experiment. This leads to no soild formation.

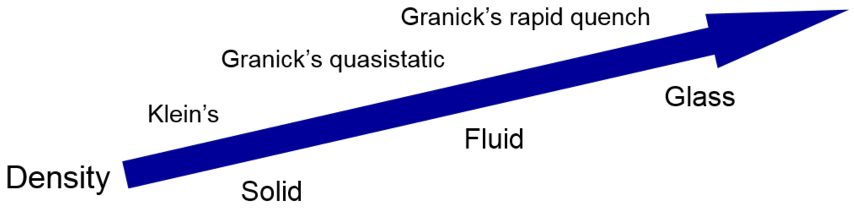

Figure 7.5. Schematic representation of the divergence and corresponding state of Granick's and Klein's experimental results using a new thought process that considers the oscillation

.

The newly introduced line of reasoning can also explain the lack of observation of a fluid-to-solid phase transition in AFM experiments. This is due to the probing style of AFM tips. In the experiment, the AFM is mainly moving up and down. Hence, it is more difficult for the fluid particles to leave the confined region. This is the same as in Granick's experiment. Due to the existence of the "jammed" fluid particles, the studies using AFM are also unable to observe the fluid-to-solid first order phase transition in nanoconfined phenomena. Thus, these contrary experimental results can be explained by this new thought process.

CHAPTER VIII

NANOCONFINED SYSTEMS WITH VARIOUS DENSITIES

8.1 Configurations at Various Densities

As demonstrated in Chapter VII, the density of the nanoconfined fluid (i.e., the "jammed" atoms) could be the source of the divergent observations in experimental studies. As a benefit from the absolute FE measurements used, we are now able to directly compare the relative stability of each state. Hence, in this chapter, the focus is placed on the nanoconfined fluid behavior at various confined phase densities.

We varied the nanoconfined phase density by means of artificially inserting/removing particles from the nanoconfined region, and subsequently equilibrating the system with the input of FE measurements (as shown in Figure 8.1). According to snapshots of each system, the well ordered structure is formed at the density $\rho^* = 1.00$, which is consistent with previous simulations.

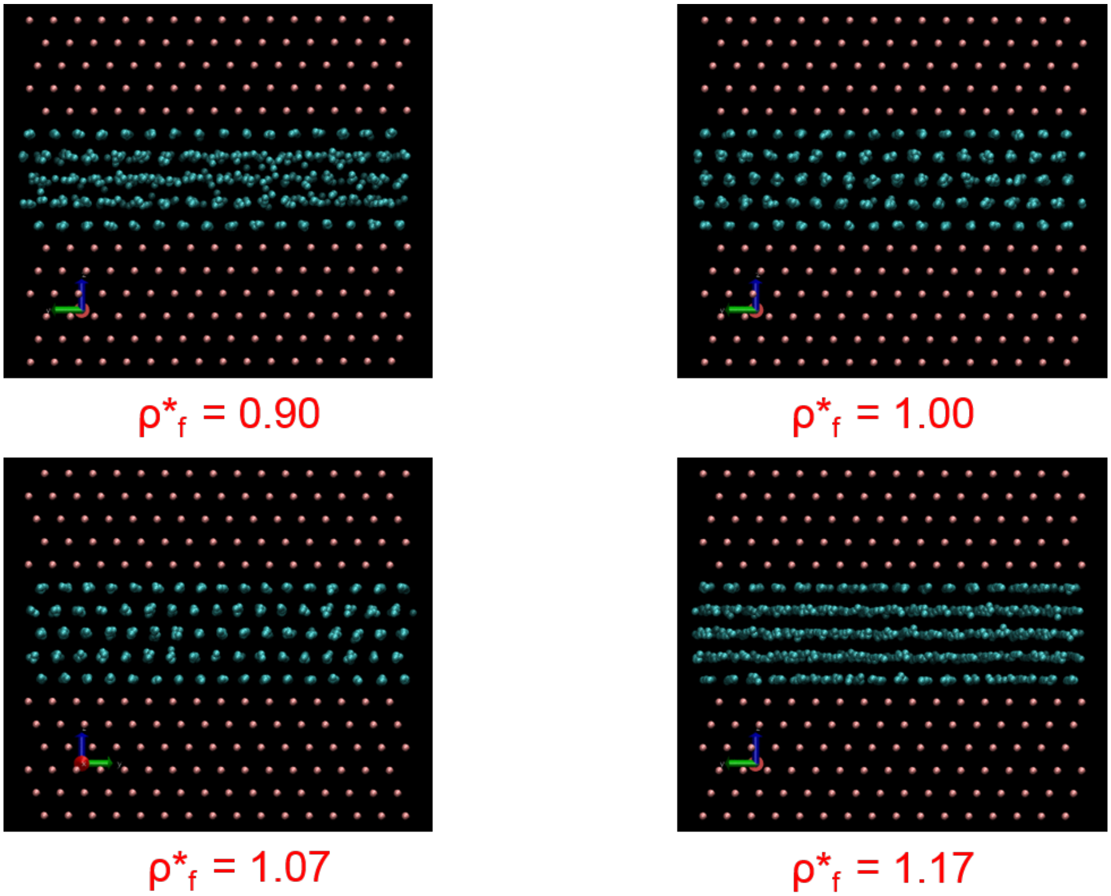

$\rho^*_f = 0.90$

$\rho^*_f = 1.00$

$\rho^*_f = 1.07$

$\rho^*_f = 1.17$

Figure 8.1. Snapshots of nanoconfined systems at various densities. $Separation = 5.0L, \varepsilon_{wm} = 4.00 * \varepsilon_{mm}, T^* = 1.00, \sigma_{mm} = \sigma_{ww}$. A well ordered structure is formed at the density $\rho^* = 1.00$.

8.2 Separation

We next determine the absolute Helmholtz FE of central layers in nanoconfined systems with separations ranging from 3 to 5 ideal layers at various nanoconfined phase densities. As detailed in previous sections, the nanoconfined fluid phase bahavior is dominated by its corresponding central layers. Because of this, the FE measurements in this section are concentrated on the central layers.

In Figure 8.2, the FE of the central layers at densities around $\rho^* = 1.00$ demonstrate a similar trend as the FE of central layers at $\rho^* = 1.00$. That is, a smaller wall-wall separation will lower the absolute Helmhotz FE of central layers and thus stabilize the nanoconfined phase. This trend is not affected by the actual density of the nanoconfined phase.

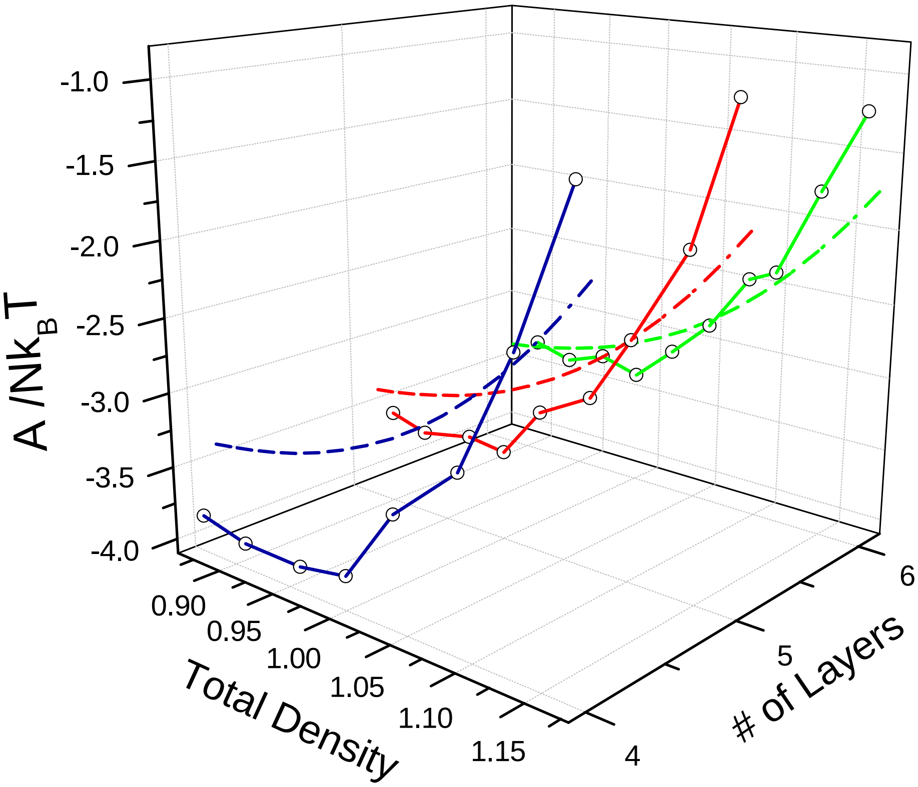

Figure 8.2. FE of central layers in nanoconfined system as a function of total density at different number of layers. **Blue** denotes 4 layers. **Red** denotes 5 layers. **Green** denotes 6 layers. **Dash-dot** line denotes FE of corresponding bulk.

8.3 Wall-Fluid Interaction

In addition to the wall-wall separation, we also further examined the role of wall-fluid interactions under various nanoconfined fluid phase densities. As shown in Figure 8.3 and Figure 8.4, wall-fluid interaction strengths $\varepsilon_{wm} = 1.0, 2.0, 4.0, 4.47$ have been employed in simulation studies and the central-layers FE measurements.

While there is a dramatic trend whereby a smaller wall-wall separation gives a lower central layers FE, the FE of the central layers does not obviously share a single, linear dependence on the wall-fluid interaction strength at all densities. This is different from previous studies in this work which show that a strong wall-fluid interaction strength will lower the FE of both the entire nanoconfined phase and its corresponding central layers. When the nanoconfined phase density is not equal to unity (especially at a density larger than unity), the FE of the central layers is not always lower at stronger wall-fluid interaction strength. This is a very interesting phenomenon.

Furthermore, a FE local minimum of the central layers occurs around the density of the nanoconfined phase equal to unity ($\rho^* = 1.0$) in all four of these interaction strength scenarios. This supports the thermodynamic stability of the nanoconfined phase with unity density. Nonetheless, as the density of the nanoconfined phase rises beyond unity ($\rho^* > 1.0$), the FE of the central layers increases sharply in almost all wall-wall separation and wall-fluid interaction strength conditions. This strongly suggests that the “jammed” atoms have the capability to destabilize the nanoconfined phase and thus render the supposed fluid-to-solid transition non-existent.

8.4 Boundary Layers

Given that particles in the central layers have a much higher mobility than those in the boundary layers, performing a FE calculation for the boundary layers by assuming that the central layer is stationary is not an accurate approach. Hence, this section does not directly measure FE of each part of the nanoconfined phase, but compares their corresponding densities instead.

As shown in Figure 8.3, the density of the boundary layers and the central layers gradually increases with the increment of the entire nanoconfind phase density, under the condition that the wall-fluid interaction strength is equal to that of the fluid-fluid interaction ($\varepsilon_{wm} = 1.0$). Meanwhile, in the system where the wall-fluid interaction strength is stronger than unity ($\varepsilon_{wm} > 1.0$) and the density of the nanoconfined phase is lower than unity ($\rho^* < 1.0$), the density of the boundary layers stays in unity (Shown in Figure 8.3 and Figure 8.4), whereas the density of the central layers keeps increasing with the increment of the nanoconfined phase density.

According to the density and FE comparison in Figure 8.3 and Figure 8.4, the system where the entire nanoconfined phase density is equal to unity ($\rho^* = 1.0$), serves as the turning point for the density and FE of the corresponding layers, while $\rho^* = 1.0$ itself is locally the most stable state.

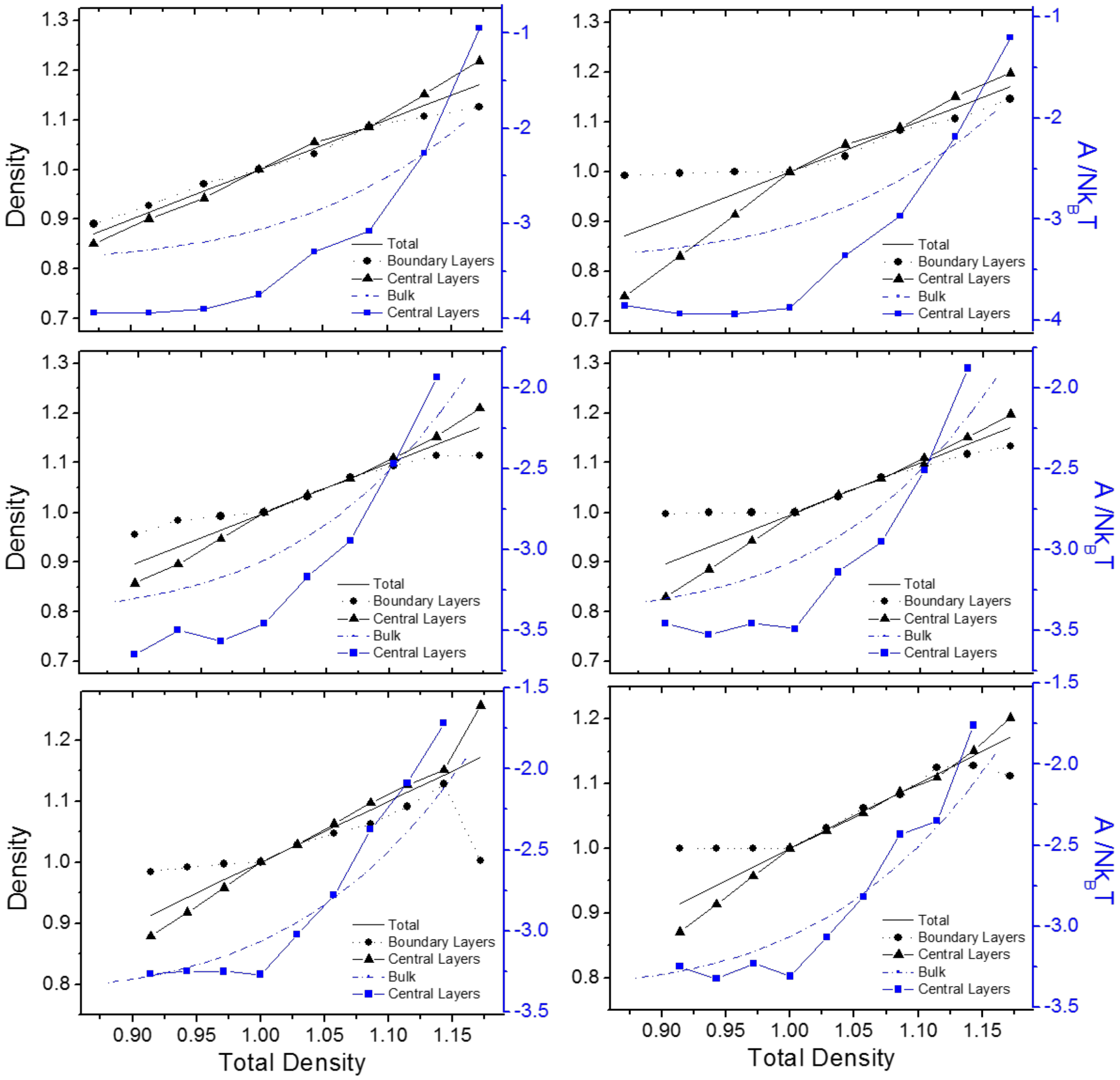

Figure 8.3. Absolute Helmholtz FE of central layers and densities of the central layers, the boundary layers, and the entire nanoconfined phase as a function of the nanoconfined fluid density. **Left** column: wall-fluid interaction strength $\varepsilon_{wm} = 1.0$. **Right** column: wall-fluid interaction strength $\varepsilon_{wm} = 2.0$. **Upper** row: 4 ideal layers. **Central** row: 5 ideal layers, **Bottom** row: 6 ideal layers.

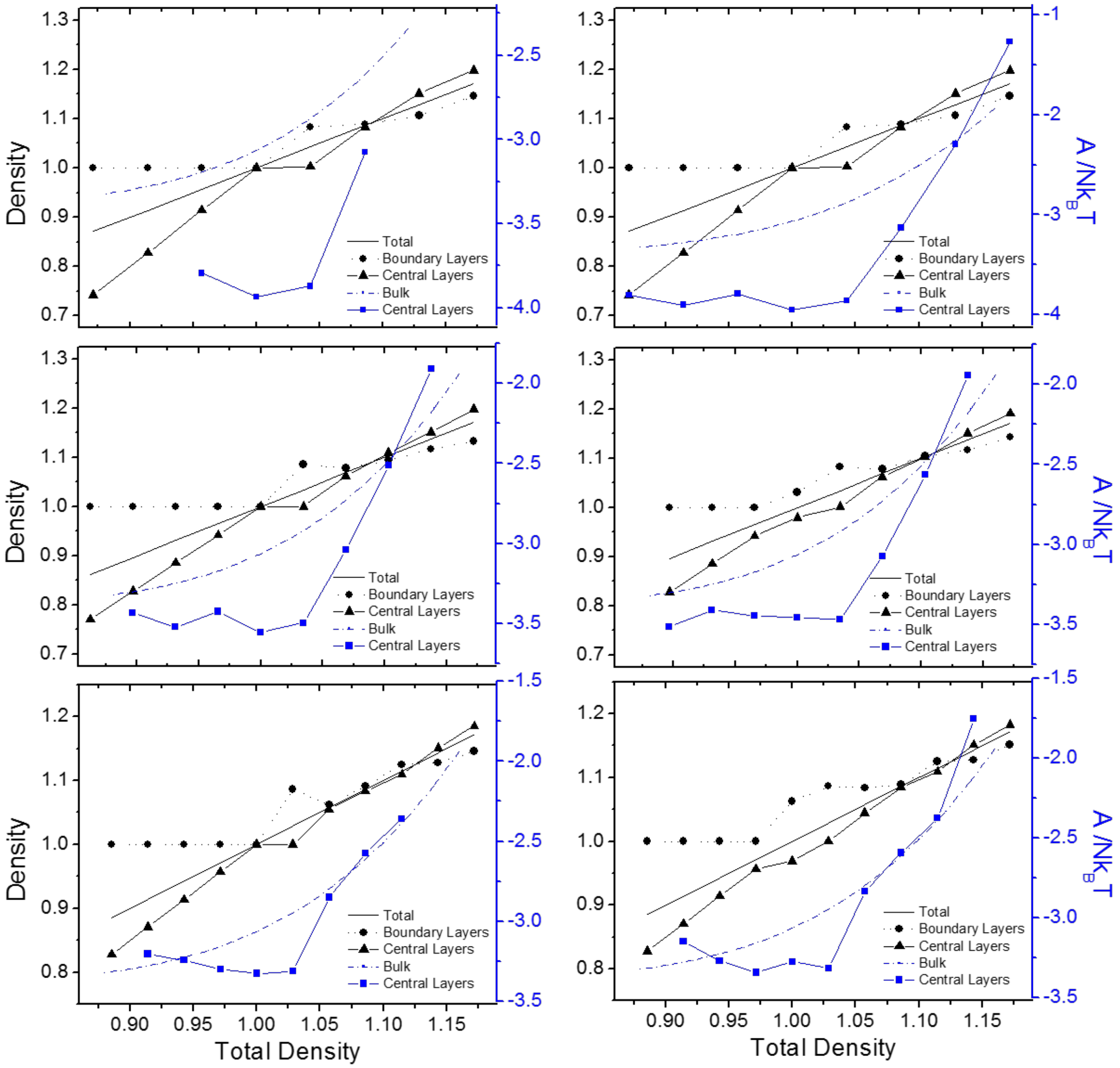

Figure 8.4. Absolute Helmholtz FE of central layers and densities of the central layers, the boundary layers, and the entire nanoconfined phase as a function of the nanoconfined fluid density. **Left** column: wall-fluid interaction strength $\varepsilon_{wm} = 4.0$. **Right** column: wall-fluid interaction strength $\varepsilon_{wm} = 4.47$. **Upper** row: 4 ideal layers. **Central** row: 5 ideal layers, **Bottom** row: 6 ideal layers. Left-hand side Epsilon 4.0.

CHAPTER IX

CONCLUSIONS AND FUTURE WORK

9.1 Conclusions

In this dissertation research we have developed absolute FE calculation strategies specifically for nanconfined systems, and subsequently employed these strategies as a research tool to reveal the nature of nanoconfined phase behavior, determine whether the layered and ordered state of the nanoconfined fluid observed in molecular simulation is thermodynamically stable, and attempt to resolve the two-decades-long debate in both experimental and simulation communities.

First, we revisited the basic algorithm of the Einstein crystal method and quantified the effects of simulation box shape, finite system size, and finite cutoff radius, paving the way for adaptation and further application of this method. We revealed that in continuous-potential modeled systems, the calculated FE shows dependence mainly on system size, rather than simulation box shape. Additionally, according to FE measurements conducted at various system sizes and crystal types, we demonstrated that FCC LJ crystals have the lowest free energy among the investigated basic LJ crystal types, and found that the FSC-asymptotic is a good option for finite-size correction strategy and has broader applications beyond the original scenario in which it was proposed. Moreover, according to direct comparison of the finite-cutoff-radius dependence of each stage, we have shown that it is stage one (ΔA_1) that dominates the finite-cutoff effect in the aforementioned Helmholtz absolute free energy calculations.

Subsequently, we extended the absolute free energy calculations to the study of nanoconfined fluid phase behavior. By utilizing a validated absolute Helmholtz free energy calculation algorithm specifically for nanoconfined fluid, we demonstrated that the free energy of the nanoconfined phase decreases as the wall-fluid interaction increases, and the melting point for nanoconfined fluid correspondingly showed a trend to shift to a higher temperature. This indicates that the fluid at certain temperatures has the potential to transition into a solid in the presence of a strong wall-fluid interaction and sufficient nanoconfinement.

Furthermore, by conducting free energy comparisons of perfectly stacked structures and structures with defects, we found that the nanoconfined phase as a whole prefers to form a structure distinct from its bulk as the separation narrows and the temperature decreases, because the structure with defects has a lower free energy.

It is important to note that our simulations and free energy calculations only explore the behavior of fluid/wall systems with commensurate fluid and wall molecular sizes. This is by design to simplify the analysis and enable comparison with bulk crystalline structures. Incommensurability of sizes may play an important role, shifting the free energy due to a competition between ordering dictated by the wall roughness and the preferred crystallinity and spacing of the fluid. Specifically, it has been observed that the relative orientation of herringbone structures observed for nanoconfined alkanes depend strongly on the structure of the walls[85,159,163]; however, the accumulation of simulation results to date suggests that incommensurability does not lead to the elimination of the ODT. The FE measurements on systems with different fluid-wall particle size ratios agree with previous experimental and simulation studies. Given that fluid particles are larger in size compared to wall crystal spacing, the slightly lower FE further stabilizes the nanoconfined solid phase.

We then extended the free energy measurements to more realistic GCMD simulations. Combining GCMD simulations with absolute free energy measurements in studies of nanoconfined fluid phase behavior, we demonstrated that the absolute Helmholtz free energy of the nanoconfined region is not equal to that of its corresponding bulk fluid. The much lower free energy of the nanoconfined region compared with its bulk fluid indicates that the fluid may undergo a fluid-to-solid phase transition as the separation decreases. This demonstrates consistency with the observations previously reported by experimentalists[6,16,47] and other researchers focused on simulation[89,94].

Meanwhile, the focus of free energy measurements in GCMD simulations is not only on the entire nanoconfined phase, but also on the behavior of different regions inside the nanoconfined phase. We showed that particles in contact with the pore walls demonstrate markedly different behavior than those in the central most region, whereas atoms in the central most region ultimately dictate the solidification. Using this, we calculated the Helmholtz free energy of the central region alone, factoring out the effects of the strong wall interactions. For systems with interaction strengths closely matching mica-organic molecule parameters, we found that this transition occurs at roughly 6 layers, in good agreement with previous simulations and experiments.

However, this agreement, mainly with observations by Klein's group[6,16,47] and other researchers focusing on simulation[89,94], is not able to provide a reasonable explanation as to why Granick's observations are so dramatically different with Klein's results or why the experimental data from the AFM community actually supports Granick's perspective.

We started with the consistencies between the two sides of the debate, then compared their differences in experimental conditions and studied the possible role of these factors in the dramatically different experimental results. This revealed the significant role that surface contact area plays in the ordering process; the additional time needed to order scales roughly with the ratio of surface contact area.

More interestingly, our free energy measurements on central layers of artificially increased nanoconfined phase density indicate that the jammed atoms have the potential to destabilize the nanoconfinement-induced solid structure. This provides hints to the question of why the experimental results reported by some researchers[11] is contrary to others[6,16,47].

Consequently, we suggested a novel thought process to better describe the nature of nanoconfined fluid behavior. The new thought process replaces the old macroscopic view of the nanoconfinement-induced solid, like a bulk solid below the melting temperature, into discrete solid states formed at separations around integer numbers of ideal layers, and it well explains the origin of the differences seen among researchers focusing on experimental studies.

Finally, our investigations on the nanoconfined system with various densities further support the idea that "jammed" atoms have the capability to destabilize the nanoconfined solid phase and remove the supposed fluid-to-solid transition.

To sum up, this dissertation research reviewed fundamental issues in solid FE determinations, supported the existence of a nanoconfinement-induced fluid-to-solid phase transition via absolute FE measurements, and introduced a theory that better reveals the nature of nanoconfined fluid behavior and reconciles the difference among experimental studies.

9.2 Future work

9.2.1 Free Energy of Fluid State

An important study that has yet to be completed in this work is the development of a method to determine the absolute Helmholtz FE of nanoconfined systems in a fluid state. The nanoconfined fluid is a highly dense system. Employing the aforementioned insertion method[100] to sample a fluid system with a large density is extremely inefficient. Additionally, the nanoconfined fluid system in scenarios that are close to experimental conditions, such as large wall-fluid interaction strengths, has a strong tendency to form a well-ordered structure. That places an extra hurdle on the way to directly measuring the absolute Helmholtz FE of nanoconfined systems in a fluid state.

In this work, we mostly used an indirect approach to estimate the FE of a nanoconfined system in a fluid state. That is, measuring the density of the nanoconfined system and then bringing the measured density value into the FE formula for the bulk fluid to then obtain the FE of the nanoconfined system. However, the implementation of the aforementioned indirect approach brings systematic error and, hence, undermines the conclusions that are reached in this work. Therefore, the introduction of a novel FE calculation strategy to directly and efficiently measure the absolute FE of a nanoconfined system in a fluid state is a primary goal in the near future.

9.2.2 Oscillatory Properties

In Chapter VII we advanced the understanding of nanoconfined fluid behavior to an oscillatory nature, which was a benefit from the ease in which we could directly compare the absolute FE. More importantly, by employing this novel theory, we were able to explain the dramatic difference seen in experimental studies, based on their different experimental conditions.

Nonetheless, the support provided by this dissertation research is preliminary and not definitively strong. Aside from the need to develop the aforementioned FE calculation method for a nanoconfined system in a fluid state, simulation and experimental studies with specific emphasis on the oscillatory properties of nanoconfined systems are required. The potential applications of the nanoconfined-fluid's oscillatory properties, such as normal-force-adjusted viscosity, super lubrication, etc., are also very interesting topics to study. When an external pressure is applied perpendicularly to the solid, the nanoconfined system becomes fluid and functions as a lubricant. While the normal force is removed, the lubricant turns back to a solid state. The viscosity is increased to several orders of magnitude and blocks the relative motion of the wall.

9.2.3 Chemical Reactions

The mechanism by which the nanoconfined phase oscillates between a solid state and a corresponding fluid state as the wall-wall separation varies, creates a special environment for polymerization or biochemical reactions.

The well-ordered structure of the nanoconfined phase has the potential to cage reactive functional groups inside a small region, and hence increase the frequency and probability of effective collisions in chemical reactions. After the reaction is completed, the disordered state between two adjacent ordered states and the increased fluidity as a result, forms perfect channels for the reaction product to leave the nanoconfined region. Most recently, DNA microfluidic nanochannnels[164] have been used to conduct DNA sequencing and synthesis.

It would be interesting to investigate the change in chemical reactions that are occurring in the nanoconfined phase, as the wall-wall separation gradually decreases or increases.

Appendix A

Modified Tail Correction

The detailed step-by-step derivation of the modified tail correction is demonstrated here. In nanoconfined systems, correction of the potential for finite cutoff radius includes contributions from both fluid-fluid interaction potential within the nanoconfined phase, and also fluid-wall interaction potential due to the existence of solid walls. It models the behavior of nanoconfined systems, and is, therefore, more accurate than the generally-used tail corrections.

In the following equation, S is the surface area of a spherical shell (including the surface area of the partial sphere inside the nanoconfined phase and in the solid wall), r_c is the cutoff distance used in the potential calculation, and the subscripts m and w, respectively, specify mobile fluid particles and static wall particles. ρ is density, r is distance, h is the wall-wall separation, U is potential energy, and σ is the interatomic distance at which the potential energy is equal to zero.

$$
\begin{aligned}
U^{tail} &= \frac{1}{2}\int_{r_c}^{\infty} dr\rho SU\left(r\right)\\
&= \frac{1}{2}\int_{r_c}^{\infty} dr\left[\rho_m S_m U_{mm}\left(r\right)+\rho_w S_w U_{wm}\left(r\right)\right]\\
&= \frac{1}{2}\int_{r_c}^{\infty} dr\left[\rho_m 2\pi rhU_{mm}\left(r\right)+\rho_w 2\pi r\left(2r-h\right)U_{wm}\left(r\right)\right]\\
&= \frac{1}{2}\int_{r_c}^{\infty} dr\left[\rho_m 2\pi rhU_{mm}\left(r\right)\right]-\frac{1}{2}\int_{r_c}^{\infty} dr\left[\rho_w 2\pi rhU_{wm}\left(r\right)\right]+\frac{1}{2}\int_{r_c}^{\infty} dr\left[\rho_w 2\pi r*2rU_{wm}\left(r\right)\right]\\
&= \pi h\rho_m\int_{r_c}^{\infty} dr\left[rU_{mm}\left(r\right)\right]-\pi h\rho_w\int_{r_c}^{\infty} dr\left[rU_{wm}\left(r\right)\right]+2\pi\rho_w\int_{r_c}^{\infty} dr\left[r^2U_{wm}\left(r\right)\right]\\
&= \pi h\rho_m\int_{r_c}^{\infty} dr\left[r*4\varepsilon_{mm}\left(\left(\frac{\sigma_{mm}}{r}\right)^{12}-\left(\frac{\sigma_{mm}}{r}\right)^{6}\right)\right]-\pi h\rho_w\int_{r_c}^{\infty} dr\left[r*4\varepsilon_{wm}\left(\left(\frac{\sigma_{wm}}{r}\right)^{12}-\left(\frac{\sigma_{wm}}{r}\right)^{6}\right)\right]\\
&\quad +2\pi\rho_w\int_{r_c}^{\infty} dr\left[r^2*4\varepsilon_{wm}\left(\left(\frac{\sigma_{wm}}{r}\right)^{12}-\left(\frac{\sigma_{wm}}{r}\right)^{6}\right)\right]\\
&= 4\pi h\rho_m\varepsilon_{mm}\sigma_{mm}\int_{r_c}^{\infty} dr\left[\left(\frac{\sigma_{mm}}{r}\right)^{11}-\left(\frac{\sigma_{mm}}{r}\right)^{5}\right]-4\pi h\rho_w\varepsilon_{wm}\sigma_{wm}\int_{r_c}^{\infty} dr\left[\left(\frac{\sigma_{wm}}{r}\right)^{11}-\left(\frac{\sigma_{wm}}{r}\right)^{5}\right]\\
&\quad +8\pi\rho_w\varepsilon_{wm}\sigma_{wm}^2\int_{r_c}^{\infty} dr\left[\left(\frac{\sigma_{wm}}{r}\right)^{10}-\left(\frac{\sigma_{wm}}{r}\right)^{4}\right]\\
&= 4\pi h\rho_m\varepsilon_{mm}\sigma_{mm}\left\{-\frac{\sigma_{mm}}{10}\left[\left(\frac{\sigma_{mm}}{\infty}\right)^{10}-\left(\frac{\sigma_{mm}}{r_c}\right)^{10}\right]+\frac{\sigma_{mm}}{4}\left[\left(\frac{\sigma_{mm}}{\infty}\right)^{4}-\left(\frac{\sigma_{mm}}{r_c}\right)^{4}\right]\right\}\\
&\quad -4\pi h\rho_w\varepsilon_{wm}\sigma_{wm}\left\{-\frac{\sigma_{wm}}{10}\left[\left(\frac{\sigma_{wm}}{\infty}\right)^{10}-\left(\frac{\sigma_{wm}}{r_c}\right)^{10}\right]+\frac{\sigma_{wm}}{4}\left[\left(\frac{\sigma_{wm}}{\infty}\right)^{4}-\left(\frac{\sigma_{wm}}{r_c}\right)^{4}\right]\right\}\\
&\quad +8\pi\rho_w\varepsilon_{wm}\sigma_{wm}^2\left\{-\frac{\sigma_{wm}}{9}\left[\left(\frac{\sigma_{wm}}{\infty}\right)^{9}-\left(\frac{\sigma_{wm}}{r_c}\right)^{9}\right]+\frac{\sigma_{wm}}{3}\left[\left(\frac{\sigma_{wm}}{\infty}\right)^{3}-\left(\frac{\sigma_{wm}}{r_c}\right)^{3}\right]\right\}\\
&= 4\pi h\rho_m\varepsilon_{mm}\sigma_{mm}^2\left\{\frac{1}{10}\left(\frac{\sigma_{mm}}{r_c}\right)^{10}-\frac{1}{4}\left(\frac{\sigma_{mm}}{r_c}\right)^{4}\right\}-4\pi h\rho_w\varepsilon_{wm}\sigma_{wm}^2\left\{\frac{1}{10}\left(\frac{\sigma_{wm}}{r_c}\right)^{10}-\frac{1}{4}\left(\frac{\sigma_{wm}}{r_c}\right)^{4}\right\}\\
&\quad +8\pi\rho_w\varepsilon_{wm}\sigma_{wm}^3\left\{\frac{1}{9}\left(\frac{\sigma_{wm}}{r_c}\right)^{9}-\frac{1}{3}\left(\frac{\sigma_{wm}}{r_c}\right)^{3}\right\}\\
&= 2\pi h\rho_m\varepsilon_{mm}\sigma_{mm}^2\left\{\frac{1}{5}\left(\frac{\sigma_{mm}}{r_c}\right)^{10}-\frac{1}{2}\left(\frac{\sigma_{mm}}{r_c}\right)^{4}\right\}-2\pi h\rho_w\varepsilon_{wm}\sigma_{wm}^2\left\{\frac{1}{5}\left(\frac{\sigma_{wm}}{r_c}\right)^{10}-\frac{1}{2}\left(\frac{\sigma_{wm}}{r_c}\right)^{4}\right\}\\
&\quad +\frac{8}{3}\pi\rho_w\varepsilon_{wm}\sigma_{wm}^3\left\{\frac{1}{3}\left(\frac{\sigma_{wm}}{r_c}\right)^{9}-\left(\frac{\sigma_{wm}}{r_c}\right)^{3}\right\}
\end{aligned}
$$

REFERENCES

[1]Gee, M. L.; McGuiggan, P. M.; Israelachvili, J. N.; Homola, A. M. *The Journal of Chemical Physics* **1990**, *93*, 1895–1906.

[2]Klein, J.; Kumacheva, E. *Science* **1995**, *269*, 816–819.

[3]Klein, J.; Kumacheva, E. *The Journal of Chemical Physics* **1998**, *108*, 6996–7009.

[4]Kumacheva, E.; Klein, J. *The Journal of Chemical Physics* **1998**, *108*, 7010–7022.

[5]Demirel, A. L.; Granick, S. *Physical Review Letters* **1996**, *77*, 2261–2264.

[6]Klein, J.; Kumacheva, E. *Science* **1995**, *269*, 816–819.

[7]Zhu, Y.; Granick, S. *Langmuir* **2003**, *19*, 8148–8151.

[8]Granick, S. *Science* **1991**, *253*, 1374–1379.

[9]Ohnishi, S.; Hato, M.; Tamada, K.; Christenson, H. K. *Langmuir* **1999**, *15*, 3312–3316.

[10]Kohonen, M. M.; Meldrum, F. C.; Christenson, H. K. *Langmuir* **2003**, *19*, 975–976.

[11]Zhu, Y.; Granick, S. *Langmuir* **2003**, *19*, 8148–8151.

[12]Radhakrishnan, R.; Gubbins, K. E. *Molecular Physics* **1999**, *96*, 1249–1267.

[13]Radhakrishnan, R.; Gubbins, K. E.; Sliwinska-Bartkowiak, M. *The Journal of Chemical Physics* **2000**, *112*, 11048–11057.

[14]Evans, R.; Marconi, U. M. B. *The Journal of Chemical Physics* **1987**, *86*, 7138–7148.

[15]Vanalsten, J.; Granick, S. *Physical Review Letters* **1988**, *61*, 2570–2573.

[16]Klein, J.; Kumacheva, E. *Journal of Chemical Physics* **1998**, *108*, 6996–7009.

[17]Tufte, O. N.; Chapman, P. W.; Long, D. *Journal of Applied Physics* **1962**, *33*, 3322–3327.

[18]Nathanson, H. C.; Wickstrom, R. A. *Applied Physics Letters* **1965**, *7*, 84–86.

[19]Chollet, F.; Liu, H. A short introduction to Micro Electro Mechanical Systems. 2012; http://memscyclopedia.org/introMEMS.html.

[20]Maluf, N.; Williams, K. *An Introduction to Microelectromechanical Systems Engineering 2nd Ed.*; MEMS Microelectromechanical Systems Series; Artech House Incorporated, 2004.

[21]Roukes, M. *Physics World* **2001**, *14*, 25–31.

[22]Lab, S. N. A mite approaching the gear chain. 2008; http://mems.sandia.gov/gallery/images/Bug_1b.jpg.

[23]Kroto, H. W.; Heath, J. R.; O'Brien, S. C.; Curl, R. F.; Smalley, R. E. *Nature* **1985**, *318*, 162–163.

[24]Heath, J.; O'Brien, S.; Zhang, Q.; Liu, Y.; Curl, R.; Tittel, F.; Smalley, R. *Journal of the American Chemical Society* **1985**, *107*, 7779–7780.

[25]Zhang, Q.-L.; O'Brien, S.; Heath, J.; Liu, Y.; Curl, R.; Kroto, H.; Smalley, R. *The Journal of Physical Chemistry* **1986**, *90*, 525–528.

[26]Novoselov, K. S.; Geim, A. K.; Morozov, S.; Jiang, D.; Zhang, Y.; Dubonos, S.; Grigorieva, I.; Firsov, A. *Science* **2004**, *306*, 666–669.

[27]Guo, T.; Nikolaev, P.; Rinzler, A. G.; Tomanek, D.; Colbert, D. T.; Smalley, R. E. *The Journal of Physical Chemistry* **1995**, *99*, 10694–10697.

[28]Guo, T.; Nikolaev, P.; Thess, A.; Colbert, D.; Smalley, R. *Chemical Physics Letters* **1995**, *243*, 49–54.

[29]Mstroeck, Illustration of eight of the allotropes that pure carbon can take. 2006; http://en.wikipedia.org/wiki/File:Eight_Allotropes_of_Carbon.png.

[30]Xu, J. F.; Kiely, J. D.; Hsia, Y. T.; Talke, F. E. *Microsystem Technologies-Micro-and Nanosystems-Information Storage and Processing Systems* **2009**, *15*, 687–693.

[31]Swann, D. A.; Bloch, K. J.; Swindell, D.; Shore, E. *Arthritis & Rheumatism* **1984**, *27*, 552–556.

[32]Chen, M.; Briscoe, W. H.; Armes, S. P.; Klein, J. *Science* **2009**, *323*, 1698–1701.

[33]Orgel, L. E. *Trends in Biochemical Sciences* **1998**, *23*, 491–495.

[34]Paukstelis, P. J.; Chen, J.-H.; Chase, E.; Lambowitz, A. M.; Golden, B. L. *Nature* **2008**, *451*, 94–97.

[35]Miller, S. L. *Science* **1953**, *117*, 528–529.

[36]Ring, D.; Wolman, Y.; Friedmann, N.; Miller, S. L. *Proceedings of the National Academy of Sciences* **1972**, *69*, 765–768.

[37]Fabene, P. F.; Bentivoglio, M. *Brain Research Bulletin* **1998**, *47*, 195–198.

[38]Sun, G.; Giovambattista, N.; Wang, E.; Xu, L. *Soft Matter* **2013**, *9*, 11374–11382.

[39]Binnig, G.; Quate, C. F.; Gerber, C. *Physical Review Letters* **1986**, *56*, 930.

[40]O'Shea, S.; Welland, M.; Pethica, J. *Chemical Physics Letters* **1994**, *223*, 336–340.

[41]Erlandsson, R.; McClelland, G.; Mate, C.; Chiang, S. *Journal of Vacuum Science & Technology A* **1988**, *6*, 266–270.

[42]Israelachvili, J. N.; Adams, G. E. *Nature* **1976**, *262*, 773–776.

[43]Israelachvili, J. N.; Adams, G. E. *Journal of the Chemical Society-Faraday Transactions I* **1978**, *74*, 975–1001.

[44]Tabor, D.; Winterton, R. H. S. *Nature* **1968**, *219*, 1120–1121.

[45]Tabor, D.; Winterton, R. H. S. *Proceedings of the Royal Society of London Series a-Mathematical and Physical Sciences* **1969**, *312*, 435–450.

[46]Israelachvili, J. N. *Proceedings of the National Academy of Sciences of the United States of America* **1987**, *84*, 4722–4724.

[47]Kumacheva, E.; Klein, J. *Journal of Chemical Physics* **1998**, *108*, 7010–7022.

[48]Vanalsten, J.; Granick, S. *Physical Review Letters* **1988**, *61*, 2570–2573.

[49]Israelachvili, J. N.; Mcguiggan, P. M.; Homola, A. M. *Science* **1988**, *240*, 189–191.

[50]Bowden, F. P.; Tabor, D. *Doubleday, New York* **1973**,

[51]Granick, S. *Science* **1991**, *253*, 1374–1379.

[52]Gee, M. L.; Mcguiggan, P. M.; Israelachvili, J. N.; Homola, A. M. *Journal of Chemical Physics* **1990**, *93*, 1895–1906.

[53]Hardy, W. *Proceedings of the Royal Society of London. Series A* **1912**, *86*, 610–635.

[54]Henniker, J. C. *Rev. Mod. Phys.* **1949**, *21*, 322–341.

[55]Raviv, U.; Klein, J. *Science* **2002**, *297*, 1540–1543.

[56]Klein, J.; Raviv, U.; Perkin, S.; Kampf, N.; Chai, L.; Giasson, S. *Journal of Physics-Condensed Matter* **2004**, *16*, 5437–5448.

[57]Demirel, A. L.; Granick, S. *Physical Review Letters* **1996**, *77*, 2261–2264.

[58]Becker, T.; Mugele, F. *Physical Review Letters* **2003**, *91*, 166104.

[59]Lin, Z. Q.; Granick, S. *Langmuir* **2003**, *19*, 7061–7070.

[60]Ohnishi, S.; Hato, M.; Tamada, K.; Christenson, H. K. *Langmuir* **1999**, *15*, 3312–3316.

[61]Kohonen, M. M.; Meldrum, F. C.; Christenson, H. K. *Langmuir* **2003**, *19*, 975–976.

[62]Frantz, P.; Salmeron, M. *Tribology Letters* **1998**, *5*, 151–153.

[63]Israelachvili, J.; Maeda, N.; Akbulut, M. *Langmuir* **2006**, *22*, 2397–2398.

[64]Bureau, L. *Physical Review Letters* **2007**, *99*, 225503.

[65]Maali, A.; Cohen-Bouhacina, T.; Couturier, G.; Aimé, J.-P. *Phys. Rev. Lett.* **2006**, *96*, 086105.

[66]Kaggwa, G. B.; Kilpatrick, J. I.; Sader, J. E.; Jarvis, S. P. *Applied Physics Letters* **2008**, *93*, 011909.

[67]de Beer, S.; van den Ende, D.; Mugele, F. *Nanotechnology* **2010**, *21*, 325703.

[68]de Beer, S.; den Otter, W. K.; van den Ende, D.; Briels, W. J.; Mugele, F. *EPL (Europhysics Letters)* **2012**, *97*, 46001.

[69]Israelachvili, J.; Min, Y.; Akbulut, M.; Alig, A.; Carver, G.; Greene, W.; Kristiansen, K.; Meyer, E.; Pesika, N.; Rosenberg, K.; Zeng, H. *Reports on Progress in Physics* **2010**, *73*, 036601.

[70]Nygard, K.; Satapathy, D.; Bunk, O.; Diaz, A.; Perret, E.; Buitenhuis, J.; Pfeiffer, F.; David, C.; van der Veen, F. *Optics Express* **2008**, *16*, 20522–20529.

[71]Raviv, U.; Laurat, P.; Klein, J. *Nature* **2001**, *413*, 51–54.

[72]Leng, Y.; Cummings, P. T. *Physical Review Letters* **2005**, *94*, 026101.

[73]Leng, Y.; Cummings, P. T. *The Journal of Chemical Physics* **2006**, *124*, 074711.

[74]Radhakrishnan, R.; Gubbins, K. E.; Sliwinska-Bartkowiak, M. *The Journal of Chemical Physics* **2000**, *112*, 11048–11057.

[75]Ludwig, R. *Angewandte Chemie International Edition* **2001**, *40*, 1808–1827.

[76]Thompson, P. A.; Robbins, M. O. *Science* **1990**, *250*, 792–794.

[77]Thompson, P. A.; Grest, G. S.; Robbins, M. O. *Physical Review Letters* **1992**, *68*, 3448.

[78]Gao, J. P.; Luedtke, W. D.; Landman, U. *Physical Review Letters* **1997**, *79*, 705–708.

[79]Gao, J. P.; Luedtke, W. D.; Landman, U. *Journal of Physical Chemistry B* **1997**, *101*, 4013–4023.

[80]Gao, J. P.; Luedtke, W. D.; Landman, U. *Journal of Chemical Physics* **1997**, *106*, 4309–4318.

[81]Gao, J. P.; Luedtke, W. D.; Landman, U. *Tribology Letters* **2000**, *9*, 3–13.

[82]Gelb, L. D.; Gubbins, K. E.; Radhakrishnan, R.; Sliwinska-Bartkowiak, M. *Reports on Progress in Physics* **1999**, *62*, 1573.

[83]Cui, S. T.; Cummings, P. T.; Cochran, H. D. *Journal of Chemical Physics* **1999**, *111*, 1273–1280.

[84]Cui, S. T.; Cummings, P. T.; Cochran, H. D. *Fluid Phase Equilibria* **2001**, *183*, 381–387.

[85]Cui, S. T.; Cummings, P. T.; Cochran, H. D. *Journal of Chemical Physics* **2001**, *114*, 7189–7195.

[86]Cui, S. T.; McCabe, C.; Cummings, P. T.; Cochran, H. D. *Journal of Chemical Physics* **2003**, *118*, 8941–8944.

[87]Jabbarzadeh, A.; Harrowell, P.; Tanner, R. I. *Macromolecules* **2003**, *36*, 5020–5031.

[88]Jabbarzadeh, A.; Harrowell, P.; Tanner, R. I. *Physical Review Letters* **2005**, *94*, 126103.

[89]Docherty, H.; Cummings, P. T. *Soft Matter* **2010**, *6*, 1640–1643.

[90]Zhu, Y.; Granick, S. *Physical Review Letters* **2004**, *93*, 096101.

[91]Siepmann, J. I.; Karaborni, S.; Smit, B. *Nature* **1993**, *365*, 330–332.

[92]Siepmann, J. I.; Karaborni, S.; Smit, B. *Nature* **1993**, *365*, 330–332.

[93]Heinz, H.; Koerner, H.; Anderson, K. L.; Vaia, R. A.; Farmer, B. L. *Chemistry of Materials* **2005**, *17*, 5658–5669.

[94]Cummings, P. T.; Docherty, H.; Iacovella, C. R.; Singh, J. K. *AICHE Journal* **2010**, *56*, 842–848.

[95]Jorgensen, W. L.; Maxwell, D. S.; TiradoRives, J. *Journal of the American Chemical Society* **1996**, *118*, 11225–11236.

[96]Alba-Simionesco, C.; Coasne, B.; Dosseh, G.; Dudziak, G.; Gubbins, K. E.; Radhakrishnan, R.; Sliwinska-Bartkowiak, M. *Journal of Physics: Condensed Matter* **2006**, *18*, R15.

[97]Chaikin, P. M.; Lubensky, T. C. *Principles of Condensed Matter Physics*; Cambridge Univ Press, 2000; Vol. 1.

[98]Girifalco, L. A. *Statistical Mechanics of Solids*; Oxford University Press, 2003; Vol. 58.

[99]Oxtoby, D. W. *Nature* **1990**, *347*, 725–730.

[100]Frenkel, D.; Smit, B. *Understanding Molecular Simulation: From Algorithms to Applications*; Computational science series; Elsevier Science, 2001.

[101]Vega, C.; Sanz, E.; Abascal, J. L. F.; Noya, E. G. *Journal of Physics: Condensed Matter* **2008**, *20*, 153101.

[102]Rosenfeld, Y. *Physical Review Letters* **1989**, *63*, 980.

[103]Tillner-Roth, R.; Friend, D. G. *Journal of Physical and Chemical Reference Data* **1998**, *27*, 63–96.

[104]Hoover, W. G.; Gray, S. G.; Johnson, K. W. *The Journal of Chemical Physics* **1971**, *55*, 1128–1136.

[105]Hoover, W. G.; Ross, M.; Johnson, K. W.; Henderson, D.; Barker, J. A.; Brown, B. C. *The Journal of Chemical Physics* **1970**, *52*, 4931–4941.

[106]Frenkel, D.; Ladd, A. J. C. *Journal of Chemical Physics* **1984**, *81*, 3188–3193.

[107]Wang, F. G.; Landau, D. P. *Physical Review Letters* **2001**, *86*, 2050–2053.

[108]Tan, T. B.; Schultz, A. J.; Kofke, D. A. *Journal of Chemical Physics* **2010**, *132*, 214103.

[109]Widom, B. *The Journal of Chemical Physics* **1963**, *39*, 2808–2812.

[110]Hoover, W. G.; Ree, F. H. *The Journal of Chemical Physics* **1967**, *47*, 4873–4878.

[111]Hoover, W. G.; Ree, F. H. *The Journal of Chemical Physics* **1968**, *49*, 3609–3617.

[112]Ogura, H.; Matsuda, H.; Ogawa, T.; Ogita, N.; Ueda, A. *Progress of Theoretical Physics* **1977**, *58*, 419–433.

[113]Bruce, A. D.; Wilding, N. B.; Ackland, G. J. *Phys. Rev. Lett.* **1997**, *79*, 3002–3005.

[114]Wilding, N. B.; Bruce, A. D. *Phys. Rev. Lett.* **2000**, *85*, 5138–5141.

[115]Wilms, D.; Wilding, N. B.; Binder, K. *Phys. Rev. E* **2012**, *85*, 056703.

[116]Tan, T. B.; Schultz, A. J.; Kofke, D. A. *Journal of Chemical Physics* **2010**, *133*, 134104.

[117]Kratky, K. W. *Chemical Physics* **1981**, *57*, 167–174.

[118]Speedy, R. J. *Journal of Physics-Condensed Matter* **1998**, *10*, 4387–4391.

[119]Polson, J. M.; Trizac, E.; Pronk, S.; Frenkel, D. *Journal of Chemical Physics* **2000**, *112*, 5339–5342.

[120]Chang, J.; Sandler, S. I. *Journal of Chemical Physics* **2003**, *118*, 8390–8395.

[121]de Miguel, E.; Marguta, R. G.; del Rio, E. M. *Journal of Chemical Physics* **2007**, *127*, 154512.

[122]Johnson, J. K.; Zollweg, J. A.; Gubbins, K. E. *Molecular Physics* **1993**, *78*, 591–618.

[123]van der Hoef, M. A. *Journal of Chemical Physics* **2000**, *113*, 8142–8148.

[124]Barroso, M. A.; Ferreira, A. L. *Journal of Chemical Physics* **2002**, *116*, 7145–7150.

[125]Pauling, L. *Proceedings of the National Academy of Sciences of the United States of America* **1930**, *16*, 123.

[126]Brigatti, M.; Galan, E.; Theng, B. *Handbook of Clay Science* **2006**, *1*, 19–69.

[127]Hanwell, M.; Curtis, D.; Lonie, D.; Vandermeersch, T.; Zurek, E.; Hutchison, G. *Journal of Cheminformatics* **2012**, *4*.

[128]Almarza, N. G. *The Journal of Chemical Physics* **2007**, *126*, 211103.

[129]Chang, J.; Sandler, S. I. *The Journal of Chemical Physics* **2006**, *125*, 054705.

[130]Vega, C.; Noya, E. G. *The Journal of Chemical Physics* **2007**, *127*, 154113.

[131]Torrie, G.; Valleau, J. *Journal of Computational Physics* **1977**, *23*, 187 – 199.

[132]Vega, C.; Sanz, E.; Abascal, J. L. F.; Noya, E. G. *Journal of Physics: Condensed Matter* **2008**, *20*, 153101.

[133]Mastny, E. A.; de Pablo, J. J. *Journal of Chemical Physics* **2007**, *127*, 104504.

[134]Plimpton, S. *Journal of Computational Physics* **1995**, *117*, 1 – 19.

[135]Aragones, J. L.; Valeriani, C.; Vega, C. *The Journal of Chemical Physics* **2012**, *137*, 146101.

[136]Butler, B. D.; Ayton, G.; Jepps, O. G.; Evans, D. J. *The Journal of Chemical Physics* **1998**, *109*, 6519–6522.

[137]Dominguez, H.; Allen, M. P.; Evans, R. *Molecular Physics* **1999**, *96*.

[138]Wan, L.; Iacovella, C. R.; Nguyen, T. D.; Docherty, H.; Cummings, P. T. *Phys. Rev. B* **2012**, *86*, 214105.

[139]Owens, J. D.; Houston, M.; Luebke, D.; Green, S.; Stone, J. E.; Phillips, J. C. *Proceedings of the IEEE* **2008**, *96*, 879–899.

[140]Strohmaier, E. TOP500 Supercomputer. 2014; http://www.top500.org/list/2014/11/.

[141]Intel, Intel Xeon Processor E5-2667 v2. 2013; http://ark.intel.com/products/75273/Intel-Xeon-Processor-E5-2667-v2-25M-Cache-3_30-GHz.

[142]Nvidia, NVIDIA Tesla K40 GPU. 2014; http://www.nvidia.com/object/tesla-servers.html.

[143]Anderson, J. A.; Lorenz, C. D.; Travesset, A. *Journal of Computational Physics* **2008**, *227*, 5342 – 5359.

[144]Nosé, S. *The Journal of Chemical Physics* **1984**, *81*, 511–519.

[145]Hoover, W. G. *Physical Review A* **1985**, *31*, 1695.

[146]Martyna, G. J.; Klein, M. L.; Tuckerman, M. *The Journal of Chemical Physics* **1992**, *97*.

[147]van der Hoef, M. A. *The Journal of Chemical Physics* **2000**, *113*, 8142–8148.

[148]Radhakrishnan, R.; Gubbins, K. E.; Sliwinska-Bartkowiak, M. *The Journal of Chemical Physics* **2000**, *112*, 11048–11057.

[149]Cui, S. T.; Cummings, P. T.; Cochran, H. D. *The Journal of Chemical Physics* **2001**, *114*, 7189–7195.

[150]Miyahara, M.; Gubbins, K. E. *The Journal of Chemical Physics* **1997**, *106*, 2865–2880.

[151]Israelachvili, J. *Proceedings of the National Academy of Sciences of the United States of America* **1987**, *84*, 4722–4724.

[152]Gao, J. P.; Luedtke, W. D.; Landman, U. *Physical Review Letters* **1997**, *79*, 705–708.

[153]HOOMD. http://codeblue.umich.edu/hoomd-blue.

[154]Keys, A. S.; Iacovella, C. R.; Glotzer, S. C. *Annual Review of Condensed Matter Physics* **2011**, *2*, 263–285.

[155]Keys, A. S.; Iacovella, C. R.; Glotzer, S. C. *Journal of Computational Physics* **2011**, *230*, 6438–6463.

[156]Kaneko, T.; Mima, T.; Yasuoka, K. *Chemical Physics Letters* **2010**, *490*, 165 – 171.

[157]Long, Y.; Palmer, J. C.; Coasne, B.; liwinska Bartkowiak, M.; Gubbins, K. E. *Microporous and Mesoporous Materials* **2012**, *154*, 19 – 23.

[158]Johnson, J.; Zollweg, J.; Gubbins, K. *Molecular Physics* **1993**, *78*, 591–618.

[159]Cummings, P. T.; Docherty, H.; Iacovella, C. R.; Singh, J. K. *AIChE Journal* **2010**, *56*, 842–848.

[160]Bureau, L. *Physical Review Letters* **2007**, *99*, 225503.

[161]Mittal, J.; Truskett, T. M.; Errington, J. R.; Hummer, G. *Phys. Rev. Lett.* **2008**, *100*, 145901.

[162]Wu, Y.; Cheng, G.; Katsov, K.; Sides, S. W.; Wang, J.; Tang, J.; Fredrickson, G. H.; Moskovits, M.; Stucky, G. D. *Nature Materials* **2004**, *3*, 816–822.

[163]Docherty, H.; Cummings, P. T. *Soft Matter* **2010**, *6*, 1640–1643.

[164]Persson, F.; Tegenfeldt, J. O. *Chemical Society Reviews* **2010**, *39*, 985–999.